

Intragastric Mechanical Systems for Dysmotility Diagnosis and Obesity Treatment

By
Zixun Jia

B.S., M.S. Harbin Institute of Technology (2016, 2018)
Submitted to the Department of Mechanical Engineering
In Partial Fulfillment of the Requirements for the Degree of
Doctor of Philosophy
At the
MASSACHUSETTS INSTITUTE OF TECHNOLOGY
June 2023

©2023 Zixun Jia. This work is licensed under a CC BY-SA 2.0.

The author hereby grants to MIT a nonexclusive, worldwide, irrevocable,
royalty-free license to exercise any and all rights under copyright,
including to reproduce, preserve, distribute and publicly display copies of
the thesis, or release the thesis under an open-access license.

Authored by: Zixun Jia
Department of Mechanical Engineering
May 10th, 2023

Certified by: Carlo Giovanni Traverso
Associate Professor of Mechanical Engineering, Thesis Supervisor

Accepted by: Nicolas Hadjiconstantinou
Professor of Mechanical Engineering, Graduate Officer

Intragastric Mechanical Interventions for Diagnosis and Treatment

By

Zixun Jia

Submitted to the Department of Mechanical Engineering on May 20th, 2023 in Partial Fulfillment of the Requirements for the Degree of Doctor of Philosophy in Mechanical and Electrical Engineering

ABSTRACT

Obesity represents one of the critical non-communicable global epidemics of our time affecting over 40% of the U.S. population and its impact continuously expands. The gastrointestinal (GI) tract is the main site of food digestion, nutrient absorption, and recognized to have a significant role in the signaling of satiety. This thesis aims to address two major healthcare challenges stemming from the obesity epidemic, dysmotility evaluation and intervention to simulate satiety as a mode of therapy. Specifically, dysmotility, often associated with metabolic derangements including diabetes mellitus and obesity, can be challenging to evaluate with precision. Satiety induction also remains a major challenge due to functional requirements including minimal invasiveness and long-term efficacy. This thesis presents the fundamental mechanics, materials development and electronic underpinnings of novel interventions that address both diagnostic and therapeutic unmet needs.

Clinical evaluation of GI motility is currently limited to radiographic and nuclear methods that provide information on gastric emptying rate. While high-resolution manometry is used to evaluate motility in narrow tubular organs, such as the esophagus and rectum, there is no analogous system for gastric motility evaluation. To address this, I have developed a motility mapping platform capable of 3D pressure distribution mapping within the stomach. This incorporates the development of new materials for sensors which can operate within the dynamic range of forces experienced in the GI tract, the mechanical framework to support engagement with gastric wall and the electronics to support sensing and recording of the contractile forces. The platform has also been validated in the esophagus and rectum and compared to Food and Drug Administration (FDA)-approved high-resolution manometry devices. This new motility mapping system could revolutionize the understanding, diagnosis, and treatment of poorly understood conditions such as functional dyspepsia by enabling three-dimensional *in vivo* characterization of motility in the stomach.

Current intragastric balloon therapy may be limited by a lack of persistent weight loss, as static balloons have been associated with plateauing of weight loss in large mammals. We hypothesized that the plateauing

is associated with gastric accommodation of the static balloon and loss of stimuli. To address this challenge, I developed a novel endoscopically administered gastric resident device that supports dynamic satiety induction to approximate the natural satiety induction process associated with episodic meal ingestion. The device expands before meals to occupy the gastric cavity, then shrinks to a minimal volume after the meal. I have developed two gastric residency and dynamic expansion mechanisms based on motorized and balloon approaches. I conducted preliminary evaluation of the system *in vitro* and *in vivo* using the swine model. This minimally invasive system enables dynamic satiety induction to support weight loss.

Thesis supervisor: Carlo Giovanni Traverso

Title: Karl Van Tassel (1925) Career Development Professor of Mechanical Engineering

ACKNOWLEDGEMENTS

When I moved into Edgerton House, lugging two massive suitcases and suffering from 12 hours of jet lag, completing my PhD seemed like a distant dream. Now, that once distant future has become a reality.

First and foremost, I would like to express my gratitude to my thesis advisor, Prof. Giovanni Traverso. I am truly thankful for his mentorship, inspiration, knowledge, and guidance. I also want to thank Prof. Sang-Gook Kim, for hosting me as a visiting student, supervising my research in my first year, and offering guidance for passing the qualifying exams. I want to thank Prof. Robert Langer, Prof. Gareth McKinley, Dr. Phillip Nadeau, and Prof. Khalil Ramadi for serving on my thesis committee, supervising my progress, and providing guidance. I want to thank Prof. Asegun Henry for providing references in support of my fellowship applications.

I want to thank senior members of the lab who have mentored and advised me throughout my graduate studies. Thank you, Dr. Sahab Babae, Dr. Hen-Wei Huang, Dr. Sean You, Dr. Kewang Nan, Dr. Ziliang Zhang, Dr. Shriya Srinivasan, and Dr. Vitor Sencadas. Thank you for helping me go further and understand deeper.

I want to thank Dr. Julia Ding, Dr. Daniel Shonibare, and Dr. Stephanie Owyang for collaborating and providing clinical insight in support of the work.

I want to thank my students who joined my projects, I not only teach you guys but also learn a lot from you. Thank you, Qiyun Gao, Michelle Zong, Jesse George-Akpenyi, Sylvia Waft, Tanner J. Packham, Gabriella Ulloa, Ziyang Zhang, Alexandra C. Lee, Yuehe Mao, Agustin G Valdes Martinez, Grace Peng, Crystal Yong Yan Liang, Cecile Leclerc, Olivia B McGrath, Kai Maier, Laura Huang, Rostam Reifschneider.

I want to thank lab members who help me work on the *in vivo* studies and 3D printing. Thank you, Johannes Kuosmanen, Josh Jenkins, Andrew Pettinari, Alison M Hayward, Niora Fabian, Seokkee Ming, Matthew Murphy, George Selsing, Keiko Ishida, Wiam Abdalla Mohammed Madani.

I want to thank my fellow graduate students in the lab, thank you for your companionship. Thank you, So-Yoon Yang, Adam Gierlach, Crystan McLymore, James McRae, Louis B DeRidder, Jack Chen, Sanghyun Park, Deepak Subramanian, Anita Dey Barsukova, Patricia Jastrzebska-Perfect.

I want to thank the friends I made in the Department Mechanical Engineering of MIT, Edgerton House, and the Wuming Theater Club. You guys made my graduate life lovely. I want to thank Whitaker Health Science Fund and the T.S.Lin Fellowship for their financial support.

Finally, I want to thank my family for supporting me, without you I couldn't have made it through.

CONFLICTS OF INTEREST

Zixun Jia is a co-inventor of the US patent application number 63/442,732 filed on February 1, 2023.

Table of content

Chapter 1. Introduction.....	14
1.1 Anatomy of the gastrointestinal tract	14
1.2 Cross section of the gastrointestinal tract.....	16
1.3 Neuro-mechanical processes involved in motility.....	17
1.4 Common Motility diseases and their pathological nature	20
1.5 FDA-approved motility diagnostic tools and interventions.....	23
1.6 Novel and investigational tools for dysmotility diagnosis	28
1.7 Satiety signaling pathway	34
1.8 Bariatric surgical treatments for obesity	35
1.9 Endoscopic obesity treatments	38
1.10 Oral drug treatments for obesity	41
1.11 Injection drug treatments for obesity	42
Chapter 2. The design of shape memory-based gastrointestinal tract motility mapping probe	45
2.1 The necessity of 3D motility mapping in the stomach	45
2.2 Adaptive motility sensing probes.....	47
2.3 Self-aligned supporting structure for motility probes.....	57
2.4 Sensor probe prototyping and integration with supporting structure	66
Chapter 3. Universal motility mapping system and its <i>in vivo</i> validation.....	68
3.1 Scanning board design, fabrication, and scanning workflow	68
3.2 Self-calibration and testing protocols of the scanning board.....	70
3.3 Bench-top tests of esophagus, rectum and stomach probe	72
3.4 <i>In vivo</i> evaluation protocols on a swine model	75
3.5 <i>In vivo</i> evaluation of the motility mapping probes	76
Chapter 4. Motorized expansion head dynamic satiety stimulator and its <i>in vivo</i> validation	81
4.1 Dynamic satiety stimulation.....	81
4.2 Structural analysis of the skeleton motorized expansion head.....	81
4.3 Analysis of protection cover and covered motorized expansion head	87
4.4 Motorized expansion head parts selection and manufacturing	91
4.5 <i>Ex vivo</i> and <i>in vivo</i> validations of motorized expansion head	93
Chapter 5. Pump-balloon dynamic satiety stimulator and its <i>in vivo</i> validation	95
5.1 Air balloon inflation system design and optimization.....	95
5.2 Design and fabrication of air valve and bifurcation.....	97
5.3 Balloon durability and fluid mechanical tests.....	100

5.4 Electronic design and control algorithms of balloon stimulator	106
5.5 Portable balloon stimulator integration.....	112
5.6 <i>In vivo</i> validation of air balloon stimulator.....	113
5.7 Feeding behavior change caused by air balloon stimulator.....	115
Chapter 6. Conclusion and outlook	118
Appendix A. Scanning board circuits.....	120

Table of Figures

Fig. 1	48
Fig. 2	49
Fig. 3	50
Fig. 4	53
Fig. 5	53
Fig. 6	54
Fig. 7	56
Fig. 8	57
Fig. 9	58
Fig. 10	59
Fig. 11	61
Fig. 12	62
Fig. 13	65
Fig. 14	66
Fig. 15	67
Fig. 16	68
Fig. 17	69
Fig. 18	70
Fig. 19	73
Fig. 20	74
Fig. 21	77
Fig. 22	77
Fig. 23	78
Fig. 24	79
Fig. 25	80
Fig. 26	82
Fig. 27	83
Fig. 28	84
Fig. 29	88
Fig. 30	90
Fig. 31	90
Fig. 32	92
Fig. 33	93
Fig. 34	94
Fig. 35	95
Fig. 36	96
Fig. 37	97
Fig. 38	98
Fig. 39	98
Fig. 40	99
Fig. 41	100
Fig. 42	101
Fig. 43	101
Fig. 44	102
Fig. 45	103
Fig. 46	104
Fig. 47	104
Fig. 48	105
Fig. 49	105

Fig. 50	106
Fig. 51	107
Fig. 52	108
Fig. 53	108
Fig. 54	110
Fig. 55	112
Fig. 56	113
Fig. 57	114
Fig. 58	114
Fig. 59	115
Fig. 60	116

This page is intentionally left blank.

List of Tables

Table 1 Anatomy of GI tract.....	16
Table 2 FDA-Approved Motility Diagnostic Tools and Interventions.....	24
Table 3 Novel and Investigational Tools.....	29
Table 4 Maximum time to prevent phase transition in overtube in the <i>in vivo</i> experiments.	65
Table 5 The value of stresses in the skeleton motorized expansion head.....	86
Table 6 The value of stresses in a single 646Q balloon covered motorized expansion head.....	90
Table 7 Device actuation system data	92
Table 8 The feeding schedule during the feeding behavior experiment.	117

This page is intentionally left blank.

Chapter 1. Introduction

1.1 Anatomy of the gastrointestinal tract

The gastrointestinal (GI) tract consists of the esophagus, stomach, small intestine, and large intestine successively. The GI tract for an adult is approximately 9 m long, extending from the mouth to the anus. The primary function of the GI tract is digesting food in preparation for cellular utilization and eliminating bile secretions and unabsorbed food material [1].

The esophagus is a dynamic tube that transfers boluses of food/liquid downward, through peristaltic waves, to the stomach while preventing gastroesophageal reflux. The adult's esophagus is usually 25 to 28 centimeters long and divided into three parts: cervical (5-6cm), thoracic (16-18cm), and abdominal (1-2.5cm). The esophagus has two types of peristaltic contractions (primary and secondary) that together form a wave-like motion. The primary peristalsis involves both central and peripheral mechanisms, consisting of inhibition (called deglutitive inhibition) followed by excitation. The secondary peristalsis is entirely due to peripheral mechanisms and involves inhibition followed by excitation [4, 5]. Primary peristalsis is initiated by a swallow and is the main source of esophageal transit whereas secondary peristalsis is distension-induced and functions to maintain an empty esophagus by clearing refluxate from the stomach in the absence of swallowing [2].

An empty stomach is about 30 cm long and 15 cm across its widest point. There are three main regions in the stomach: fundus (the uppermost hollow), corpus (the body), and antrum (from proximal to distal). Across these regions of the stomach, there are three distinct motility patterns. The first one is gastric accommodation, which happens in the proximal stomach (fundus and corpus) after the ingestion of food, to support the temporary storage of food. It can be further divided into two main responses: receptive and adaptive relaxation. Receptive relaxation is the mechanism whereby the smooth muscle in the proximal stomach relaxes within seconds of food bolus being introduced to the oropharynx and esophagus. Adaptive relaxation is a slower mechanism that adjusts the gastric fundal muscle tone in response to gastric and duodenal distension along with increased gastric intraluminal pressure. The second gastric motility pattern is antral contraction waves (ACWs), where the antrum acts as a peristaltic food pump as ring-shaped muscular contractions of the gastric wall move along the stomach. This movement is responsible for mixing and grinding of the food particles. ACWs regulate gastric emptying by enabling the release of gastric contents into the duodenum. The third motility pattern is the migrating motor complexes (MMCs) during the fasted state. They sweep indigestible solids from the stomach to the intestine through very strong mechanical contraction waves, typically repeating every 120 minutes [4].

The small intestine oversees the breakdown of food, absorbing nutrients needed for the body, and disposing of unnecessary components. It is a tubular organ with a length of about 6 - 6.5m for adults [5]. It is divided into the duodenum (0.2 – 0.25m), jejunum (2.5m), and ileum (3m) [6]. During fasted states, MMCs propel the chyme from stomach into the small intestine [6]. This complex is characterized by a regular cycle with four phases. Phase I is a prolonged period of quiescence (40–60% of total time); phase II is an increased frequency of action potentials and smooth muscle contractility (20–30% of total time); phase III is the most prominent phase where a front of intense spiking activity migrates down the entire small intestine, in order to sweep remnants of the previous meal into the colon and prevent stagnation and bacterial overgrowth (5–10 minutes); phase IV shows a declining motor activity [8, 9]. In fed state, this cycle is interrupted and the motility pattern in the small bowel becomes an irregular spiking activity called the fed pattern. This fed pattern of motility does not seem to move intestinal contents forward to any great extent but mixes these contents with digestive juices and spreads them over the absorptive surface [5].

The large intestine has the function of absorbing water and electrolytes, producing and absorbing vitamins, and forming and propelling feces toward the rectum for elimination. The large intestine of an adult is approximately 1.5m long and takes up one-fifth of the length of the GI tract [7]. It consists of four parts: the cecum (a pouch within the peritoneum), colon (absorbs water and electrolytes and transports food waste), rectum (a temporary storage for feces), and anal canal (connects the rectum to the anus) [7]. The large intestine has two types of motility mechanisms. The first one is haustral contraction, which moves food slowly to the next haustra (sacculae) and mixes chyme to help with water absorption. It happens frequently and regularly, about 3 to 8 contractions per minute. The second one is mass movement. This peristalsis pattern is stronger and can move chyme to the rectum quickly. Mass movement appears less frequent than haustral contraction, normally occurring only a few times a day. These gastric movements can be measured by motility index (MI), defined as $\ln(\text{sum of pressure amplitudes} \times \text{numbers of contraction})$ by Kloetzer et al. The median MI in gastric window of healthy individuals was reported as 11.83 [8]. One would find that the MI of the peristalsis is lower before lunch and dinner, with the lowest index appearing during sleep. The highest index appears after eating. The amplitude of the motility in the large intestine is usually less than 60 mmHg [9].

Please refer to Table 1 for a summary of the anatomy and functionality of the GI Tract.

Table 1 Anatomy of GI tract

GI Section	Dimension	Sub-GI part	Characterization/dimension	Motility patterns	Characterization of motility patterns	Functionality of the motility pattern
Esophagus	18-25 cm	Cervical	5–6 cm	Primary peristaltic contractions	Involves both central and peripheral mechanisms; consisting of inhibition (called deglutitive inhibition) followed by excitation.	Initiated by a swallow and is the main source of esophageal transit
		Thoracic	16-18cm			
		Abdominal	1-2.5cm	Secondary peristaltic contractions	Entirely due to peripheral mechanisms; involves inhibition followed by excitation.	Functions to maintain an empty esophagus by clearing refluxate from the stomach in the absence of swallowing.
Stomach	30 cm long and 15 cm across its widest point	Fundus	The uppermost hollow	Gastric accommodation	Happens in the proximal stomach (fundus and corpus) after the ingestion of food.	Support the temporary storage of food.
		Corpus	The body			
		Antrum	From proximal to distal	Antral contraction waves (ACWs).	The antrum acts as a peristaltic food pump; ring-shaped muscular contractions of the gastric wall move along the stomach.	Mix and grind the food particles; regulate gastric emptying.
				Migrating motor complexes (MMCs) during the fasted state.	Very strong electromechanical contraction waves, typically repeating every 120 minutes.	Sweep indigestible solids from the stomach to the intestine
Small intestine	6 - 6.5m	Duodenum	0.2 – 0.25m	Fast state	Characterized by a regular cycle with four phases: Phase I: a period of quiescence; Phase II: increased frequency of action potentials and smooth muscle contractility; Phase III: a front of intense spiking activity migrates down the entire small intestine; Phase IV: declining motor activity	Propel the chyme from stomach into the small intestine
		Jejunum	2.5m			
		Ileum	3m	Fed state	The previous cycle is interrupted and the motility pattern in the small bowel becomes an irregular spiking activity	Mixes intestinal contents with digestive juices and spreads them over the absorptive surface
Large Intestine	1.5m	Cecum	6 cm	Haustral contraction	3 to 8 contractions per minute	Moves food slowly to the next haustra (sacculae); mixes chyme to help with water absorption
		Colon	About 1.5m			
		Rectum	12 cm	Mass movement	Happens a few times a day in normal people.	Can move chyme to the rectum quickly
		Anal canal	3.8 – 5 cm			

1.2 Cross section of the gastrointestinal tract

The GI tract has a unique structure to serve the functions of digestion, absorption, and secretion of contents. For example, multiple levels of infoldings of the intestine wall create a gigantic surface area, allowing maximum nutrient absorption. The GI tract has a four-layer organization, composed of the mucosa, submucosa, muscularis propria, and either serosa or adventitia. Each layer is linked together by neural and vascular elements and connective tissue [10].

The mucosa is the innermost layer, consisting of the epithelium, lamina propria, and muscularis mucosae. Within the mucosa, the layer facing the intestinal lumen is the epithelium, made up of epithelial cells.

Outward from the epithelium layer is the lamina propria, consisting of subepithelial connective tissue and lymph nodes. At the base of the lamina propria is the third layer called muscularis mucosae, or a continuous sheet of smooth muscle cells. The mucosa is where most of the absorptive functions take place [10]. It also provides protection for the muscle layer, acting as the first line of defense against stomach acid [11]. Underneath the mucosa is the submucosa. The submucosa is composed of inflammatory cells, lymphatics, autonomic nerve fibers, and ganglion cells. The arteries and venous branch out and distribute contents in the submucosa. It acts as a secretory layer and allows mucosa to move freely during peristalsis. Outside the submucosa is the muscularis propria, made up of the inner circular muscle layer, intermuscular space, and outer longitudinal muscle layer. Smooth muscle cells are arranged into two muscle layers and the intermuscular space is occupied by the myenteric plexus consisting of autonomic neural fibers and ganglion [12]. The muscularis propria is most important for motility, as most peristalsis occurs in its smooth muscle layer. The main function of the muscularis mucosa is to propel food through the gut. The outermost layer is the serosa or, if it lacks a mesothelial layer, the adventitia. The serosa is made up of squamous epithelial cells, the mesothelium, and connective tissue. Most of the digestive tract is bound by serosa, only the oral cavity, thoracic esophagus, ascending colon, descending colon and the rectum have an adventitia. The boundary layer, either the serosa or the adventitia, serve as a protective barrier [10]. Interestingly, unlike other organs of the body the esophagus is made up of both skeletal and smooth muscle. Specifically, the upper third of the esophagus is striated skeletal muscle and the lower third is made up of smooth muscle, whilst the middle third is a mixture. Peristalsis progresses seamlessly despite differential muscle types across the esophagus.

1.3 Neuro-mechanical processes involved in motility

GI motility results in the movement of food through the digestive tract by peristalsis, or involuntary contractions and relaxations of the muscle [12]. There are mainly two mechanisms involved with controlling motility, via the enteric nervous system (ENS) or the central nervous system (CNS). The ENS controls motility mostly through peristaltic reflex, while the CNS provides extrinsic neural inputs that help regulate, modulate, and control motility [13].

A. Enteric nervous system and its involvement in the motility

The ENS is located within the wall of the GI tract, extending from the lower third of the esophagus through to the rectum [14], and consists of two distinct ganglionated neuronal plexuses: the myenteric plexus (MP), also known as Auerbach's plexus, and the submucosal plexus (SP), also known as Meissner's plexus. The MP is found along the entire length of the GI tract, located in between the outer longitudinal and inner circular smooth muscle layers of the muscularis propria. It controls motility by coordinating muscle

movements to accomplish synchronic propulsion of food [15]. The SP in larger mammals such as human form multiple layers (inner, outer, and in some cases intermediate) between the longitudinal and circular layers of the external muscle and is situated in the submucosal layer. It plays a similar but smaller role in influencing motility as the MP [16].

The ENS comprises its own population of sensory neurons. The main type of sensory neuron, intrinsic primary afferent neuron (IPAN), has the morphology of Dogiel type II, that is, multipolar neurons with some axons projecting to the mucosa and other axons projecting to neighboring nerve cells. IPANs form self-reinforcing networks by connecting with each other via slow excitatory postsynaptic potentials. They transmit signals to interneurons and motor neurons via both slow and fast excitatory postsynaptic potentials waves. IPANs are mainly found in the MP and are indirectly excited by luminal chemical or mechanical stimulation of the mucosa via the release of neurotransmitters from endocrine cells in the epithelium. The main involving neurotransmitters in the MP include acetylcholine and calcitonin gene-related peptides [17]. Some IPANs are also observed in SP and are important in evoking reflexes after sensing mechanical stimulation of the mucosa [16].

By having its own population of sensory neurons, the ENS is capable of initiating reflex responses independent from the CNS [18]. Sensory neurons first pass mechanical, thermal, osmotic, or chemical information to the MP through enteric primary afferent neurons. All the information is processed and integrated by the interneurons and the descending interneurons pass the command down to the motor neurons which control the muscle to perform their function such as motility generation. For instance, the intestines have a reflex mechanism whereby sensory neurons sense changes primarily at mechanical levels and activate intestinofugal neurons to generate fast synaptic potentials to inhibit or excite gut motility. Intestinofugal neurons are neurons with cell bodies in the gut wall and axons in prevertebral ganglia and serves reflex between gut regions [19].

Besides the sensory neurons and interneurons, the interstitial cells of Cajal (ICC) and the fibroblast-like cells positive for platelet-derived growth factor receptor- α (PDGFR α) also play important roles in the motility generation process [14, 21]. ICC and PDGFR α - positive cells are the pacemaker cells of the GI tract, producing electrical slow waves that cause rhythmic contractions in the GI tract's smooth muscles [21]. They are responsible for transmitting ENS inhibitory and excitatory neural effects to the smooth muscle cells in GI muscles, which makes the stomach muscular layer a multicellular electrical syncytium producing coordinated contractions, initiating propagation of the content toward the antral and pyloric

region [22]. Noteworthy, the production of slow waves does not require activity from enteric neurons, but ENS is required for propulsion along the gut [18].

B. Central nervous system and its involvement in the motility

The CNS consists of the brain and spinal cord and extends from inside the skull to the second lumbar vertebra [23], [24]. The CNS together with the peripheral nervous system is the main network that enables organisms to interact with its surroundings. Although the GI tract has its own intrinsic reflex circuits controlled by the ENS, the CNS provides extrinsic neural inputs that help regulate, modulate, and control GI function [13]. For instance, without interference from the CNS, the stomach can produce symptoms such as nausea, abdominal pain, and diarrhea due to disorganized and dysregulated gastric activity; however, regular gastric activity appears to recover after a period of time. This suggests that a function of the CNS in the stomach is to enhance and co-coordinate gastric functions, and is not the determining factor for functional motility [13]. The distal colon is innervated by both celiac and accessory celiac vagal branches, and less than 20% of neurons in the descending colon receive innervation from CNS through the efferent vagal innervations [25]. Noteworthy, the influence of the CNS in motility decreases distally along the GI tract [26].

The CNS influences motility through the autonomic nervous system, mainly via the parasympathetic pathway. The parasympathetic nerves exerts both excitatory and inhibitory control on intestinal motility [13]. The CNS parasympathetic innervations to the stomach, small intestine, and proximal colon are carried out by the vagus nerve and originate from the brainstem, specifically from the dorsal motor nucleus of the vagus (DMV) [13]. The DMV vagal neurons release acetylcholine, which activates the ICC and myenteric neurons in the stomach and upper part of the small intestine [27]. The activated neurons form two pathways, an excitatory cholinergic pathway and a non-adrenergic, non-cholinergic (NANC) pathway. The former pathway mediates smooth muscle contraction, and the latter allows smooth muscle relaxation [28].

The CNS parasympathetic innervations play an important role in regulating propulsive colonic motility. The parasympathetic innervation to the distal colon is carried out by preganglionic neurons found in the sacral vertebrae region of the spinal cord [13]. The axons of these neurons reach the colon by either innervating the postganglionic neurons within the myenteric plexus directly or indirectly through innervating the postganglionic neurons within the ganglia of the hypogastric plexus [29]. Damage to these parasympathetic neurons will result in dysregulated colonic motility and constipation. However, it is important to point out that the role of the CNS in the colon is to modulate and support intrinsic motility patterns and does not initiate or terminate colonic functions [13].

1.4 Common Motility diseases and their pathological nature

A. Functional Constipation

Functional Constipation is a dysmotility disease characterized by having fewer than three high amplitude propagated contractions (HAPC) per week. Symptoms in adults include bloating, abdominal pain, and a sensation of incomplete evacuation [30], while symptoms in children include fecal incontinence, urinary incontinence, and urinary tract infections [34]. Patients with functional constipation have been found to have decreased health-related quality of life, and higher direct outpatient costs. The prevalence of the disease affects approximately 15.3% of the population worldwide according to Rome criteria [31], and specifically 9.5% of the children population worldwide [32]. The causes of the disease are not fully known, but along with other functional GI disorders (FGIDs), is believed to be related to complex interactions within the gut-brain axis, microbial dysbiosis, visceral hypersensitivity, and abnormal GI motility [33].

From a molecular level, the origin of functional constipation is caused by serotonin underproduction. Patients with functional constipation experience underproduction of serotonin upon activation by food entering the gut wall. Serotonin is responsible for triggering muscle contraction through the release of acetylcholine; therefore, underproduction of serotonin leads to less muscle contraction in the gut [34]. On a functional level, the lack of serotonin results in less frequent non-propulsive contractions and HAPC. Repetitive non-propulsive contractions help absorption and mixing of content in the gut while HAPC causes the mass movement that brings stool from the ascending colon down to the left colon. HAPC happens once every 20 hours to 72 hours, typically after meals and upon awakening in normal adults, but it is less frequent in constipated patients [30]. As a result of having less frequent HAPC, fecal material remains in the colon for longer periods of time and undergo scybalation, or pebble-like stool formation, and impaction if becoming too hard and large to continue transit out of the rectum. Common treatments in the United States include polyethylene glycol as first line treatments, and secretagogues such as linaclotide, plecanatide, and lubiprostone as second line [35]. Stimulants that increase colon motility, such as senna glycosides and bisacodyl, are also used in practice. Surgery is a therapy of last resort [34].

B. Functional Diarrhea

The epidemiology of functional diarrhea is not clear, as few studies have distinguished functional diarrhea alone from diarrhea-predominant irritable bowel syndrome (IBS-D), and it can be considered on a single spectrum of functional diarrheal disorders. Functional diarrhea is defined as having watery stool and a lack of stool consistency for over four weeks without the presence of pain, while IBS-D comes with abdominal

pain [36]. Approximately 4.8% of the United States population experience nonspecific diarrhea [37], similarly to between 3% and 5% around the world [38]. Annual health care costs associated with IBS-Diarrhea type were US\$2268 per patient/year [39]. Other symptoms of functional diarrhea include increased frequency, the urgency of bowel movements, and incontinence. As another type of FGID, it's pathophysiology likely involves a complex interplay of gut-brain axis dysfunction and microbial dysbiosis leading to abnormal GI motility.

The physiologic factors behind functional diarrhea received little research attention. Although one study found increased propagating colonic contractions and decreased non-propagating contractions in functional diarrhea patients [40]. Generally, in a normal gut, ions and water are reabsorbed in a controlled manner through a combination of active transport of ions, passive transport of water, and help from absorptive and secretory agents, including local and systemic hormones and neurotransmitters. In patients experiencing diarrhea, rapid transit delivers fluid secreted during digestion to the distal small bowel or colon, overwhelming the reabsorption capacity of the colon [38]. First line treatments for functional diarrhea include the gut wall opioid receptor agonist loperamide, bile acid sequestrants, and second lines treatments would consider the antibiotic rifaximin [41].

C. Dysphagia

Dysphagia is a disease defined by difficulty swallowing. Approximately 7-10% of adults older than 50 years are estimated to have dysphagia according to Juckett et al., while Bazzocchi et al. estimated up to 20% of the general population experience dysphagia [39, 40]. Due to the high morbidity that comes with an inability to swallow, dysphagia leads to high healthcare utilization. In a study of economic burden on inpatients in the United States, total inpatient costs were a mean \$6,243 higher among those with dysphagia diagnoses compared to those without [42].

The location of difficulty swallowing further characterizes the type of dysphagia to be oropharyngeal or esophageal. Difficulty initiating a swallow is a characteristic of oropharyngeal dysphagia, while esophageal dysphagia is characterized by difficulty arising after the swallow. Oropharyngeal dysphagia is often caused by anatomical, structural, or neuromuscular malfunctions. The oropharynx includes the tongue, epiglottis, palatine tonsils, hard palate, and soft palate; dysfunction at these locations are anatomical causes of oropharyngeal dysphagia. [43]. Esophageal dysphagia is typically caused by intrinsic or extrinsic structural abnormality such as carcinoma and stricture, or disruption in normal motility. Whilst structural and anatomical origins can precipitate dysphagia, motility disorders such as achalasia and scleroderma is also known to influence esophageal dysphagia [44]. In a normal esophagus, an involuntary swallowing reflex

in the oropharynx is triggered after active swallowing, where coordinated muscular contractions and relaxations occur to move food into the proximal esophagus. Patients with dysphagia experience dysfunctional transfer of food in the pharynx past the upper esophageal sphincter into the esophagus [34, 36]. Possible therapeutics for esophageal dysphagia due to mechanical damage in the esophagus include bougie or balloon dilators accompanied by concurrent acid suppression therapy. Pneumatic dilation is the most effective nonsurgical approach for dysphagia caused by motility disorders [43].

D. Gastroparesis

Gastroparesis is defined as delayed gastric emptying. Symptoms include early satiety, vomiting, nausea, poor appetite, and pain in the upper abdomen. The prevalence of gastroparesis in 2007 was 37.8 per 100,000 persons in women and 9.6 per 100,000 persons in men [45]. However, it is important to note that many patients with gastroparesis symptoms have not had gastric emptying tests, which are only available in special laboratories, and so are never diagnosed. A study estimated that 1.8% of community subjects may have undiagnosed gastroparesis [46]. The diagnosis of gastroparesis requires an objective gastric emptying test using either scintigraphy, wireless motility capsule, or carbon breath testing. Scintigraphy is the most widely used method. Clinically, gastroparesis is defined as having > 90% food left in the stomach at 1 hour past the starting time, > 60% at 2 hours, and > 10% at 4 hours [47].

Most gastroparesis is idiopathic gastroparesis, or gastroparesis without a known cause. The most known cause is diabetes, which damages vagal nerves and pacemaker cells in the stomach [48]. Compared to controls, patients diagnosed with diabetic gastroparesis and idiopathic gastroparesis had approximately twice the healthcare cost of controls in the first three years of diagnosis. It is reported that the mean total cost difference per patient is \$34,885 in the first year if the patient is diagnosed of gastroparesis [49]. During a normal gastric emptying process, food in the gastric cavity goes through acid secretion and antral contraction, which are modulated by vagal innervation. During this process, nitrergic neurons modulate relaxation of the pyloric sphincter and gastric peristaltic activity. Camilleri et al. reported a significant decrease in the number of ICC and neuronal nitric oxide synthase (nNOS), which are positive inhibitory neurons in patients experiencing gastroparesis [47]. Liu et al. reported no significant difference in the number of ICC between gastroparesis patients and the control group but confirmed the reduction in the amount of nNOS-positive inhibitory neurons in gastroparesis patients. The study suggested that the reduction in nNOS-positive neurons reduced the coordination of gastric peristalsis, resulting in a delay in gastric emptying [22]. Other causes include vagal nerve damage caused by surgery, hypothyroidism, neuromuscular abnormalities of the gastric motor function caused by nervous system disorders such as Parkinson's disease; reduction in nitrergic inhibitory neurons and in ICC and/or telocytes, and viral

infection of the stomach [38, 41]. Notably, some opiates, antidepressants, hypertension and allergy medications could cause gastroparesis-like symptoms. Although medications cannot cause gastroparesis, they could exacerbate the symptoms from gastroparesis. Standard treatments for gastroparesis include dietary modification and prokinetic agents such as metoclopramide or erythromycin. Tricyclic antidepressants and cannabinoids can be used as second-line therapy [45].




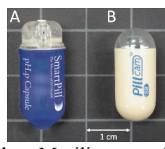
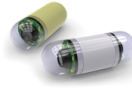
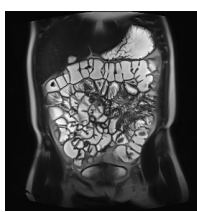

1.5 FDA-approved motility diagnostic tools and interventions

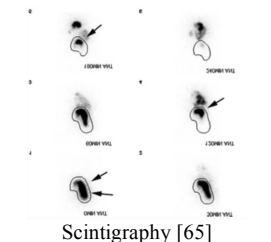
There are many FDA-approved tools to currently assess motility function in individuals as outlined in Table 2.

A. High-resolution manometry

High-resolution manometry (HRM) is a motility diagnostic tool that is used to assess whether a patient's esophagus is adequately functioning by mapping the pressure in the GI tract in response to liquid or solid swallows [50]. It can evaluate dysphagia when endoscopy or radiographic studies have not satisfied a definitive diagnosis. In addition, it can be used to diagnose a variety of esophageal motility disorders including eosinophilic esophagitis, jackhammer esophagus, nutcracker esophagus, and in rarer cases, scleroderma and achalasia [51]. For example, if a patient has been recommended anti-reflux surgery for gastroesophageal reflux disease (GERD) treatment, HRM would be used to rule out an achalasia or scleroderma diagnosis as anti-reflux surgery would not effectively treat them [50]. This device includes a series of closely spaced pressure sensors on a catheter that is passed through the nose into the esophagus. The pressure sensors convert physical pressure in the GI tract into electrical signals, and a recording device amplifies and stores those signals [52]. It measures the natural wave-like contractions of the esophagus, as well as the force and coordination of the esophageal muscles as liquids or solids are moved down the GI tract [53]. Software processes the HRM pressure output using interpolation to generate an esophageal pressure topography (EPT) plot, color-coded to show higher and lower pressure areas. The EPT plots can then be further analyzed by software to generate an esophageal motility disorder diagnosis [54]. Two common types of these catheter devices are water-perfused catheters coupled to volume displacement transducers and solid-state strain gauge transducers [52]. Common suppliers of both types of catheter devices include Medtronic (ManoScan ESO), Smit Medical, and Laborie [57, 58, 59].

Table 2 FDA-Approved Motility Diagnostic Tools and Interventions

Diagnostic Tool	Functionality	Portion of GI Tract	Mechanism	Indications/Contraindications	Drawbacks
 High-resolution manometry [58]	Assess whether patient's esophagus is adequately functioning with liquid or solid swallows	esophagus	Pressure converts to electrical signals, generates an esophageal pressure topography (EPT) plot, color coded for high/low pressure areas	Evaluating dysphagia; no contraindications	N/A
 Anorectal Manometry [59]	Assess whether rectum and anal sphincter functioning	rectum	Pressure converts to electrical signals, generated into dynamic pressure map, color coded based on pressure	Diagnosing defecatory disorders; no contraindications	N/A
 Impedance Planimetry [60]	Displays distensibility of organs in GI tract	esophagus	Electrodes measure voltage which can deduce cross sectional area; pressure signals	Evaluating dysphagia, monitoring during anti-reflux surgery and cardiomyotomy; no contraindications	N/A
 Wireless Motility capsule [61]	Measures pH, temperature, pressure in GI tract	GI tract	Wirelessly sends data that can help measure gastric emptying time	Evaluating treatment for gastroparesis, slow transit constipation, small bowel dysfunction; no contraindications	N/A
 Wireless Capsule Endoscopy [62]	Small video camera transmits pictures of GI tract	Small bowel, GI tract general	Wireless transmission of pictures	Diagnosing obscure GI bleeding and small bowel Crohn's disease; no contraindications	N/A
 MR Enterography [63]	Takes cross-sectional images of small intestine	Small intestine	Oral contrast agent and MRI machine allows small intestine to be visible	Investigating small bowel Crohn's disease and tumors and small bowel peristalsis; no contraindications	More time consuming, less stable image quality, more expensive, lower spatial resolution than CT Enterography
 CT Enterography [64]	Takes cross-sectional images of small intestine	Small intestine	Oral contrast agent and CT scanner allows small intestine to be visible	Acute patients with difficulty holding breath, investigation of bowel masses, assessment of potential perforation or complete bowel obstruction; no contraindications	Radiation exposure, single planar imaging, lower contrast and temporal resolution

	<p>Produces pictures of organs in the body, providing assessment of GI motility from mouth to rectum</p>	<p>GI tract</p>	<p>Oral drug with radioisotopes and external detectors measure radiation emitted in GI tract, transmits via electrical waveform which produces 2D/3D images</p>	<p>Evaluating persistent dyspepsia, explaining symptoms of postprandial fullness, early satiation, nausea, vomiting, epigastric pain; no contraindications</p>	<p>N/A</p>
---	--	-----------------	---	--	------------

Source: Adapted from [65], [66], [67], [68], [69], [70], and [71]

B. Anorectal Manometry

Anorectal manometry (ARM) is an imaging technique that is used to assess whether the rectum and anal sphincter are functioning adequately by looking at rectal pressure [66]. A catheter with a series of closely spaced pressure sensors and a small balloon is inserted into the rectum and measures the rectum pressure by inflating so that the muscles in the rectum and anus start contracting. This data is then converted into a continuous, dynamic map of anorectal pressures that are color-coded based on the pressure. As a result, the strength of anal and sphincter muscles, intestinal reflexes, and the movement of rectal and anal muscles can also be deduced [67]. ARM is generally used for diagnosing defecatory disorders, such as fecal incontinence, constipation, Hirschsprung’s disease, and difficulty passing stool in general [66]. Common suppliers include GI Supply, Medtronic (ManoScan AR), Medspira, Palex Medical, Laborie, Given Imaging, Sandhill Scientific, and Medical Measurement Systems [67].

C. Impedance Planimetry

Impedance planimetry is an imaging technique that displays the distensibility of organs in the GI tract as a function of pressure and cross-sectional area. The idea is that tonic and phasic muscular contractions as well as wall compliance can reveal the dimensions of hollow internal organs and the movement of contents within them [59]. A catheter ending with a cylindrical balloon is inserted transnasally and distended with set volumes of conductive fluid, often a saline solution. Inside the balloon, an array of uniform ring electrodes mounted on the catheter segment measure voltage which can be used to deduce electrical impedance and cross-sectional area. A solid-state pressure transducer measures intra-balloon pressure [62, 63]. This device can be used for the evaluation of dysphagia and achalasia by characterizing the mechanical properties of the esophageal wall and localizing areas of reduced distensibility. It is also used to monitor lumen diameter and contraction during anti-reflux surgery and cardiomyotomy (an operation for achalasia of cardia where muscles fail to relax, resulting in a hindrance of food and fluid passage into the stomach) [59]. The primary supplier of impedance planimetry devices is Medtronic, with the product more commonly known as Endoflip [61].

D. Motility Capsule

The motility capsule is a capsule that can be swallowed by patients and moves through the GI tract while wirelessly sending back environment or image data inside the GI tract [68]. It needs three components to function: an ingestible single-use capsule of 26 mm × 13 mm, a receiver, and a display software [69].

There are two kinds of capsules that are equipped with different systems inside. The first one is the wireless motility capsule (WMC) system which consists of a battery that can last for 5 days, a transmitter operating at a wavelength of 434 MHz, a pH sensor, a temperature sensor, and a pressure sensor, all wrapped inside a shell made of rigid polyurethane [69]. A WMC can measure the pH (range, 0.05–9.0, accurate to 0.5 pH units), temperature (range, 25–49°C), and pressure (range, 0–350 mmHg). The data obtained allow for indirect measures of capsule ingestion (indicated by an abrupt rise in temperature as the capsule enters GI tract), gastric emptying time (GET), and body exit time [67, 68]. Some of the common applications of the WMC include measuring GET in treatments of gastroparesis, measuring colonic transit time in treatments of suspected slow transit constipation, and measuring small bowel transit time to detect small bowel dysfunction in patients with generalized motility disorders [71].

The second kind of capsule is the wireless capsule endoscopy (WCE) system that encapsulates a small video camera. With a shell also made of polyurethane, the WCE can take about 50,000-60,000 digital images of the digestive tract per study and transmit the pictures wirelessly to an external wearable recorder. This ability to image the entire small bowel makes it a common tool for the diagnosis of obscure GI bleeding and the investigation of small bowel Crohn's disease [61].

When using the two kinds of motility capsules in a clinical setting, the patients are required to fast overnight beforehand. For the WMC they are given a standardized meal with 120mL water when they attend the clinic, and then 50mL water to swallow the capsule. The patients will then be instructed to fast for another 6 hours and return home to their normal activities. An event recorder will be keeping track of the data from the capsule and the patients return to the recorder after 5 days [61]. In the clinical procedure for WCE, patients are allowed to drink two hours after the capsule ingestion and eat four hours after and return the recorder after the eight-hour test ends. For now, SmartPill is the only supplier of the WMC and the WCE can be found at Given Imaging (Medtronic Plc), Olympus Corporation, IntroMedic, Co. Ltd., Chongqing Jinshan Science & Technology (Group) Co., Ltd., CapsoVision, and RF System lab [70, 71].

E. Enterography

Enterography is a non-invasive imaging method that takes cross-sectional images of the body [74]. It enables GI imaging that measures the bowel lumen and wall, the adjacent mesentery and soft tissues, and a variety of extraintestinal abdominopelvic contents (e.g. the small bowel lumen, wall, and perienteric tissues) that helps evaluate possible inflammatory bowel disease (IBD) [75]. The detailed images of organs, tissues, and structures, such as bones and blood vessels, support the detailed examination of the small intestine and the detection of GI disease [72, 74].

There are two kinds of enterography that can be performed: Computed tomography (CT) enterography and Magnetic resonance (MR) enterography. The CT enterography uses a neutral enteric contrast agent taken orally and a CT scanner. During the test, the patient will first drink the liquid or have an enema that includes the contrast material which will help make the patient's small intestine more visible on the CT scan. Then the patient will be moved through the CT scanner to capture the X-ray images. While scanning, a different type of contrast will be injected into the vein of the patient's arm [77]. The advantages that CT enterography has over MR are it is less time-consuming, more stable image quality, cheaper cost, greater availability, and higher spatial resolution. It's usually used in examinations with acute patients who have difficulty in holding their breath, investigation of bowel masses, and assessment of potential perforation or complete bowel obstruction [74]. The MR enterography requires an oral contrast and a magnetic resonance imaging (MRI) machine that generates magnetic fields. The patient will first drink contrast material one hour before the test. Then, IV contrast dye is injected and their body is scanned under the MR machine before and after the contrast dye is injected through IV [78]. MR enterography is usually chosen over CT because of the absence of associated ionizing radiation exposure, multiplanar imaging capabilities, superb contrast and temporal resolution, and facilitation of sequential imaging over prolonged periods. Therefore, it's often used for initially investigating in patients with suspected small bowel Crohn's disease and tumors, detecting complications and following response to therapy of follow-up patients, and assessing small bowel peristalsis [75, 76].

The CT scanners can be found at Toshiba (now Canon Medical), Siemens, GE, and Philips [79]. The MRI machines are made by GE, Phillips, and Toshiba (now Canon Medical) [80]. Both the contrast material for CT and MR can be found at GE healthcare [75].

F. Scintigraphy

Scintigraphy is a method that uses a scintillation counter or another similar detector together with a radioactive tracer to produce pictures of organs within the body [81]. It measures the amount of radioactivity in the stomach (gastric counts) and can therefore provide an assessment of GI motility from the mouth to the rectum [79, 80]. Because GI scintigraphy studies are noninvasive, quantitative, and physiologic, they can be used to examine patients with GI dysfunctions and evaluate the effectiveness of treatments taken [83].

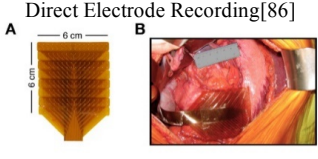
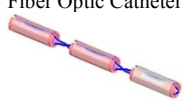
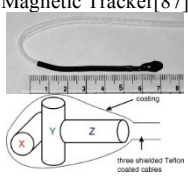
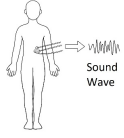
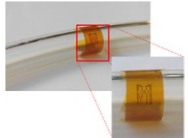
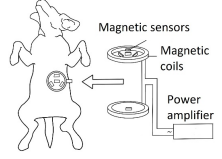
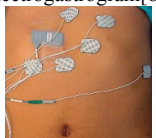
In scintigraphy studies, patients need to first intake a drug that contains radioisotopes and external detectors, such as gamma cameras, will detect the radiation emitted by the radioisotopes. Adults would typically drink 300 Ci of ^{99m}Tc -SC suspended in 150 mL of orange juice mixed with 0.1 normal of HCl. The patient is then imaged supine under a gamma camera, and an abdominal binder is used to increase abdominal pressures in 20 mmHg increments up to 100 mm Hg. Computer images are recorded for 30 seconds at each level of binder pressure [81]. As the drug travels from the fundus into the antrum, it gets closer to the gamma camera when positioned in front of the patient, and therefore would give a larger count [84]. The different gamma radiation emitted from the radioisotope is captured by external detectors (gamma cameras), and an electrical waveform would be detected. The computer then uses this waveform to generate 2D or 3D images accordingly [81]. The advantage of this method is that the gastric count pattern has a direct correlation with the volume of the meal remaining, and no knowledge of the shape of the stomach is needed. Some of the usages for scintigraphy in clinical practices are for evaluating persistent dyspepsia, and to explain the symptoms of postprandial fullness, early satiation, nausea, vomiting, and epigastric pain [83] where previous evaluations (including upper endoscopy) have shown no evidence of structural disease.


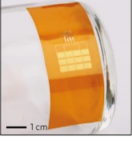
The gamma camera used for scintigraphy can be found at AEI, Siemens Corporation, PHDS Co, The InterMed Group, UTC Aerospace Systems - ISR Systems, and Advanced Test Equipment Corporation (ATEC). And some of the manufacturers for the radioisotopes are Frontier Technology Corp., AnazaoHealth Corporation, Spectrum Techniques, LLC, Trace Sciences International Corp., and Nordion Inc [85].

1.6 Novel and investigational tools for dysmotility diagnosis

Over the years, efforts have been made to develop novel tools that are not only more effective, but more feasible for assessing dysmotility, as summarized in *Table 3*.

Table 3 Novel and Investigational Tools

Diagnostic Tool	Functionality	GI Section	Indications	Contraindications	Drawbacks
<p>Direct Electrode Recording[86]</p> 	<p>Assess whether GI motility adequate via electrodes, looking at abnormal rhythmic patterns of ICC</p>	<p>All GI tract</p>	<p>Multi-electrode arrays record electrical potential and slow wave recorded and interpreted to assess whether GI motility adequate</p>	<p>Diagnosing gastroparesis; no contraindications</p>	<p>Requires surgery</p>
<p>Fiber Optic Catheter</p> 	<p>Measures pressure in GI tract, as well as transit of content through it</p>	<p>Esophagus</p>	<p>Fiber optic catheters reflect some wavelengths and transmit others; Catheter distorts from pressure leading to a shift in the location of reflected peak wavelengths.</p>	<p>Diagnosis of GI disorders like dysphagia, functional diarrhea, constipation; no contraindications</p>	<p>N/A</p>
<p>Magnetic Tracker[87]</p> 	<p>Measures stomach wall movement and elongation</p>	<p>Stomach</p>	<p>Solenoid transmitter emits a magnetic field; 3-axial receiver made of orthogonal solenoid coils receives magnetic field from specific directions; can tell if stomach is moving/elongating</p>	<p>Health diagnosis via estimating net gastric emptying and satiety scores; no contraindications</p>	<p>10% error in distance estimation</p>
<p>Bowel-Sound Pattern Analysis</p> 	<p>Measures muscular convulsions of the bowels</p>	<p>Abdomen / bowel</p>	<p>2 or 4 piezoelectric transducer monitoring sensors on the abdominal quadrants sense vibrations from bowel sounds. A neural network expert system analyzes the bowel sound pattern</p>	<p>Help diagnose, understand, and treat FGIDs; no contraindications</p>	<p>N/A</p>
<p>Flexible Pressure Sensors[88]</p> 	<p>Measures gastric and esophageal pressures</p>	<p>Esophagus</p>	<p>External pressure induces mechanical deformation of material that deforms strain gauges. This changes electrical resistance that is read by a system interpreted as pressure.</p>	<p>Evaluating dysphagia; no contraindications</p>	<p>N/A</p>
<p>AMR-ACB Arrays</p> 	<p>Measures spatiotemporal resolution through gastric activity contraction</p>	<p>Stomach</p>	<p>AMR sensor's electrical resistance is modulated by a magnetic field. ACB coil sensors measure biomagnetic fields in response to AC magnetic fields. Spatial resolution can be extracted from strength of magnetic fields</p>	<p>Optical imaging of GI tract; no contraindications</p>	<p>N/A</p>
<p>Electrogastrogram[89]</p> 	<p>High resolution spatiotemporal details in GI tract via multi-electrode arrays</p>	<p>Abdomen</p>	<p>Extracellular electrodes placed on abdomen records oscillating biopotentials of ICC; this wave course is sent to recording device, displayed as graph</p>	<p>Diagnose chronic dyspepsia, unexplained chronic nausea, vomiting, belching or gas pain, and gastroparesis; no contraindications</p>	<p>N/A</p>

Piezoelectric Gastric Sensor [90] 	Measure contractile patterns of GI tract	GI tract	Knots in pressure sensing silicon tubing increase sensitivity	Evaluating dysphagia and other motility disorders (similar to HRM); no contraindications	N/A
Piezoelectric Gastric Sensor [91] 	Senses physiological and pathophysiological states	Stomach	Pill capsule with piezoelectric sensor senses mechanical deformation within gastric cavity; settles on stomach lining and can measure physiological states of GI tract	Diagnose motility disorders and monitor ingestion in bariatric applications; no contraindications	N/A

Source: Adapted from [88], [92], [95], [96], [97], and [98]

A. Direct electrode recording

Direct electrode recording (DER) is the technique to directly measure the electrical slow waves generated by the ICCs in the GI tract. In the GI tract, there are ICCs that generate slow waves because of the changes in membrane potential. Using DER, abnormal rhythmic patterns of the ICC and GI tract can be known and used as a diagnostic measure of gastroparesis [92].

DER allows for high-resolution spatiotemporal details in the GI tract by multi-electrode arrays. Traditionally, a dense array of silver-wire electrodes is applied to a small area on one side of the intestine. The number of electrodes in each array can vary. These electrodes are coated with epoxy resin and placed *in vivo*, requiring surgery to place them directly on a specific region in the GI tract for high-quality recording [93]. Each electrode in the array can record the electrical potential at a particular point of the GI tract serosal wall by infusing the temporal data of the node. As a result, the generation and propagation of the slow wave can be recorded and sent to a recording device [86]. These waves can be interpreted to elucidate whether GI motility is adequately functioning in a patient [92]. A newer approach uses a flexible printed circuit board with electrodes in silicone cradles. It allows mapping around the curvy intestine geometry *in vivo*. Traditional silver-wire electrodes tend to be relatively inflexible, and therefore have trouble achieving good electrical contact. The flexible circuit boards eliminate this issue while maintaining the same functionality as the traditional DER [93].

Recently, DER is no longer a widely practiced technique because of its invasiveness. A more commonly used technique is now the electrogastrogram, a much less invasive approach to measuring rhythmic patterns in the GI tract [92].

B. Diagnostic Tool Miniaturization

Multiple groups have reported novel sensor design allowing for motility diagnostic tools to be miniaturized. Some of these devices include fiber optic catheters, magnetic trackers, bowel-sound pattern analysis, flexible pressure sensors, and AMR-ACB arrays.

C. Fiber Optic Catheters

Fiber optic catheters can measure the pressure of the GI tract, as well as the transit of content through it, to investigate whether the GI tract is adequately functioning. Also known as Fiber Bragg Grating (FBG) catheters, fiber optic catheters reflect particular wavelengths of light and transmit others. As the fiber distorts from pressure, the location of reflected peak wavelengths shifts, detected by a spectral detector. Pressure is then inferred by an initial calibration between pressure and wavelength shift [87, 88]. Compared to traditional manometry catheters, fiber optic catheters have a 1.4 mm smaller external diameter (4.2 mm vs. 2.8 mm), multiple measuring and sensing functions, and increased flexibility. As it is deployed *in vivo*, it can measure gastric pressures to aid the diagnosis of GI orders such as dysphagia, and functional diarrhea and constipation [96].

D. Magnetic Trackers

A magnetic tracker is an *in vivo* implantable device that measures stomach wall movement and elongation. The device is made up of a single solenoid transmitter and a three-axial receiver. The single solenoid transmitter is made up of a solenoid coil coated in a Teflon insulator that emits a magnetic field. The three-axial receiver has three orthogonal solenoid coils also coated in a Teflon insulator that receives the magnetic field. Each of the three solenoids receives the magnetic field from a specific direction, which helps calculate movement direction. All solenoid coils are 5 mm long, have an outer diameter of 2 mm, and have 1000 turns. These two probes are placed on opposite ends of the stomach wall and can then measure if the stomach is moving or elongating based on the change in received magnetic field intensity and direction. However, based on data from *in vitro* and *in vivo* studies in dogs and rats, there is still a 10% error in distance estimation which could be reduced with further development. Tomek et al. suggest that this device could eventually be used to infer stomach volume [87]. Gastric stomach volume is important to estimate net gastric emptying or satiety scores for health diagnosis [97].

E. Bowel-Sound Pattern Analysis

Bowel-sound pattern analysis, or the autonomous intestinal motility analysis system (AIMAS), is a noninvasive device that measures the muscular convulsions of the bowels. The goal is to implement an autonomous system for long-term, unsupervised GI monitoring. Two or four piezoelectric transducer monitoring sensors are symmetrically placed at the abdominal quadrants as bowel sounds create abdominal surface vibrations. The duration of the recording was between 1 hour and 6 hours. The surface signals are turned into a wave amplitude and sent to a neural network expert system that can deliver bowel sound pattern analysis based on it. Through this, the background noise in the data is also extracted so that the output is clearer and easy to read. As it analyzes gastric convulsions, it can help diagnose, understand, and treat FGIDs [98].

F. Flexible Pressure Sensors

Flexible pressure sensors are an improvement on HRM. The sensor is made of polyimide. External pressure induces mechanical deformation of the polyamide which would deform strain gauges. As a result, there is a change in electrical resistance. The resulting data is measured by an electrical readout system that is designed to have a user-friendly interface for physicians. As it measures gastric and esophageal pressures *in vivo*, it can essentially be an inexpensive alternative to HRM [88].

G. Anisotropic Magnetoresistive-AC Biosusceptometry (AMR-ACB)

AMR-ACB array is a less expensive and portable way of measuring spatiotemporal resolution through gastric activity contraction. Two components make up this novel device: AMR sensors and ACB, both being noninvasive and radiation-free sensors. For AMR sensors, electrical resistance can be modulated by the application of a magnetic field in the direction of its inherent magnetization. ACB coil sensors measure the biomagnetic fields in response to the AC magnetic field. When measuring the magnetic field, spatial resolution can be extracted because the stronger the detected magnetic field is, the closer the stomach walls. When testing *in vivo* with dogs, Paixao et al. inserted the array transnasally, and simultaneous magnetic and manometric continuous recordings were obtained. The results were very similar to manometry recordings, peaking at the same times and occurring within the same frequency range [99].

H. Electrogastrogram

The electrogastrogram (EGG) is a non-invasive alternative to DER. Similarly, it measures the waves generated from the ICC, where the ICCs change in membrane potential and depolarize smooth muscle cells. Using EGGs, abnormal rhythmic patterns of the ICC and GI tract can be known in a less invasive way. It

can diagnose motility disorders such as chronic dyspepsia, unexplained chronic nausea and vomiting, unexplained belching or gas pain, and gastroparesis [89].

Like direct electrode recording, EGG allows for high-resolution spatiotemporal details in the GI tract, achieved by multi-electrode arrays [100]. During an EGG procedure, extracellular electrodes are placed on the abdomen which records the oscillating biopotentials of the ICC [101]. These wet gel electrodes can be arranged in a variety of ways on the abdomen: there are reports of three electrodes across the abdomen and sixteen electrodes in a 4x4 pattern [95, 98]. Each of the electrodes can record the electrical potential at that point of the GI tract. These electrical impulses create a wave course that is sent to an electrical recording device and displayed as a graph. Subjects with a higher percentage of abnormal slow waves were linked to more severe abdominal pain [102]. Being a noninvasive technique, the electrogastrogram does not need devices inserted directly into the organ and has become a more dominant procedure than DER. However, more research is still being done to discover further uses for understanding the electrical signals from ICC and EGG [100].

I. Piezoelectric gastric sensor

The piezoelectric gastric sensors can be integrated into implantable devices that can measure contractile patterns of the GI tract [99]. In addition, the piezoelectric gastric sensor is a more inexpensive alternative to mainstream manometry devices.

Nan et al. discusses a sensor made up of liquid metal infused through thin silicone tubing and resembling the quipu, an ancient Inca method of knotting strings in ways that convey information. By tying knots in pressure sensing silicone tubing, the pressure sensing capabilities are enhanced. The pressure sensors become more sensitive to deformations because of shear stress and because the knots in series amplify the total pressure. Though this novel investigation has only been complete *in vitro*, this procedure would theoretically be similar to other catheter GI manometry procedures *in vivo* [90]. The sensor is inserted transnasally into the GI system and uses an ultrasound imager for wireless powering and real-time data communication [103]. This piezoelectric gastric sensor design has the least production cost compared to the other mainstream GI manometry techniques and may benefit low-resource settings [90].

Dagdeviren et al. reported ingestible electronics that can sense physiological and pathophysiological states. Traditional ingestible electronics tend to be solid and inflexible, with the potential associated risk of GI obstruction. This study designs an ingestible, flexible, piezoelectric device that senses mechanical deformation within the gastric cavity. The goal of this device is to treat and diagnose motility disorder and

monitor ingestion in bariatric applications. The patient ingests a pill capsule containing a piezoelectric sensor. As the capsule dissolves, the flexible device inside naturally unfolds and settles on the stomach lining with mucosa. In this position, the device can monitor the physiological states of the GI tract. The resulting data is sent to an external receiver and interpreted as instantaneous information on ingestion states in the GI tract [91], [99].

1.7 Satiety signaling pathway

It was previously believed that a human's biological need for energy was the primary factor driving feeding behavior, however, recent research has shown that the regulation of the satiety pathway involves a complex interplay between homeostatic and neurological factors. The satiety pathway operates as a mechanism that inhibits dietary consumption and controls appetite, rather than simply responding to it [104]. The state of satiety is achieved through the consumption of an appropriate amount of food within a specific time frame.

The regulation of the satiety pathway is orchestrated by the gut-brain axis through a delicate balance of neuronal and hormonal signals. Neuronal circuits in the hypothalamus and brainstem work together to maintain energy homeostasis, activated by sensory neurons in the GI tract [105]. The brainstem primarily receives neuronal signals from the GI tract, while the hypothalamus receives most of its signals from hormones circulating in the bloodstream. It is noteworthy that there are extensive reciprocal connections between the brainstem and hypothalamus, enabling both regions to jointly oversee the integration of endocrine and neuronal signals. Beyond physiological needs, the perception of satiety is also shaped by hedonic mechanisms, mediated by the brain's reward system. This is supported by the observation that meals are initiated before significant food deprivation and terminated before the delivery of nutrients to the system [104]. The appealing visual, olfactory, or gustatory signals from food can stimulate feeding, and at times, overeating.

After a meal, signals from mechanoreceptors and chemoreceptors are transmitted via the vagus nerve to the medial and dorsomedial parts of the nucleus of the solitary tract (NTS). Simultaneously, hormones are released into the bloodstream by the GI tract. These hormones can directly access the brain through the area postrema, which lacks a complete blood-brain barrier and serves as a point of interaction between the circulation and the brain. Projections from the NTS and brainstem then innervate the hypothalamus and the lateral hypothalamic area, which play a crucial role in mediating the conscious perception of satiety [106]. The hypothalamus and brainstem work in tandem to oversee the homeostatic regulation of satiety perception.

The brainstem contains key components of the appetite control system, including the area postrema (AP), dorsal vagal complex (DVC), and nucleus of the solitary tract (NTS). The AP, lacking a complete blood-brain barrier, serves as the main window between circulating factors and the brain. The DVC is the origin of preganglionic vagal efferent neurons that send commands from the brain to the gut, while the NTS receives signals from the gut and projects them to other regions, such as the hypothalamus and higher centers[107].

Two groups of neurons in the arcuate nucleus (ARC) of the hypothalamus are primarily responsible for regulating appetite. Neurons that co-express neuropeptide Y (NPY) and agouti-related peptide (AgRP) have been found to stimulate appetite [108], while neurons that co-express pro-opiomelanocortin (POMC) and cocaine-and-amphetamine-regulated transcript (CART) are known to inhibit appetite [109]. The POMC neurons release α -melanocyte-stimulating hormone (α -MSH), which acts as a melanocortin-4 ligand-receptor. Both groups of neurons project to the hypothalamic paraventricular nucleus (PVN) [110]. Additionally, both POMC and AgRP/NPY neurons express receptors for insulin and leptin, two important metabolic hormones found in the periphery. Leptin is secreted and expressed by white adipose tissue adipocytes, and its circulating level is directly proportional to fat mass [109]. Insulin, secreted by the pancreatic β -cells in response to nutrient ingestion, plays a critical role in regulating energy and glucose homeostasis by suppressing hepatic glucose production [111].

Gut hormones play a crucial role in regulating the satiety pathway through their presence in the circulation. Cholecystokinin (CCK), glucagon-like peptide 1 (GLP-1), and pancreatic polypeptide (PP) are just a few examples of key gut hormones involved in the feeding control system. CCK is a peptide hormone produced by endocrine I cells in the small intestine and is released into the circulation upon meal ingestion, promoting satiety by activating a visceral sensory circuit [112]. GLP-1, produced by intestinal epithelial endocrine L-cells, is also released upon meal intake and has been found to inhibit appetite when injected into the third ventricle of the brain in rats [113]. PP and peptide YY (PYY), along with previously mentioned NPY, are all part of the PP-fold family. PP is produced by pancreatic islets and localized by enteroendocrine cells throughout the GI tract and plays a critical role in energy regulation as its release into circulation is proportional to the number of calories consumed [114].

1.8 Bariatric surgical treatments for obesity

A. Sleeve gastrectomy

A sleeve gastrectomy is a bariatric surgical procedure designed to help patients lose excess weight and reduce the risk of life-threatening health problems associated with obesity, including heart disease, high

blood pressure, high cholesterol, sleep apnea, type 2 diabetes, strokes, cancer, and infertility. Candidates for the procedure typically have a body mass index of 40 or higher or a body mass index of 30-40 with serious weight-related health problems. In the weeks leading up to the surgery, patients are required to start a physical activity program and stop any tobacco use. The day before the procedure, there may be restrictions on eating and drinking. The surgery, which typically takes 1-2 hours and is performed laparoscopically using small instruments inserted through multiple small incisions in the upper abdomen, is performed under anesthesia. During the procedure, 80% of the stomach is removed, leaving a tube-shaped stomach about the size and shape of a banana, limiting the amount of food that can be consumed [115]. Possible post-surgery risks include excessive bleeding, infection, blood clots, lung or breathing problems, leaks from the abdominal incisions, or stapler line insufficiency. Of the 10% morbidity rate associated with sleeve gastrectomies, stapler line insufficiency resulting in fistula leakage accounts for up to 80% of the morbidity and mortality [116]. Long-term risks include GI obstructions, hernias, gastroesophageal reflux, hypoglycemia, malnutrition, and vomiting. Approximately 25% of patients who undergo sleeve gastrectomies may eventually require reoperation due to insufficient weight loss or weight regain. Patients can expect to lose 60% or more of their excess weight and improve their obesity-related health problems. On average, patients experience a 47.3% loss of excess weight after 13.1 months, with reductions in blood glucose and hemoglobin A1c of 88.2 mg/dL and -1.7%, respectively [117].

B. Jejunioleal Bypass

The jejunioleal bypass was a bariatric surgical procedure popular in the late 60s and early 70's, known for its success in inducing weight loss by creating a surgical short bowel syndrome. At the time, it was considered the most effective surgical intervention for weight loss and was eligible for patients with weight-related health problems. The procedure involved the anastomosis of 35 cm of the proximal jejunum to the last 10 cm of the ileum, creating a shorter bowel route and leading to hyperphagia and malabsorption, reducing the number of calories absorbed. However, the procedure is no longer performed due to its high rate of serious short-term and long-term complications, including renal failure (37%), diarrhea (29%), calcium oxalate nephrolithiasis (29%), liver disease (10%), acute liver failure (7%), electrolyte imbalances, fat-soluble vitamin deficiencies, and malnutrition. It also carried the risk of metabolic consequences such as steatohepatitis, cirrhosis, renal oxalosis, gallstones, enteritis, arthritis, fatigue syndrome, bypass encephalopathy, or bypass dermatitis. As surgical procedures have improved over time, the number of patients retaining a jejunioleal bypass has decreased, with a high mortality rate and many opting for a different bariatric procedure after undergoing a reversal [118]. On average, patients lost 58 kg after one year and saw a 3.5 decrease in hemoglobin A1c [119]. The high complication rates and the need for lifelong

maintenance and follow-up have made the jejunoileal bypass much less popular in modern-day bariatric interventions.

C. Vertical Banded Gastroplasty

A vertical banded gastroplasty, also known as stomach stapling, is a weight loss surgery that involves the use of non-adjustable bands and staples to create a smaller stomach pouch. This allows patients to feel full with less food. To be eligible for the procedure, patients must have a body mass index greater than 40 or a body mass index of 35-40 with one or more obesity-related health problems. The surgery is performed laparoscopically, using small incisions in the abdomen to minimize invasiveness and avoid a large abdominal incision. Anesthesia is given, and a laparoscope is inserted to view the internal organs while small surgical instruments are inserted through other incisions. The stomach is then cut, stapled at the margins, and a restrictive band is looped to form a smaller, restricted pouch. However, there are several potential risks and complications associated with this procedure, including complicated reversal, pouch dilation, strict dietary requirements, and an inadequate weight loss effect. Other risks include blood loss, infection, deep vein thrombosis, staple line leakage, band slippage, and pouch enlargement [120]. In fact, 39% of patients undergo revisional surgery due to weight regain, vomiting, or food intolerance.

Before revisions, outlet dilation (17% of patients), pouch dilation (16%), and outlet stenosis (10%) were seen in some patients. 56 months after the revision, patients had an additional average effective weight loss of 23% and an additional reduction in comorbidities of 33%. On average, 66 months after the surgery, patients had an effective weight loss of 53% and a reduction in comorbidities of 54%. Recently, vertical banded gastroplasty procedures have become less common due to their high failure rate, high incidence of long-term complications, and the availability of newer techniques such as adjustable gastric banding and sleeves [121].

D. Laparoscopic Gastric Banding

Laparoscopic gastric banding is a weight-loss surgery that helps bariatric patients feel full with less food. It is typically used for patients with severe obesity who have not achieved success with other weight loss methods. To be eligible for the surgery, patients must have a body mass index greater than 40 or a body mass index of 35-40 with weight-related health conditions. Before the surgery, patients are required to participate in a bariatric surgery education program, undergo nutrition counseling, and may undergo imaging or upper endoscopy. Blood thinning medications, such as aspirin or ibuprofen, must be discontinued, and patients must not eat or drink anything after midnight before the surgery. The procedure itself takes 30-60 minutes and is performed laparoscopically, using small incisions in the upper abdomen

to place an adjustable band around the top part of the stomach. The band can be adjusted by adding or removing fluid in a balloon around the band through a port under the skin of the abdomen. Usually, fluid is injected at every routine clinical check.

However, specific risks associated with laparoscopic gastric banding include band slippage, stomach punctures, food not entering the stomach, food intolerance, and ineffective weight loss [122]. One year after a laparoscopic gastric banding, on average a patient has 45.7% excess weight loss, 28 kg of total weight loss, a 0.7% decrease in A1c, and major improvements in weight-related issues like arthritis, asthma, depression, diabetes, gastroesophageal reflux disease, hyperlipidemia, hypertension, joint and back pain, sleep apnea, and stress incontinence [123].

E. Roux-en-Y Gastric Bypass

Roux-en-Y gastric bypass (RYGB) is a weight-loss surgery that involves the formation of a small stomach pouch and its connection to a part of the small intestine [124]. It is recommended for patients with a body mass index greater than 40 or a body mass index of 35-40 with weight-related health conditions. Before the surgery, patients must follow the same pre-surgery procedure as gastric banding, including a bariatric surgery education program and nutrition counseling. During the operation, the stomach is reduced to a small pouch, about the size of an egg, and stapled off before being attached to the roux limb of the small intestine, forming a “Y” shape. This modification of the GI tract allows digested food to bypass the rest of the stomach and upper part of the small intestine, reducing the amount of fat and calories absorbed from foods, but also limiting the patient's vitamin and mineral intake.

However, RYGB is associated with several post-surgery risks, including low levels of vitamins, low levels of iron or calcium, dumping syndrome, narrowing at the sites where the intestines are joined (stenosis or stricture), internal hernia, the need for additional surgery, failure to lose enough weight, and weight regain. After one year, patients lose an average of 29 kg in total weight loss and have a 2.9% A1c decrease [125].

1.9 Endoscopic obesity treatments

A. Intra-gastric Balloon

The intra-gastric balloon is a weight-loss procedure that involves the placement of a saline or air-filled balloon in the stomach to reduce feelings of hunger and increase satiety. To be eligible for this procedure, patients must have a body mass index of 30-40 and be willing to make healthy lifestyle changes, attend regular medical follow-ups, and participate in behavioral therapy. Additionally, patients who have had

previous stomach or esophageal surgery are not eligible for this procedure. During the procedure, which typically takes about 30 minutes, the patient is usually sedated, and a doctor inserts a catheter attached to the intragastric balloon through the throat and into the stomach. The balloon is then filled with either saline or air, depending on the type of intragastric balloon being used [126]. An endoscope allows the doctor to visualize the intragastric balloon as it is filled with 400-700 mL of saline-stained methylene blue [127]. After the procedure, patients are typically required to follow a liquid diet for about a week before transitioning to soft foods and eventually a regular diet, around 3 weeks after the procedure. The balloon is typically left in place for up to 6 months, after which it can be removed through another endoscopic procedure.

However, it is important to note that 33% of patients may experience pain and nausea lasting a few days after the insertion of the balloon. Other potential complications associated with the intragastric balloon procedure include vomiting, balloon deflation, blockage of the digestive system, overinflation, and acute pancreatitis. Although rare, there is also a risk of developing ulcers or perforations in the stomach wall. On average, after 6 months, patients will have a total weight loss of 7-15%, excess weight loss of 30-47%, and an A1c decrease of 1.3% [128].

B. Endoscopic suturing

Endoscopic suturing is a weight-loss procedure that involves the use of an endoscope equipped with a stitching device to reduce the size of the stomach. This procedure is typically recommended for individuals with a body mass index greater than 40 or a body mass index of 30-40 who have weight-related medical issues or who have failed previous noninvasive weight loss measures. However, there are certain individuals who should not undergo this procedure. This includes individuals with gastric lesions, neoplastic findings, a family history of gastric cancer, mental health disorders, significant medical comorbidities that would make sedation unsafe, or coagulopathies [129].

During an endoscopic suturing procedure, the patient is given general anesthesia and endotracheal intubation. The procedure involves the use of a double-channel endoscope equipped with an endoscopic suturing system to make full-thickness sets of running sutures from the antrum to the fundus of the stomach. The goal of the procedure is to reduce the size of the gastric lumen by creating a tubular configuration with a modified greater curvature through the placement of sutured plications. One of the advantages of endoscopic suturing is that it is incisionless and less invasive compared to other bariatric surgeries. After the procedure, patients receive instructions on a specific diet and undergo intensive follow-ups with a multidisciplinary team at 3, 6, and 12 months post-surgery. The endoscopic suturing configuration should

still be intact one year after the procedure [130].

The most common risks associated with endoscopic suturing procedures include bleeding and perforations, which can occur immediately or at a later time. To minimize the risk of these complications, some solutions such as the use of conventional endoclips or endoloop and clips can be utilized [131]. After a year of undergoing the procedure, patients saw an average weight loss of 57% in terms of excess weight loss and a decrease in their A1c levels by 1% [129], [130]. On average, patients experience total weight loss was 14.4% after 6 months, 17.6% after 12 months, and 20.9% after 24 months.

C. AspireAssist

AspireAssist is an outpatient bariatric procedure designed for weight loss. Eligible candidates for the procedure are individuals with a body mass index between 35-55 who have been unable to achieve or maintain weight loss through non-surgical weight loss treatments. It is important to note that there are certain conditions and disorders that may make AspireAssist an unsuitable option. These include disorders such as dysphagia, previous stomach ulcers, uncontrolled high blood pressure, blood clotting disorders, pregnancy or lactation, bulimia, binge eating disorder, night eating syndrome, anemia, previous abdominal surgery, serious pulmonary or cardiovascular disease, chronic abdominal pain, or severe organ dysfunctions.

The AspireAssist device consists of two components: the A-Tube and the Skin-Port. The A-Tube is a thin, flexible tube that is inserted into the stomach through the mouth and has five holes for food to enter during the "aspiration" process. The A-Tube also has a soft, round bumper that sits against the inner wall of the stomach to prevent it from being pulled out. The Skin-Port, which is attached to the A-Tube outside the abdomen, has a pump system that transfers food into the A-Tube for aspiration. During the procedure, the patient is sedated, and the doctor uses an endoscope to insert the A-Tube into the stomach. A small incision of 1 cm is made on the abdomen, and a long needle is inserted to access the stomach from the outside. A thin wire is then passed through the needle, pulled out through the mouth, and attached to the A-Tube. The wire is used to pull the A-Tube through the mouth into the stomach until the bumper is positioned against the inner wall of the stomach. The end result is a long tube extending from the stomach.

The AspireAssist device is designed to decrease the number of calories the body absorbs. After a meal, the patient performs the "aspiration" process by using the device to empty 25-30% of the stomach contents into the toilet, preventing the body from absorbing those calories. To effectively aspirate, the patient needs to chew their food into smaller pieces and wait 20-30 minutes after eating. AspireAssist is intended for use as

a long-term bariatric therapy [132]. The AspireAssist procedure has the potential for certain risks, such as A-Tube failures, buried bumpers, and infections. After a period of one year, patients experienced a weight loss of 18.3% in terms of total weight loss and a decrease in their A1c levels by 1% [133].

1.10 Oral drug treatments for obesity

A. XENICAL - orlistat

XENICAL (orlistat) is a medication used for weight loss management. It works by inhibiting the activity of lipases, which are enzymes responsible for breaking down dietary fat into absorbable free fatty acids and monoglycerides. By blocking the action of lipases, XENICAL reduces the amount of fat absorbed by the body, leading to weight control. This medication is recommended for obese individuals with a body mass index of 30 or above, or a body mass index of 27 with other risk factors like hypertension, diabetes, or dyslipidemia. However, it should not be prescribed if the obesity is caused by an organic factor such as hypothyroidism. The recommended dose of XENICAL is 120 mg, taken three times a day, which is capable of reducing the absorption of dietary fat by around 30%.

According to clinical trials, the average weight loss after 6 months and 1 year of treatment with XENICAL was 12.4 lbs and 13.4 lbs respectively, while patients taking a reduced-calorie diet without XENICAL lost 6.2 lbs and 5.8 lbs respectively. However, taking XENICAL can lead to some common side effects such as oily spotting, flatulence with discharge, fecal urgency, fatty or oily stools, increased defecation, and fecal incontinence. It is contraindicated in patients with chronic malabsorption syndrome or cholestasis, and its use can also reduce cyclosporine plasma levels when co-administered with cyclosporine [134].

B. Qsymia - phentermine/topiramate

Qsymia (phentermine/topiramate) is a prescription medication for weight management in adult patients who are either obese (body mass index over 30 kg/m²) or overweight (body mass index 27 kg/m²) with weight-related health conditions such as hypertension, type 2 diabetes, dyslipidemia, or abdominal obesity. The drug is a combination of phentermine and extended-release topiramate, and its exact mechanism of action in weight loss is not fully understood. However, it is believed that the combination of phentermine's release of catecholamines in the hypothalamus and topiramate's various pharmacologic effects, including the modulation of voltage-gated ion channels, inhibition of AMPA/kainate excitatory glutamate receptors, and inhibition of carbonic anhydrase, results in decreased appetite, food consumption, and increased satiety in patients.

Qsymia is taken once a day in the morning with or without food. It comes in three different daily dosages (phentermine mg/topiramate mg extended-release): 3.75mg/23 mg (low), 7.5mg/46 mg (mid), and 15mg/92 mg (high), and the dosage will gradually increase according to the doctor's prescription. The expected weight loss after 12 weeks of treatment with the mid-dose (7.5mg/46mg) of Qsymia is 3% of baseline body weight, while the high-dose (15mg/92mg) is expected to result in at least 5% of baseline body weight loss after an additional 12 weeks. However, there are some known side effects associated with the use of Qsymia, including birth defects (cleft lip/cleft palate), increases in heart rate, suicidal thoughts or actions (Topiramate, an ingredient in Qsymia, may cause patients to have suicidal thoughts or actions), and increases of acid levels in bloodstream (metabolic acidosis) [135].

C. CONTRAVE - naltrexone HCl / bupropion HCl

CONTRAVE (naltrexone HCl / bupropion HCl) is a prescription medication for weight management in overweight and obese adults. It contains two active ingredients, naltrexone and bupropion, which have different mechanisms of action in the brain that regulate food intake and reward. Naltrexone is an opioid antagonist and bupropion is a weak inhibitor of the reuptake of dopamine and norepinephrine. While the exact mechanism of how CONTRAVE causes weight loss is not fully understood, nonclinical studies have shown that naltrexone and bupropion affect two separate areas of the brain involved in regulating food intake and reward. The medication is indicated for adults with a body mass index of 30 kg/m² or greater (obese) or 27 kg/m² or greater (overweight) with at least one weight-related comorbidity, such as hypertension, type 2 diabetes, or dyslipidemia. The recommended starting dose is one morning tablet in the first week, two morning and one evening tablet in the second week, and two tablets each for morning and evening from the third week onwards [136].

Clinical trials have shown that patients who take CONTRAVE for 12 weeks should experience a minimum of 5% total weight loss from the start of therapy [137]. In a 56-week trial, patients taking CONTRAVE (32 mg/360 mg dosage) had an average weight loss of 5.4%, compared to 1.3% in the placebo group. However, like with any medication, there are potential side effects including suicidal thoughts or actions (linked to bupropion), nausea, dizziness, constipation, difficulty sleeping, headache, dry mouth, vomiting, and diarrhea [136].

1.11 Injection drug treatments for obesity

A. Saxenda - liraglutide

Saxenda (liraglutide) is a Glucagon-like peptide 1 receptor analog and a prescription medication used for weight management in patients with a BMI greater than 30 or a BMI greater than 26 with weight-related health conditions. The drug works by regulating appetite and mimicking the effects of the naturally occurring hormone GLP-1, which helps control hunger. To be effective, Saxenda should be used in conjunction with a reduced-calorie diet and increased physical activity. The drug is taken once a day via injection in the abdomen, thigh, or upper arm. However, it is contraindicated for individuals with a family history of medullary thyroid carcinoma (MTC) or conditions like multiple endocrine neoplasia syndrome type 2 (MEN 2) [138].

On average, after 52-56 weeks of treatment with Saxenda, patients experienced a 6% total weight loss and a 1.3% decrease in their A1c levels [139]. Some common side effects associated with Saxenda include nausea, diarrhea, constipation, vomiting, injection site reactions, headaches, fatigue, dizziness, stomach pain, and changes in lipase levels in the blood. More severe side effects could include thyroid tumors, including cancer, pancreatitis, gallbladder problems, hypoglycemia, tachycardia, kidney failure, allergic reactions, and depression [138].

B. Wegovy - semaglutide

Wegovy (semaglutide) is an injectable prescription medication containing 2.4 mg of semaglutide, a molecule that mimics the effects of GLP-1, a hormone that regulates hunger. This medication is designed to help patients manage obesity and is intended for adults with a body mass index of 30 or more, or a body mass index of 27-30 with weight-related medical issues. Wegovy is administered once a week via a single-use pen injection and is most effective when used in conjunction with a reduced-calorie diet and increased physical activity. It is important to note that Wegovy should not be used by individuals who have a history of medullary thyroid carcinoma (MTC) or multiple endocrine neoplasia syndrome type 2 (MEN 2) in their family, or by those who are already taking other semaglutide-containing products or GLP-1 receptor agonist medicines.

In a 26-week clinical trial, patients treated with Wegovy showed a 1.1% decrease in A1c levels. Another 68-week trial found that patients achieved an average of 15% total weight loss [140], and a third 68-week trial conducted by the FDA showed a 12.4% total weight loss [141]. The most reported side effects of Wegovy include nausea, diarrhea, vomiting, constipation, abdominal pain, headache, fatigue, dizziness, bloating, gas, stomach flu, and heartburn. Other potential side effects include pancreatitis, gallbladder problems, hypoglycemia, kidney failure, allergic reactions, tachycardia, and depression. In rare cases, serious side effects, including thyroid tumors (including cancer), may occur.

C. *IMCIVIREE - setmelanotide*

IMCIVIREE (setmelanotide) is a prescription medication that is used to treat obesity in patients who have deficiencies in the genes responsible for producing pro-opiomelanocortin (POMC), proprotein convertase subtilisin/kexin type 1 (PCSK1), or the leptin receptor (LEPR). The use of IMCIVIREE is only recommended for patients who have been confirmed to have deficiencies in POMC, PCSK1, or LEPR through an FDA-approved test. The medication is administered as an injection, typically once a day in the morning, with a dosage that varies depending on the patient, but is typically around 2mg. The injection can be given in the abdomen, thighs, or back of the upper arms [142].

According to clinical data, patients with POMC or PCSK1 deficiency who received IMCIVIREE treatment achieved an average total weight loss of 10% after 1 year, with 80% of patients reaching this target. Similarly, patients with LEPR deficiency had a 10% average total weight loss after 1 year, with 45% of patients achieving this outcome. Additionally, IMCIVIREE treatment resulted in an average decrease in A1c of 8.1% after 1 year. Despite its potential benefits, IMCIVIREE use is associated with certain side effects, including male and female sexual dysfunction, depression, increased skin pigmentation, and benzyl alcohol toxicity. More common side effects include skin darkening, injection site reactions, nausea, headache, diarrhea, stomach pain, vomiting, depression, and spontaneous erections in males without sexual activity [143].

Upon evaluating current dysmotility diagnosis tools and obesity treatments, it has become evident that there is a need for a non-invasive tool that can accurately map stomach contractions, as well as an effective obesity treatment with long-term efficacy and minimal invasiveness.

Chapter 2. The design of shape memory-based gastrointestinal tract motility mapping probe

2.1 The necessity of 3D motility mapping in the stomach

GI motility, in which ingested material is mechanically transported through the GI tract, is essential to the digestion and processing of nutrients [144]–[146]. There are two main types of motility reflexes: accommodation or distension [147], [148], which refers to the GI tract's ability to expand or contract according to the volume of its contents; and peristalsis [149]–[151], which refers to the mechanical waves generated by the GI tract to propel and process food. The impairment of motility, also called dysmotility, is quite common, with a prevalence of 15-20% among the general population [152], [153]. GI dysmotility underlies common disorders such as gastroesophageal reflux disease and chronic constipation. However, diagnostic methods remain limited, particularly for the study and evaluation of gastric motility.

Esophageal and anorectal motility are better understood than gastric motility, owing to the existence of HRM and impedance planimetry. In clinical practice, HRM is used in narrow, homogenous, tubular organs (i.e. the esophagus) in the evaluation for motility disorders. HRM involves a catheter with a densely packed pressure sensor array with a resolution of 1-2 cm, and is capable of evaluating the spatial-temporal pressure distribution in a 2D format (pressure along a line). Information provided by HRM is critical for the diagnosis and management of esophageal dysmotility. For instance, the American Gastroenterological Association recommends HRM evaluation before anti-reflux surgery to rule out contraindications or esophageal motility disorders that cannot be treated with this type of surgery [154]. Similarly, anorectal manometry is commonly used in the evaluation of fecal incontinence or constipation to guide further management such as biofeedback therapy or surgical correction of disorders such as Hirschsprung's disease [155], [156]. Impedance planimetry [157] is another technique used in the evaluation of esophageal motility, and uses a plastic tube filled with saline and a catheter with an array of electrodes, with changes in tube diameter caused by contractions appearing as changes in electrical resistance between a pair of electrodes. However, these catheter-based techniques cannot be used in other parts of the GI tract that are not narrow and homogenous, such as the stomach.

Evaluation of gastric motility in clinical practice is mainly limited to gastric emptying scintigraphy, which involves ingestion of a radiolabeled meal and measurement of the percentage of gastric retention at time points up to 4 hours. This is useful for the diagnosis of gastroparesis, or delayed gastric emptying (defined as gastric retention >10% at 4 hours) [158]. However, this method does not provide pressure mapping within the stomach. Wireless motility capsules [159] can be used as an alternative to gastric scintigraphy, but provide similar information on gastric emptying. These capsules are swallowed by patients, and are

capable of measuring pH, pressure, and temperature. Gastric emptying, small bowel transit time, and colonic transit time are estimated based on the pH profile (i.e. the rise in pH when moving from the stomach to the small intestine, and a drop in pH when moving from the small intestine to the colon). Pressure readings are of limited clinical utility compared to manometry and are unable to detect a peristaltic pressure wave front [160]. Importantly, patients with and without gastroparesis often experience functional dyspepsia, defined as ongoing symptoms (early satiety, postprandial fullness, bothersome epigastric discomfort) in the absence of structural etiologies such as peptic ulcer disease or acid reflux [161]. Without a method to map spatial pressure distribution within the stomach, functional dyspepsia is common but poorly understood. Because the correlation between perception of discomfort and changes in gastric motility/pressure remains uncertain.

A number of investigational motility mapping systems have been developed in attempts to improve evaluation of motility throughout the GI tract. Electrode-recording systems are used to quantify the bioelectrical signals that correspond to motility. These systems have been used to directly measure the bioelectric slow waves in the GI tract in animal studies[162]–[166]. However, these systems need to be surgically implanted, which limits their clinical application. There are efforts to record and analyze motility-related bioelectrical signals via non-invasive electrodes; however, the information acquired is limited to abstracted features of motility rather than global distributions [167], [168]. Another trend in motility mapping systems is to replace solid-state pressure sensors with optical fiber-based pressure sensors [169]–[171]. Optical fiber-based sensors enable sensing probes to be miniaturized. However, since sensors are still embedded into a catheter like a traditional manometry probe, the data acquired from the two systems are effectively the same, and limited to narrow tubular organs. Other sensing methods have also been used for motility mapping, including mutual inductance [172], bioacoustics [173], resistive sensing (e.g., thin-film strain gauges) [174], magnetoresistive sensing and biosusceptometry [175]. Previously, our group developed a flexible piezoelectric device that can conform to smaller segments of the stomach wall and monitor motility [176]. To the best of my knowledge, there is currently no system reported capable of achieving 3D pressure mapping of the stomach.

To support 3D mapping of gastric motility, I developed conformal pressure sensing probes. The motility sensing probes use Nitinol, a shape memory alloy, for its conformal and adaptive supporting structure. The design of the supporting structures is able to adapt to the anatomic and dimensional variation within stomachs across subjects. An array of pressure sensors is embedded into the probe, with a spatial resolution of 2 cm. The probes use flexible printed circuit (FPC) sensor belts, and an electronic interface is developed to read and process the data measured by all probes. Esophageal and rectal probes can be placed or removed

via an endoscopic overtube or directly into the lumen. The stomach probe can be stretched into a long belt and delivered endoscopically. Once the probe is deployed, body temperature triggers the phase transition of the Nitinol supporting structure; it then transforms into its pre-programmed shape. Once the probe is placed into the subject, body temperature continuously heats the probe and thus it is important to avoid phase transition from occurring before the probe is positioned. I found the deployment time of the stomach probe needs to be no more than about 4 minutes to avoid premature phase transition. Once the phase transition is complete, the pressure sensors are delivered to the wall of the GI tract. After testing is completed, the probes can be removed from the subject endoscopically without requiring a surgical procedure. The platform was tested to measure changes in gastric pressure in swine. As there is no clinically available system for mapping spatial-temporal pressure distribution within the stomach, this platform was also tested in the esophagus and rectum in swine, and validated against a FDA-approved HRM (34) system which is used clinically to obtain 2D intraluminal pressure data. The system not only integrates motility evaluation of three parts of the GI tract into one platform, but also achieves global motility mapping inside the stomach, which is not yet clinically available.

2.2 Adaptive motility sensing probes

The platform developed in this work has three different probes that are designed to support mapping of the mechanical pressure in the stomach, esophagus, and rectum (Fig. 1 a). Linear sensor probes are used for the esophagus and rectum. To map the 3D distribution of mechanical pressure in the stomach, a conformal globular supporting structure was envisaged and built. To deploy the stomach probe, it is stretched into a linear belt and advanced through an endoscopic overtube placed inside the esophagus. Once the device is deployed inside the body, the body temperature from the subject triggers the Nitinol phase transition. The probe returns to the programmed shape and conforms to the stomach walls. To retrieve the device, a cable, which is attached to the probe, can be withdrawn; the device will then exit via the overtube in the esophagus (see Figs. 1 c-d).

The bolus probe was deployed and retrieved through via upper endoscopy. During deployment (see Fig. 1 b *i*), I placed a lubricated overtube via the esophagus into the stomach. I unwound the probe (shown in orange) and began to push it through the overtube. Note that there's a wire attached to the coil at the end (shown in blue). I continued pushing the coil through the esophagus (see Fig. 1 b *ii*) until the coil was fully in the stomach. I confirmed it with videos from the endoscope. Once the Nitinol was in the stomach, it coiled back into its programmed shape due to the temperature in the body (see Fig. 1 b *iii*). When the coil was ready to be removed, I pulled the string attached to it until all the equipment was fully out (see Fig. 1 b *iv*).

The rectal and esophageal probes can be directly inserted into the rectum or via an overtube into the esophagus respectively. Cables attached to either rectal or esophageal probe can be withdrawn; the probes then exit the subject. Figs. 2 a-c show X-ray images of the probes in the esophagus, rectum, and stomach of a swine, respectively. An endoscopic image of the probe deployed in the stomach of the swine is shown in Fig. 1 h demonstrating the coil-like structure (Fig. 2 e) and juxtaposition with the gastric mucosa. The sensing units are delivered to the stomach wall and pushed against by the supporting structure (Fig. 2 f). Endoscopic and radiographic evaluation did not reveal mucosal injury as supported by the lack of abrasions as well as free air in the abdomen.

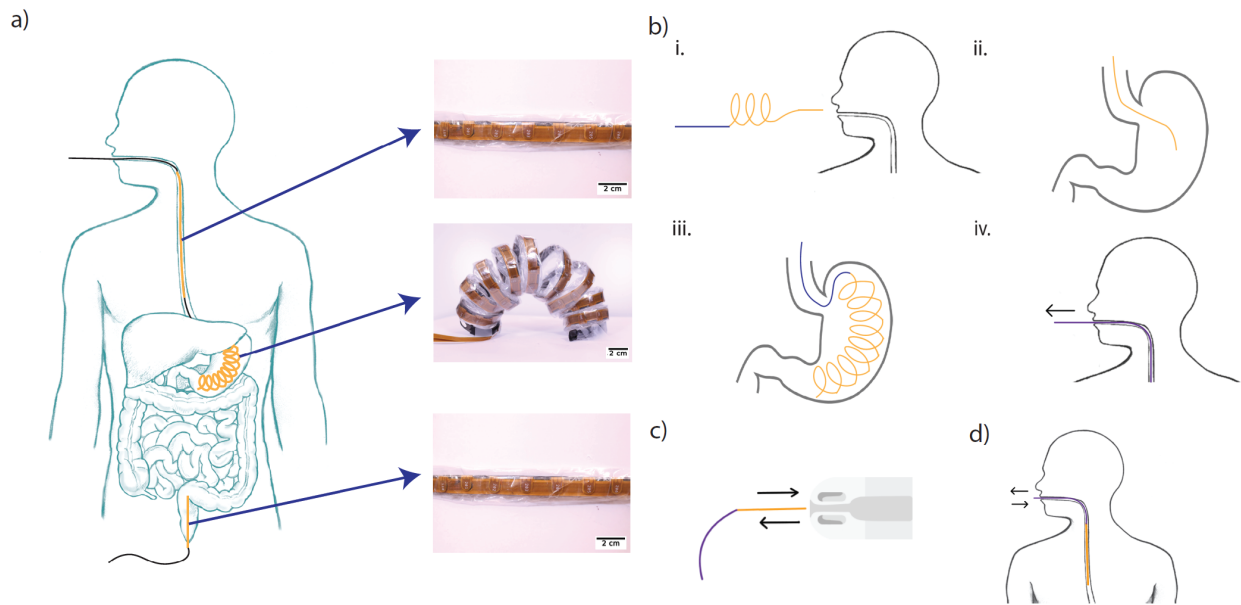


Fig. 1 a) Illustration of the universal motility mapping system with tubular and bolus sensing probes. b) Deployment and retrieval workflow of the stomach motility probe. Deployment and retrieval illustrations of c) rectum and d) esophagus probe.

The probes are fabricated entirely using off-the-shelf materials thus can be easily scaled up in production. To design the conformal GI tract motility mapping probes with piezoresistive sensors, materials with low elastic modulus and high electrical conductivity are needed. To build a sensing unit, I evaluated commercially available anti-static foams and fabricated multi-walled carbon nanotube (MWCNT)-doped polymers. I selected four kinds of off-the-shelf foams in the screening process (Protektive Pak Inc., 37704, 37680, 37700, Desco Inc., 12250). The foams are purchased via Digikey Inc., part numbers: 37704-ND, 37680-ND, 16-1448-ND, and 16-1231-ND). For each foam sheet, I punched out three circular pieces, each with a diameter of $\frac{1}{2}$ inch. An off-the-shelf anti-static foam was used as the sensing material due to its high electromechanical performance and strong adhesion to the FPC board. MWCNT doped foam's electromechanical performance could be tuned to the desired values for motility mapping application.

However, its poor adhesion with the Cu electrodes on the FPC prevent the MWCNT doped foam from being implemented in the sensing probe.

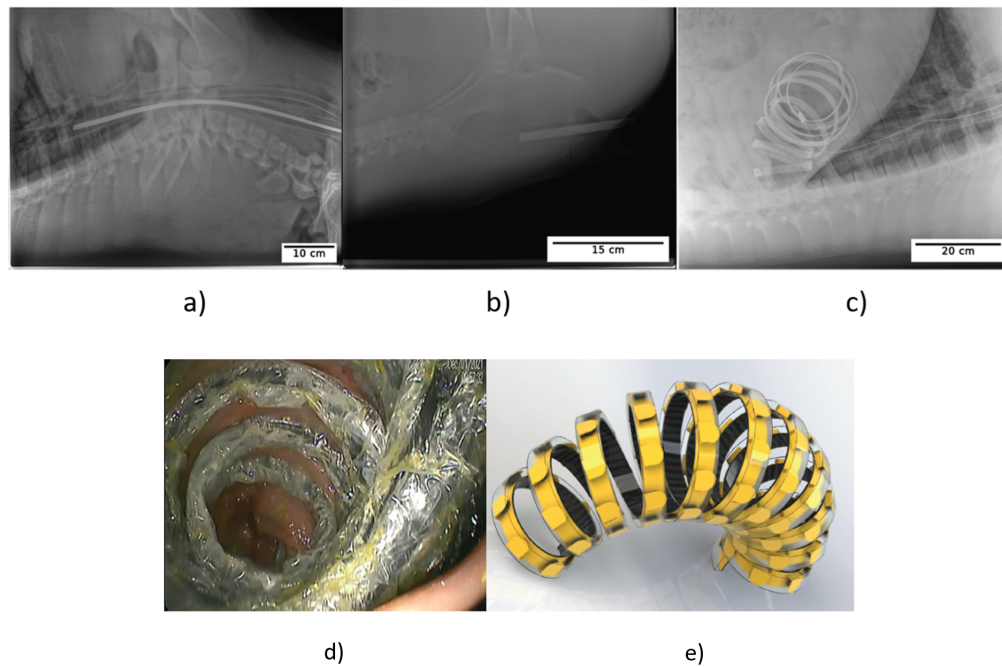


Fig. 2 X-ray of tubular probe in a) esophagus, b) rectum. c) X-ray and d) endoscope image of the bolus probe in the stomach. e) Illustration of the bolus organ (stomach) motility probe.

2.2.1 Fabrication and testing of three pressure-sensitive resistive polymers

1) SEBS (styrene and ethylene/butylene) and MWCNT film.

I added 0.25 g of MWCNT (US Research Nanomaterials, Inc. >95%, OD: <7 nm) and 50 mL of tetrahydrofuran (THF) in a glass jar. An ultrasound probe was used to disperse the MWCNT for 1 hour. I added 5 g of SEBS (KRATON G1643 V Polymer) polymer into the jar. It was magnetically stirred for 2 hours then cast onto a sheet of glass (Fig. 3 a). The thickness of a film applicator (doctor blade) was set to 500 μm and the mixture was spread on the glass sheet. The mixture was left to dry in a fume hood for 1 hour then it was peeled off the glass sheet. A 1 cm x1cm sample of SEBS film was taken and connected to a pair of soft electrodes. An Instron was used to load and unload forces (0-2.75 N, 0-206 mmHg correspondingly) on the sample. As can be seen from Fig. 3 b, the resistance of the SEBS film shows very little variation, so it was decided not to use SEBS+MWCNT film as the sensing material.

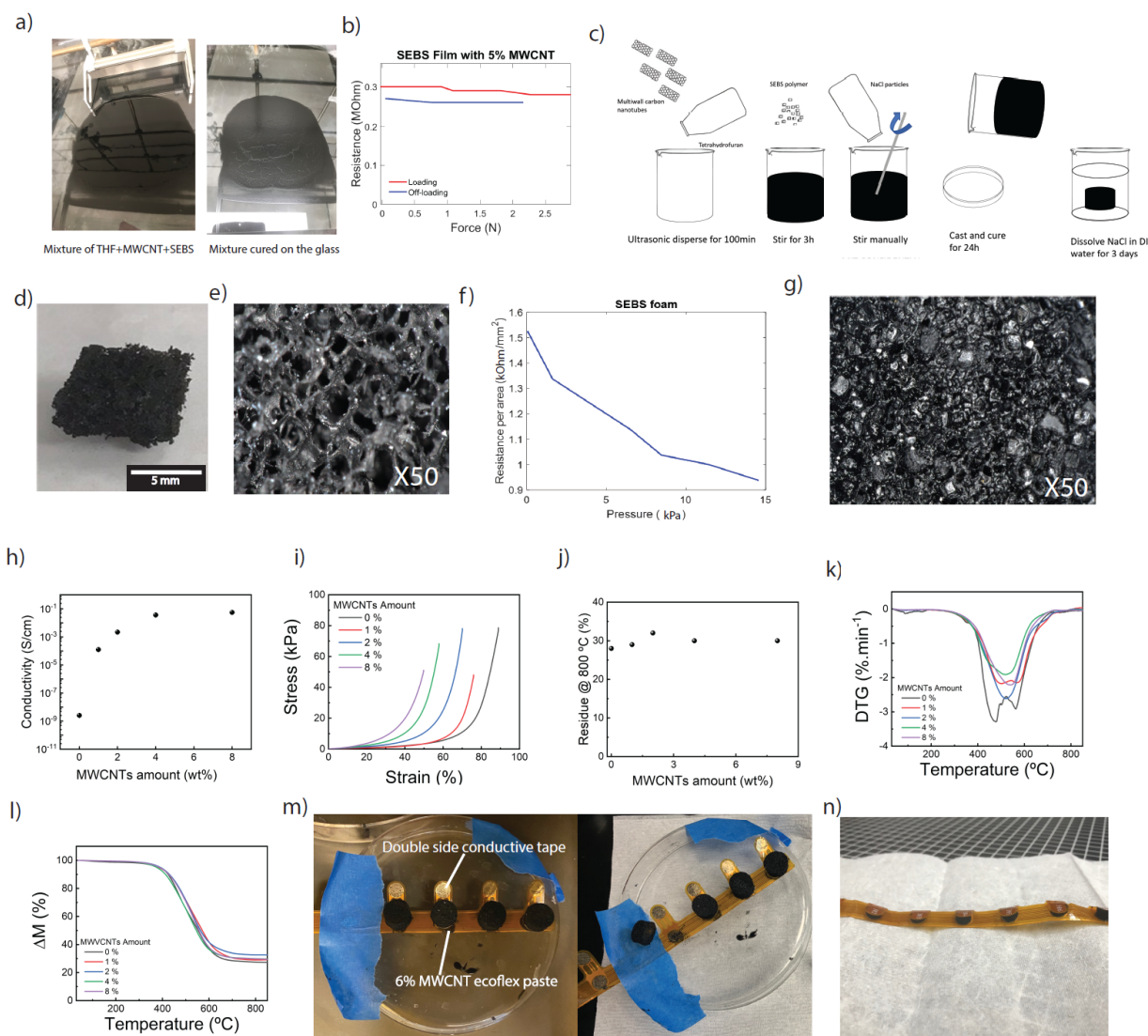


Fig. 3 a) Mixture of THF, MWCNT, and SEBS polymer cast on a glass sheet before (left) and after (right) drying for 1 hour. b) SEBS film resistance-force curve. Red line is the loading curve, and the blue line is the unloading curve. c) Fabrication workflow of SEBS+MWCNT porous foam. SEBS + MWCNT porous foam d) 1X and e) 50X magnified picture. f) Resistance-pressure curve of a 1cmx1cmx0.5cm SEBS + MWCNT porous foam, where the pressure was applied at the 1cmx1cm face. g) X50 magnification of the Eco-flex+MWCNT foam. h) Ecoflex foam conductivity vs MWCNT amount. i) Ecoflex foam stress-strain curves. j) Ecoflex residue graphs. The residue is the amount of carbon that was left at the temperature mentioned in the graph. k) Ecoflex TGA derivative. The derivative is the first derivative of the TGA plot, and shows the maximum degradation rate. l) Ecoflex thermogravimetric analysis. m) Ecoflex foam adhesion test. n) 16-1231 foam adhesion test.

2) SEBS and MWCNT porous foam.

The fabrication of SEBS and MWCNT porous foam is shown in Fig. 3 c. I added 0.25 g of MWCNT and 50 mL of THF in a jar. I covered the jar with foil and placed it in an ice bath and used an ultrasonic probe to disperse for 100 min. I then added 5 g of SEBS polymer into the jar and magnetically stirred it for 3 hours. NaCl particles (25g) were added and manually stirred until it was well mixed. I cast the new mixture onto a glass petri dish and left it to cure for 24 hours. I took the cured polymer into a DI water bath to

dissolve the NaCl for 3 days. The product is shown in Fig. 3 d and e. The sample shown in Fig. 3 d was sandwiched by a pair of electrodes and pressed on an Instron. The resistance-pressure relation of the sample is Fig. 3 f. It shows significant resistance variation within the range of pressure, 1.51-0.9 kOhm/mm² in 0-14.9 kPa. However, I found the brittleness of material causes unevenness along the edge (see in Fig. 3 d), which reduced its adhesiveness to FPC. I thus decided not to use this foam as the sensing material.

3) Eco-flex 00-30 and MWCNT porous foam

I then used Eco-flex 00-30 as the base material for the porous pressure-sensitive foam. I combined 2.5 g of Part A Eco-flex, 2.5 g of Part B Eco-flex, and various amounts of MWCNTs (0 – 8 wt%), then manually stirred with a spatula. Subsequently, 25 g of NaCl particles were added to the previous blend, stirred manually and the mixture was cast onto a glass petri dish and was left to cure overnight. I took the cured polymer into a DI water bath for 3 days. The product was left in the fume hood to dry at room temperature for 2 days. The final product is shown in Fig. 3 g. The foam formed a porous structure with a conductivity that was dependent on the amount of conductive filler added to the elastomeric matrix. A maximum of 5.6 S/m was achieved for the sample with 8 wt% MWCNTs (Fig. 3 h). It was observed that increasing the amount of conductive filler led to an increase on the mechanical stiffness of the Eco-flex foams (Fig. 3 i). Furthermore, the prepared nanocomposites were thermally stable up to 300 °C, followed by a decrease in the sample weight due to the volatilization of the Eco-Flex matrix (Fig. 3 l). It was found for materials doped with 0-8 wt% MWCNTs they all had $28 \pm 3\%$ residue at 800 °C (Fig. 3 j). The material without MWCNTs has around 28% of residue, when I add 8wt% MWCNTs, if it is pure physical interaction, I would expect that at 800 °C the polymer burns a residue of $28 + 8 = 34\%$. Instead, I have observed a 30% residue. It suggests that the MWCNTs could chemically interact with the polymer chains during the elastomer curing process. Fig. 3 k shows the rate of weight loss during the thermal weight loss experiment.

To adhere the foams onto the FPC, I tried both double-sided conductive tape and 6% MWCNT Eco-flex paste. As can be seen in Fig. 2.3 m, neither case showed good adhesion with FPC. In Fig. 2.3 n, I used double-sided conductive tape on 16-1231 foam and this combination showed good adhesion on FPC boards.

2.2.2 Screening of piezoresistive materials

A sourcemeter (Keithley 2450) was used to apply DC voltages across the anti-static foams and measure the resulting currents. The foams were loaded on an Instron (Universal Testing Machines) to determine their mechanical properties. I-V curves of four foams are shown in Fig. 4 a. Foam 16-1231 exhibits a linear I-V relationship. Its current changes linearly from -5 to +5 mA when the applied voltage changes from -10 to +10 V, while the other three foams exhibit very low conductivity. The foams' mechanical properties were

determined by applying a uniaxial compressive force onto each foam specimen (Fig. 4 b). The force was then subsequently converted into pressure by dividing the area of the sample as a ½ inch circle. The pressure was up to a maximum of 350 kPa. All foams exhibited three phases of deformation. In the first phase, I observed a linear strain change with stress increase. In the second phase, a plateau was observed with a large strain change along with relatively small stress increase. While in the third phase, the stress increases exponentially with very little strain change. This is due to the pore collapse and foam densification that occurs at higher strains.

The conductivity of the sample 16-1231 was superior to the other foams (Fig. 4 c). Sample 16-1231 had a conductivity of 10 S/cm, while other foams have significantly smaller conductivity. The foam 37704-ND had the highest Young's modulus value ($E = 754 \pm 24$ kPa), while the softer foam (16-1231-ND) had a value of $E = 180 \pm 22$ kPa (Fig. 4 d). In our application, the desired value for E is ~ 100 kPa because with a motility compression pressure ~ 40 kPa the material will have a significant deformation and thus a change of electrical resistance. The desired conductivity of the material is ~ 10 S/m. With this conductivity, the measured current would be ~ 1 mA because ~ 10 V of bias voltage is applied onto the sensing material. This amount of current is large enough for an accurate electrical resistance scanning (the resolution of current measurement is ~ 1 uA in the system) while maintaining the voltage below the dangerous threshold of 30V[178]. Based on the results, I concluded that the best candidate was the sample 16-1231-ND, with its low Young's modulus E (Fig. 4 c) and high electrical conductivity (Fig. 4 d). The gauge factor (GF) is defined as $GF = \frac{\frac{\Delta G}{G_0}}{\varepsilon}$, where $\frac{\Delta G}{G_0}$ is the normalized change in electrical conductance, and ε is the applied mechanical strain. The piezoresistive behavior of the foam 16-1231-ND exhibited good linearity up to 50% deformation, with a gauge factor (GF) value of 1.0 ± 0.4 (Fig. 5 a). The electromechanical behavior of the foam 16-1231-ND was assessed by applying a mechanical stress at 50 mm/min stroke speeds and monitoring the change in electrical conductance (Fig. 5 b). I studied the dynamic response of the sensor cell of a cyclic compression with a period of 1s. As can be seen in Fig. 5 b k, conductivity, stress, and strain show synchronized variations. Given the period of peristalsis/reflex in the GI tract is ~ 10 s, the sensor shows adequate response time.

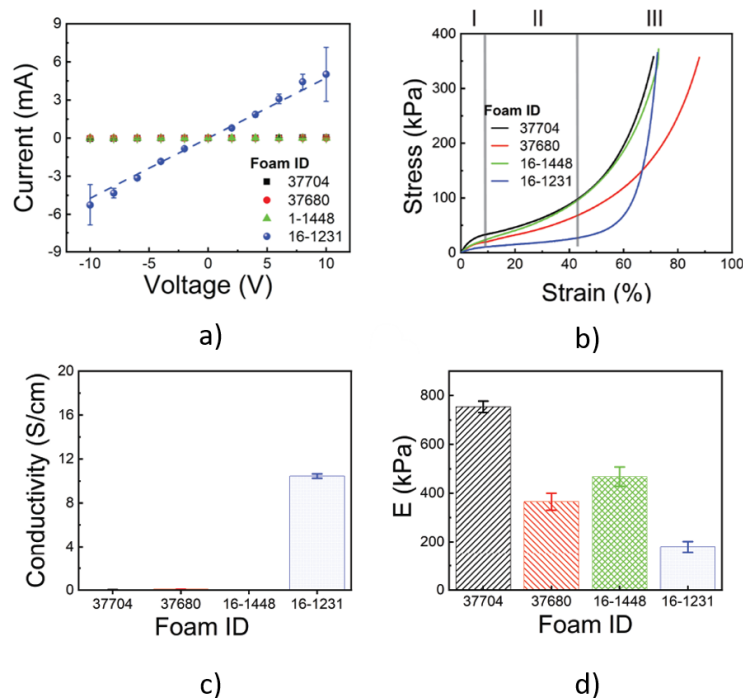


Fig. 4 a) I-V curves, and b) stress-strain relations of the 4 anti-static foams. Properties of four off-the-shelf anti-static packaging foams (37704-ND, 37680-ND, 16-1448-ND, and 16-1231-ND): c) conductivity, and d) Young's Modulus.

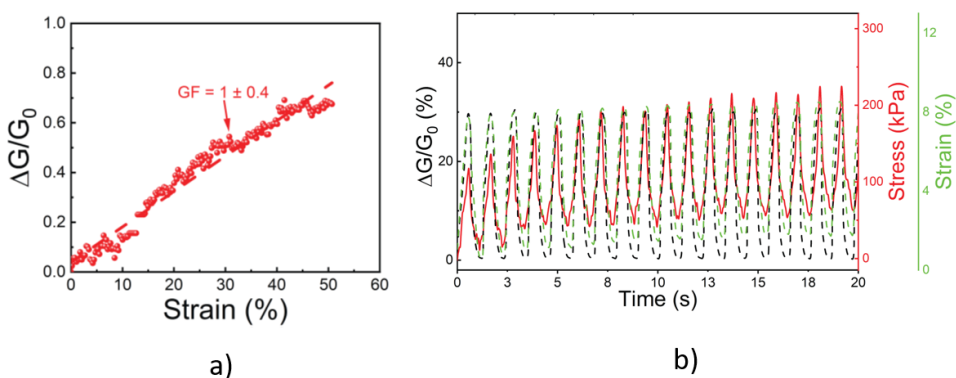


Fig. 5 a) Gauge factor of foam 16-1231. b) Mechano-electrical performance of the single sensor cell.

To understand the mechanism of this phenomenon, I first studied the microstructure of the foam and then characterized the electromechanical characteristics of the foams. As can be seen from the scanning electron microscopy (SEM) images in Fig. 6 a, all four foams exhibit a porous structure, with the pore diameter of 0.5-1 mm. The 3D morphology was evaluated using a 3D model from CT scan imaging data with 3 μ m resolution (Fig. 6 b). All foams had a porosity of over 90%. The morphology and the porosity data helped us to build a hypothesis of anti-static foams' mechanism of detecting mechanical pressure. In the neutral state, where there is no pressure applied on the foam, the electrons flow through the skeleton of the foam. Once the foam experiences stress, the porous structure collapses and contacting points are created inside

the foam. With a larger stress, more contacting points are created, thus the electrical resistance of the foam decreases.

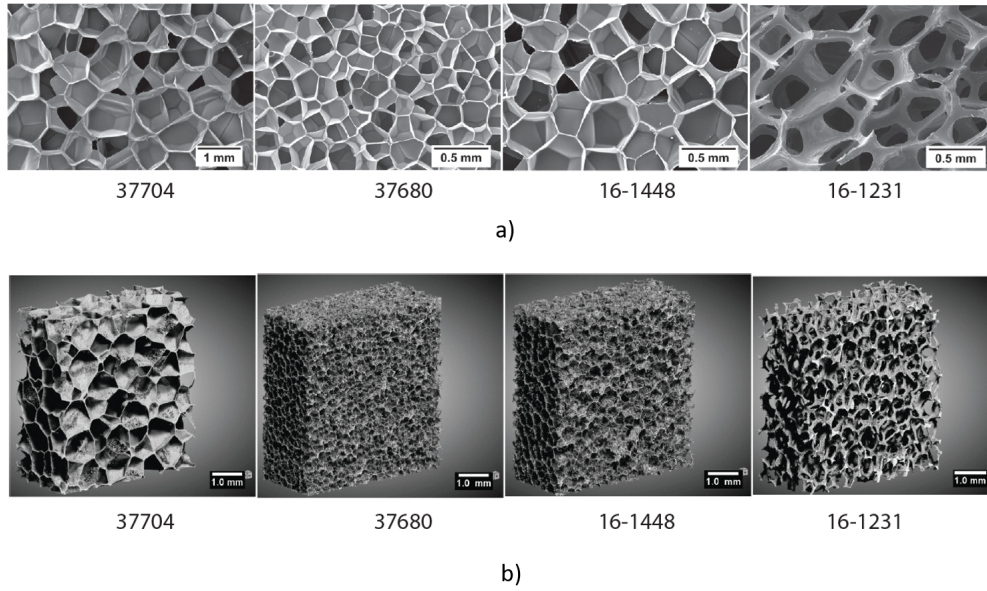


Fig. 6 Properties of four off-the-shelf anti-static packaging foams (37704-ND, 37680-ND, 16-1448-ND, and 16-1231-ND): a) SEM images, b) Micro CT.

2.2.3 Single sensor cell twin spring model and single sensor cell design optimization

A twin-spring model is developed to optimize the geometric parameters of the sensor cell, where the foam is modeled as a linear spring connected in parallel with the FPC modeled as a U-turn spring. As can be seen from Fig. 7 a-b, when an external force is applied to the sensor cell, the foam and the U turn both resist compression. Thus, they can be modeled as two springs connected in parallel. Assuming the foam is a homogenous material with a constant cross-sectional area, its spring constant can be calculated as follows:

$$k_{foam} = \frac{E_{foam} A_{foam}}{h_{foam}} \quad Eqn. 1$$

where E_{foam} is the Young's modulus of the foam, A_{foam} is the cross-section area of the foam, and h_{foam} is the height of the foam. The FPC U-turn can be modeled as an flat U-turn spring model[179], whose equivalent spring constant is:

$$k_{fpc} = \frac{8B}{h^3} \quad Eqn. 2$$

$$B = \frac{Wt^3 E_{fpc}}{12(1-\nu^2)} \quad Eqn. 3$$

where h is the height of the U turn, W is the width of the single sensor cell, t is the thickness of the FPC, E_{fpc} and ν are Young's modulus and Poisson ratio of the FPC material polyamide [180], [181]. The force F

applied on the sensor is related to the pressure the sensor experiences and the area where the pressure is applied. When the sensor is compressed to have a smaller height h , more area is delivered under the compressor. This is illustrated at the left panel of Fig. S3 a. F is expressed as:

$$F = P \left[A + \frac{W}{2} \left(L - \frac{\pi h}{2} \right) \right] \quad \text{Eqn. 4}$$

where P is the pressure, A is the area of the FPC top pad, W is the width of the FPC, $(L - \pi h/2)/2$ is the length of the U-turn in Fig. 7 a, on side of facing the pressure. For a given height h , the increase of force F and pressure P can be written as Eqn. 5. In the twin spring model, the total spring constant of the sensor is expressed as Eqn. 6 considering the foam and the U-turn are working in parallel. By having F divides spring constant k , I obtain Eqn. 7 where the height h and pressure P are related.

$$dF = d \left\{ P \left[A + \frac{W}{2} \left(L - \frac{\pi h}{2} \right) \right] \right\} \quad \text{Eqn. 5}$$

$$k = k_{fpc} + k_{foam} \quad \text{Eqn. 6}$$

$$-dh = \frac{dF}{k} = \frac{d \left\{ P \left[A + \frac{W}{2} \left(L - \frac{\pi h}{2} \right) \right] \right\}}{\frac{8B}{h^3} + k_{foam}} \quad \text{Eqn. 7}$$

Taking the integration of Eqn. 7 and applying the initial condition as $h = h_0$, $P = 0$, the relation of height h and pressure P is expressed as:

$$-\frac{(ac^3 + b^3d) \log(b - ch)}{b^3c} - \frac{a(b + 2ch)}{2b^2h^2} + \frac{ac^3 \log(h)}{b^3} = -P + Const \quad \text{Eqn. 8}$$

$$\left(\frac{ac^3}{b^3} + \frac{d}{c} \right) \log \left(\frac{b - ch}{b - ch_0} \right) + \frac{a(b + ch)}{2b^2h^2} - \frac{a(b + 2ch_0)}{2b^2h_0^2} - \frac{ac^3}{b^3} \log \left(\frac{h}{h_0} \right) = P \quad \text{Eqn. 9}$$

Where the constants are:

$$a = 8B$$

$$b = A + \frac{WL}{2}$$

$$c = \frac{\pi W}{4}$$

$$d = k_{foam}$$

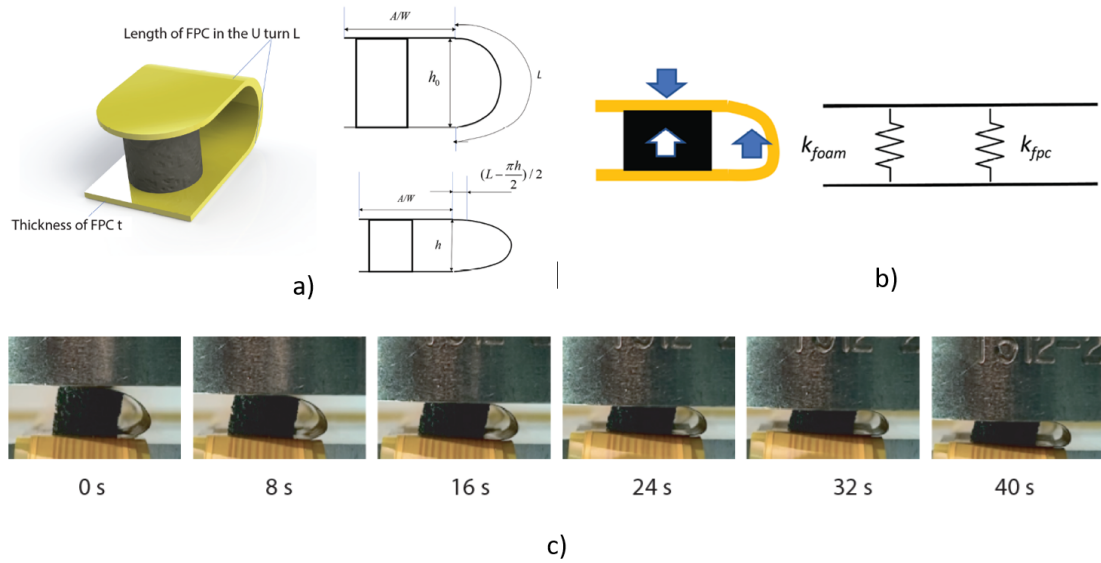


Fig. 7 a) Illustration of a single pressure sensing cell. b) Twin spring model of the single sensor cell. c) Single cell under compression test on the Instron platform.

To evaluate the electromechanical properties of the conductive foam, two electrodes were connected to the top and bottom part of the sample and its resistance was recorded as a mechanical compressive force was applied (Fig. 7 c). During the foam compression, the pores collapse and more pathways for electrons to migrate are created, leading to an overall increase in conductivity as mechanical strain is applied. The model is verified by observing the mechanical behavior of the sensor cell (Fig. 7 c). When the sample is compressed, the foam cell shrinks in height and behaves like a linear spring, and the diameter of the U turn gets smaller.

Based on manometry measurements in previous studies, GI motility can result in a pressure change of up to 250 mmHg [182]; as such, I looked for a soft material capable of undergoing a large thickness change when subjected to a pressure in the range of 0-250 mmHg. According to our model, as shown in Fig. 8 a, only the FPC with $t = 0.1$ mm case shows a significant change of thickness of 2 mm when subjected to a pressure of 250 mmHg. The other three cases of $t = 0.2$, 0.3, and 0.4 mm have little to no thickness change, suggesting that the sensors are too mechanically stiff to reflect the pressure change. Using $t = 0.1$ mm while changing L , I found that the U-turn length, L , does not significantly affect the sensor stiffness defined as thickness response to the change of stress, as can be seen in Fig. 8 b. To verify this model, I converted the pressure applied to the sensor into force (N) and plotted sensor thickness under different forces in Fig. 8 c. The thick blue line is made up from the experimental data where I compressed a $t = 0.1$ mm and $L = 1$ cm sensor cell with three strokes on a mechanical tester apparatus. The model and experimental data showed alignment in the $t = 0.1$ mm case. So, I confirmed the optimal parameters were foam 16-1231, with $t = 0.1$ mm and $L = 1$ cm. I also conducted life-time tests of sensor cells with a stroke speed of 5 mm/min for 1000

cycles, 5 mm/min for 10,000 cycles, and 50mm/min for 10,000 cycles (Fig. 8 d). The lifetime test indicates that the sensor will be able to operate for at least 24 hours in an *in vivo* setting, given it can survive 10,000 cycles and the period of contract in the GI tract is ~ 10 s.

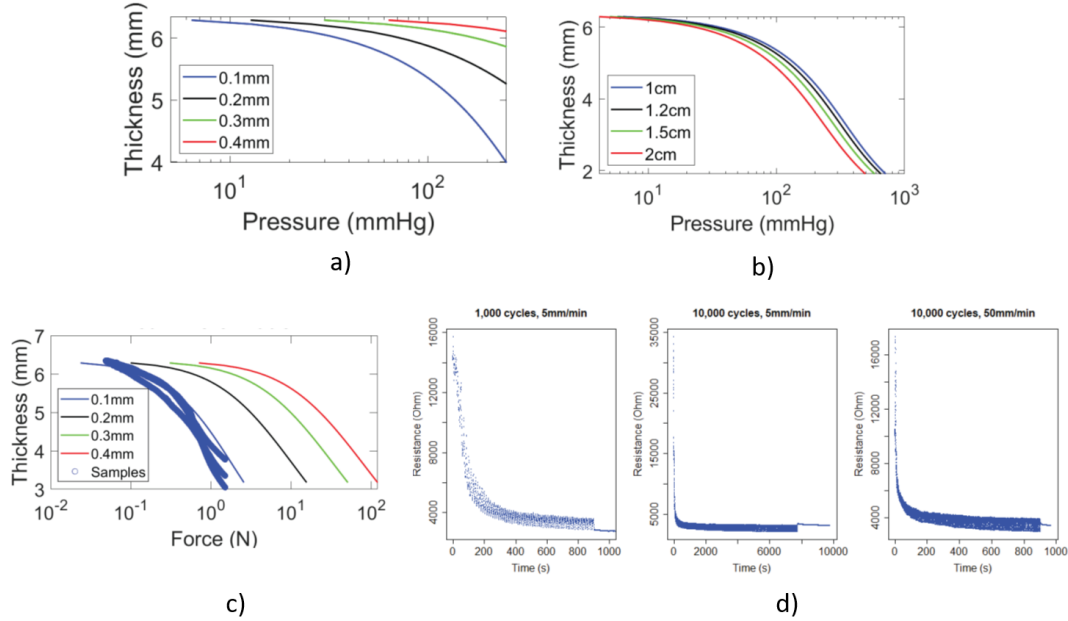


Fig. 8 Single sensor cell's mechanical deformation-pressure relationship a) $L = 1\text{cm}$ with different thicknesses t b) $t = 0.1\text{mm}$ with different lengths L . c) Single sensor cell's mechanical deformation-force relationship with $L = 1\text{cm}$ with different thicknesses. The experimental data was obtained from an Instron platform by pressing the sensor cell with $t = 0.1\text{mm}$ for three cycles, and the data points were plotted as blue hollow circles. d) Lifetime tests of the single sensor cell.

2.3 Self-aligned supporting structure for motility probes

The probes use the shape memory alloy Nitinol as the supporting structure material. The Nitinol strips used for the esophagus and rectum probes are 1 mm thick, 12 cm (rectum probe) or 54 cm (esophagus probe) long. Using the dimensions measured from a swine stomach (Fig. 9 a), I found that to have a 2-cm resolution of pressure mapping in the stomach, similar to FDA approved manometry's resolution (22), there should be ~ 90 sensing units. Thus, I designed a coil-like structure 180 cm long. The challenge in building a conformal supporting structure is achieving an appropriate axial stiffness while minimize radial stiffness. Axial stiffness is the structure's ability to expand inside stomach against its weight (Fig. 9 b). The probe needs to be stiff enough axially to expand across the stomach. Radial stiffness is the structure's ability to push against the surrounding stomach tissue (Fig. 9 b). The probe's radial stiffness needs to be minimized so the probe can adapt to subjects with different stomach shapes/sizes. The supporting structure with 0.5mm thickness is then fabricated and integrated with the sensor belt. The probe is stiff but flexible, which allows it to be stretched, or compressed for adaptation purposes (Fig. 9 c-d). I then deployed the same supporting

structure into animals with different body weights. Fig. 2 c, Figs. 9 e and f are X-rays images of the supporting structure in swine of body weight 103 kg, 89 kg, and 90 kg, respectively. One can see the supporting structure has aligned by itself and adapted to stomachs of different subjects.

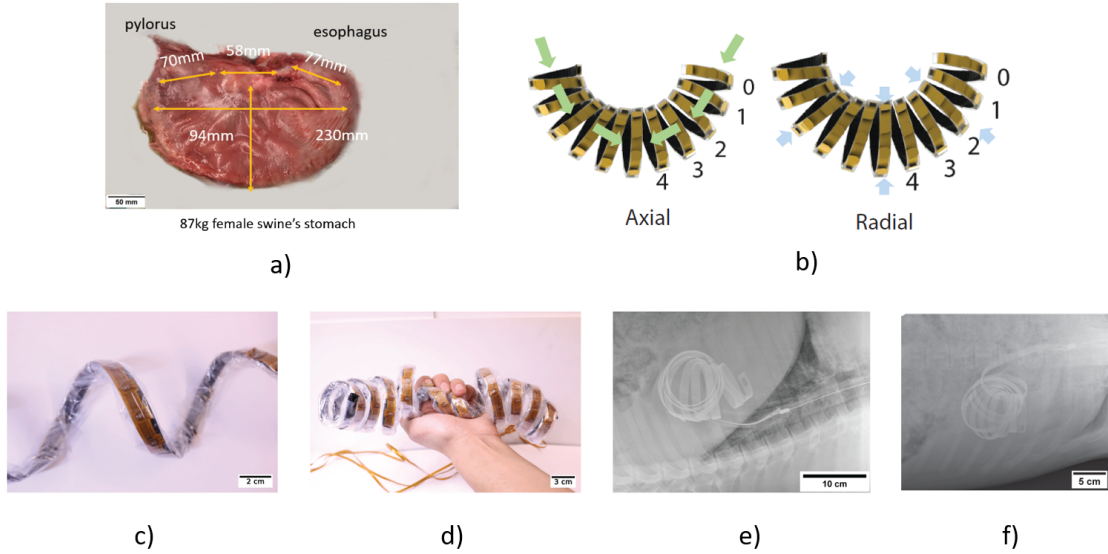


Fig. 9 a) Stomach of a swine with dimension measured. b) The illustration of axial and radial forces bolus probe experienced inside the stomach. c) Stomach probe being extended. d) Stomach probe being crushed by hand. X-ray of supporting structure inside the stomach of e) 89kg and f) 90kg pigs.

2.3.1 Globular supporting structure mechanical model of axial stiffness

A mechanical model to describe the axial stiffness of the supporting structure was developed. Each turn in the coil is modeled as a spring, which will resist the weight of the sensor system above it, as can be seen from Fig. 13 a. The spring constant of each turn is [183]:

$$k_i = \frac{\beta E b t^3}{D^3} \quad \text{Eqn. 10}$$

$$\beta = 0.4$$

Since each turn inside the coil structure works as a helical spring, it needs to support the structure and fight against the weights of every other turns above itself. The weight of each turn is w_i , and $g \cos \theta_i$ is the projection of gravity vector onto the axis of each turn. Summing all the weights and dividing the axial spring constant k_i , the change of length of each turn n due to the weight of sensor system is δ_n :

$$\delta_n = \frac{\sum_{i=0}^{n-1} w_i g \cos \theta_i}{k_n} \quad \text{Eqn. 11}$$

$$\delta_n < \delta_n^{max} = \frac{\sum_{i=0}^{n-1} w_i g}{k_n} \quad \text{Eqn. 12}$$

Notice that in the *in vivo* environment, the projection of gravity vector onto the axis is depending on the pose of the subject. To ensure the structure will have sufficient axial stiffness, I used the maximum possible compression length δ_n^{max} in the calculation in which $\theta = 0$ Deg. Nitinol sheets with a transition temperature of 35 °C and thicknesses of 0.1, 0.25, 0.5, and 1 mm were selected. The width of the strip was set at 1cm in order to fit inside an overtube with a diameter of 1.5cm. As seen in Fig. 13 b, when the device has a weight of 100g/m, a 0.1mm thick device fully collapses. For devices with thickness 0.25mm, 0.5mm, and 1mm have open angles of, respectively, 100, 175, and 179 deg, as illustrated in Fig. 13 c. I found the optimal thickness to be 0.5mm, since it allows a large open angle (expansion across the stomach) with the smallest thickness.

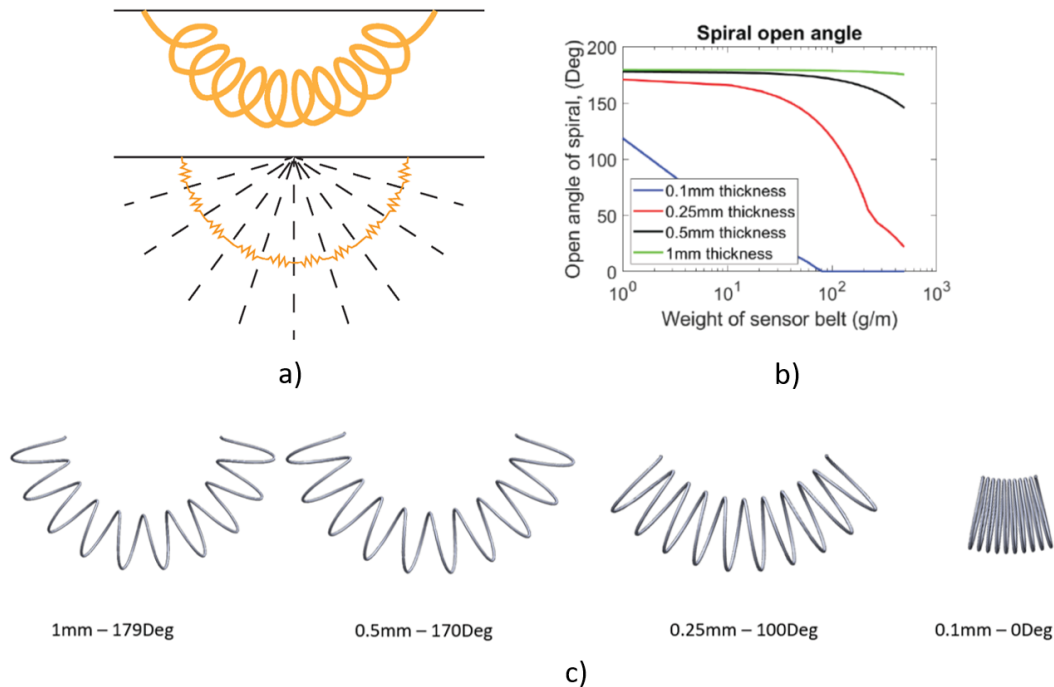


Fig. 10 a) Axial stiffness model illustration. b) Axial stiffness model result. c) The illustration of the open angle at 100g/m with different Nitinol thickness.

2.3.2 Radial stiffness of the stomach bolus supporting structure

A model to predict the radial stiffness of the bolus supporting structure is illustrated in Fig. 11 a. First, I want to build a relationship between the internal torque inside the coil and the pressure P applied on the circumference of the coil. When the coil turns over a small angle $d\theta$ caused by the circumference force, the work stored into the internal stress is $Md\theta$. This increase of energy is caused by the volume work done by

the pressure P , which is $PW\pi Ddr$, where W is the width of the coil, D is the diameter of the turn, and r is the radius of this turn. According to the principle of virtual work, the energy done by the volume work should be the same as the energy stored in the coil. I also have the relationship of $d\theta$ and dr given the length of the coil doesn't change: $(2\pi + d\theta)(r + dr) = 2\pi r$, $d\theta = -2\pi dr/r$. Here I neglect $d\theta dr$ in the derivation. So a relationship was established between internal torque in a turn of the supporting structure and the external pressure from the principle of virtual work:

$$\sum d(\text{Work}) = Md\theta + PW\pi Ddr = 0, \quad \text{Eqn. 13}$$

$$M = \frac{PWD^2}{4}$$

where M is the internal torque and P is the pressure applied on the structure. For each turn, it is modeled as a coil spring [184] where I can obtain the relationship between M and angle θ , the angle it has turned over neutral state:

$$M = \frac{\pi Ebt_c^3\theta}{6L} \quad \text{Eqn. 14}$$

L is the total length of the coil spring, b is the width of the spring, t_c is the thickness of the spring, E is the Young's modulus of the material. θ can be expressed as:

$$\theta = 2\pi(N_t - 1) \quad \text{Eqn. 15}$$

where N_t is the total number of turns in the new state. The total length of the turn studying is:

$$L = \pi N_t D \quad \text{Eqn. 16}$$

The total length of this turn is the same before and after it is experiencing pressure, thus:

$$D\pi N_t = D_0\pi \quad \text{Eqn. 17}$$

By substituting Eqn. 14-17 into Eqn. 13, I have the relationship between the diameter of the coiled probe and the external pressure:

$$\frac{3PWD_0^3}{4\pi Ebt_c^3} \left(\frac{D}{D_0}\right)^3 + \frac{D}{D_0} = 1 \quad \text{Eqn. 18}$$

I conducted a series of experiments to measure the radial stiffness of the bolus supporting structure, and the pressure measuring device is shown in Fig. 11 b. The measuring device was composed of a hand pump (orange arrow), a rigid plastic straw (pink arrow), and plastic tubing (green arrow) whose ends were secured with hose clamps (yellow arrows). I also laser cut a fixture (red arrow) to ensure only one turn was being measured during each trial. The plastic tubing was used to record the change of pressure. The setup is shown in Fig. 11 c. First, I placed the coil into a 40-degree Celsius water bath. Then, I measured the relationship between pressure and diameter on each individual turn. On each turn, I stabilized the turn between the disks of the laser cut structure by adding a ring inside. I wrapped the measuring device around the turn and secured a hose clamp around it. The plastic tubing was inserted between the hose clamp and the coil. In

each trial, I measured the starting diameter at a low pressure. Then, I tightened the hose clamp screw to decrease the diameter. The coil was forced to have a smaller diameter because of the pressure applied by the hose clamp. I measured the air pressure and diameter at regular intervals until the maximum pressure was reached. Then, I released the air by pressing the releasing button on the hand pump. I repeated this process three times.

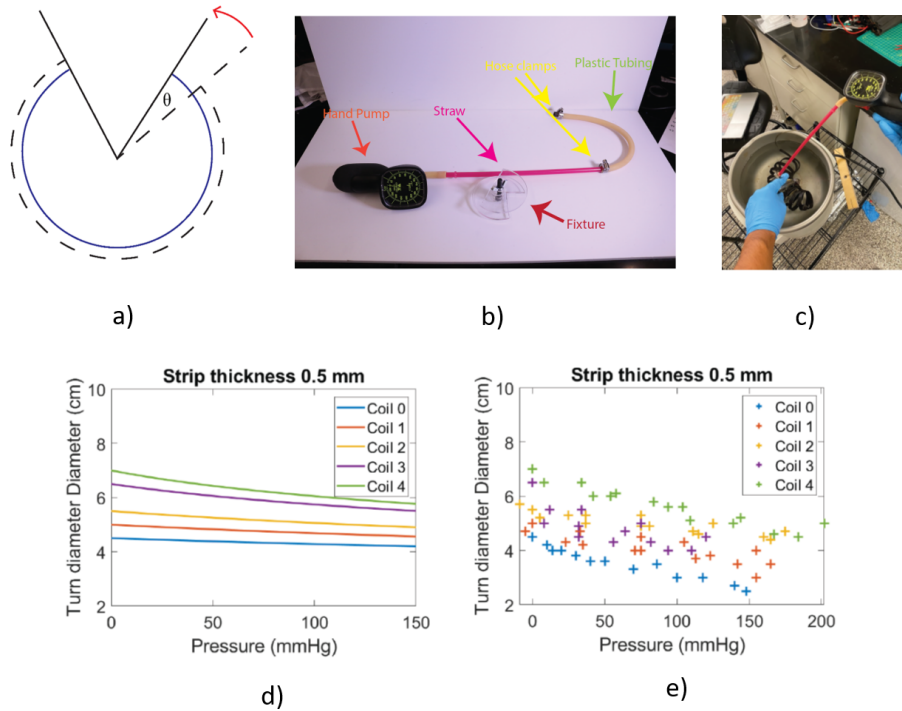


Fig. 11 a) Radial stiffness model illustration. b) A photo of the pressure measuring device for the radial stiffness measuring experiment. c) Radial stiffness measuring setup. d) Radial stiffness model result. d) Change of diameter of each turn when a uniform load is applied on to the supporting structure. Each cross refers to a data point obtained from the radial stiffness testing experiment. e) Stomach probe being extended.

In the coil spring model of radial stiffness, the diameter of each turn is a function of the pressure uniformly applied to the coil which comes from the gastric wall, and the result is shown in Fig. 11 d. In the experimental data, as shown in Fig. 11 e, one can see from 0 to 150mmHg, the diameter of each turn is reduced by ~2cm. Considering the diameter of a 75-100 kg swine's stomach is 4-7 cm, the supporting structure can reduce total diameter by 50-30% when the maximum possible pressure is applied. This indicates that the radial stiffness of the supporting structure is sufficiently small.

2.3.3 Friction Forces in the Overtube

To ensure the safety of the intervention, It is important to understand the frictional forces during the deployment and retrieval processes. To estimate the force required to insert and extract the coiled sensor

belt through the overtube, a simplified model is devised based on the helical nature of the sensor belt: the force required to extract or insert the sensor is equal to the force required to overcome the friction between the wall of the overtube and the coiled probe, which is obtained from the radial force exerted by the sensor probe to the wall of the overtube, and a friction coefficient. The whole coiled sensor belt, which has 10 turns, is modeled as 10 helical springs connected in series in which each spring represents one turn of the actual coil. (Fig. 12 a) Each modeled spring's diameter equals the major diameter of the corresponding turn of the relaxed sensor belt. The spring element has a rectangular cross section with thickness of 0.5 mm and width of 10 mm.

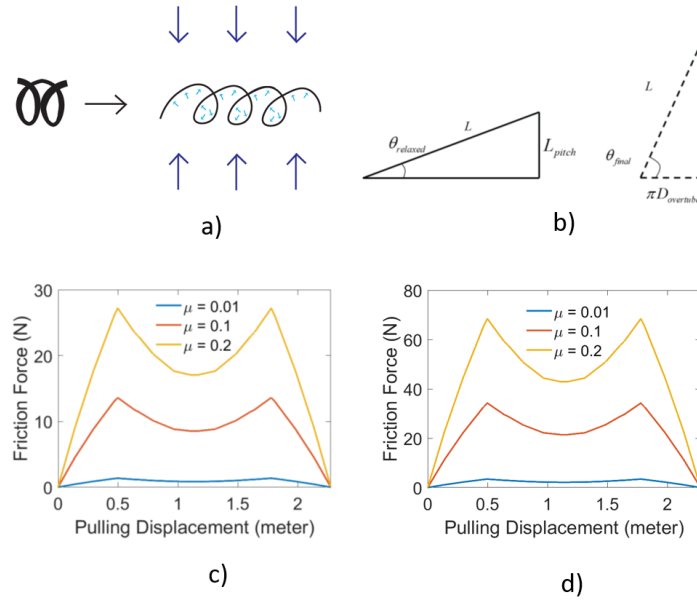


Fig. 12 a) Friction model illustration. b) The relaxed and final angle illustrations. Expected friction in the overtube when the supporting structure is c) below or d) above transition temperature of Nitinol which is 35 Celsius.

The torque required to impose a twist of angle θ can be expressed as in Eqn. 19. In which G is the torsion modulus, J is the area inertia of the sensor belt and L is the straightened length of the sensor-belt forming this turn. The angle of twist is calculated from the change of pitch angle as shown in Eqn. 20 (Fig. 12 b).

$$T = \frac{GJ\theta}{L} \quad \text{Eqn. 19}$$

$$\theta = \theta_{final} - \theta_{relaxed} = \sin^{-1}\left(\frac{L_{pitch}}{L}\right) - \cos^{-1}\left(\frac{\pi D_{overtube}}{L}\right) \quad \text{Eqn. 20}$$

In order to simplify the model, this model assumes that the compression applied to a specific turn of the coil linearly distributes along the length of this turn. As the coiled sensor belt is squeezed into the overtube, its diameter is forced to decrease from relaxed diameter to the diameter of the overtube. As the deformation of the spring is purely torsional per the assumptions above, the energy method is employed to relate the internal torque on the belt and the radial force applied by the overtube, as shown in Eqn. 21.

$$T \Delta \theta = F \Delta R \quad \text{Eqn. 21}$$

When the coiled sensor belt is pulled into the over-tube, the coil's diameter must be the same as the inner diameter of the over-tube, D . By modeling each turn of the spring as a loop and letting f be the force density (N/m) acting on the outer diameter, the relationship between the change in radius, dR and the change in twist angle, $d\theta$ of each turn of the spring can be expressed as in Eqn. 22.

$$T \cdot d\theta = f \pi D \cdot dr \quad \text{Eqn. 22}$$

Naturally, twisting the coiled spring decreases its diameter. Since the whole spring is assumed to be twisted uniformly, the relationship between $d\theta$ and dR can also be expressed as in Eq. 23-25. Here, r_0 represents the radius of the loop prior to the imposition of $d\theta$ and r_1 represents the radius of the loop after $d\theta$ have been imposed.

$$r_1 (2\pi + d\theta) = r_0 \cdot 2\pi \quad \text{Eqn. 23}$$

$$r_1 \approx r_0 \left(1 - \frac{d\theta}{2\pi} \right) \quad \text{Eqn. 24}$$

$$dr = r_0 - r_1 = r_0 \frac{d\theta}{2\pi} \quad \text{Eqn. 25}$$

By substituting Eqn. 25 into Eqn. 22, the relationship between the torque and the radial force per unit loop length can be expressed as in Eqn. 26-27 where I also use $r = D/2$ where D is the diameter of the turn.

$$T = \frac{f \cdot D^2}{4} \quad \text{Eqn. 26}$$

$$f = \frac{4T}{D^2} \quad \text{Eqn. 27}$$

Finally, the friction between the wall of the over-tube and the coiled sensor for each coil can be expressed as in Eqn. 28 in which μ represents the friction coefficient between the inner wall of the over-tube and the coiled sensor belt where the turn is confined into a tube with diameter D_{overtube} , and $D = D_{\text{overtube}}$.

$$F_f = \mu \frac{4\pi T}{D_{\text{overtube}}} \quad \text{Eqn. 28}$$

In order to calculate the force required for sensor insertion and extraction as a function of the length of the sensor belt inside the stomach, a further assumption is made that the friction is constant within each turn of the coil. F_f is retro-fitted to f_f , the friction per unit length of the sensor belt, and linearly interpolated along the length of the sensor belt. f_f is then integrated for the length of the sensor belt within the over-tube to obtain the force required to overcome the static friction at each point of displacement and plotted as in Fig. 12 c and d. Fig. 12 c shows the friction when the structure is in the martensite phase (below the phase transition temperature) and pushed into the overtube. The frictional force reaches a maximum value of 27 N with a coefficient of friction of 0.2. Fig. 12 d shows the frictional force when the supporting structure is in the austenite phase (above the phase transition temperature) and removed through the overtube. In the austenite phase, the maximum friction force reaches 70 N with a coefficient of friction of 0.2. In both cases,

the maximum frictional force is proportional to the coefficient of friction. Our findings have two implications: 1) The device must be well lubricated in both the deploying and retrieval processes. In the *in vivo* experiment, I used an edible oil spray (PAM Cooking Spray) to create an oil-rich environment in the overtube. 2) In the deploying process, I needed to ensure the transition from the martensite to austenite phase would not occur before reaching the stomach.

2.3.4 Heat transfer model of the supporting structure in the deploying process

A heat transfer model was developed to study the temperature of the device as a function of the time in the body of the swine (Fig. 13 a). The body temperature of the swine is 38.6-39.2 degree Celsius.[185] To understand the heat transfer process, I first used a thermal resistance network to model the transfer of heat in the sensing probe. A cross-section of the sensor probe is shown in Fig. 13 b and its corresponding thermal resistance network is shown in Fig. 13 c. On the sensor probe, sensor units of 1cm width are equally spaced by 2cm of period. On the side with sensor units, there are 1cm wide air pockets sandwiched by the sensors. Here I consider the heat resistances at the side with sensing units and the opposite side where there are no sensing units. Notably, the Biot number along the thickness of the strip is 0.005 while the Biot number along the length is 8.98. This means the internal heat resistance along the thickness of the Nitinol strip is very small compared with the external heat resistance. On the other hand, the heat resistance along the length of the Nitinol is large compared with external heat resistance. The probe will reach a relatively uniform temperature distribution along its thickness but the temperature difference along its length will be significantly greater. This is because the heat resistance along the length is one order of magnitude larger than the outer layer heat resistance. As such, the strip will not be able to reach a relatively uniform temperature distribution along its length. With this insight, I built a heat transfer model of the strip with assumptions: 1) The temperature across the thickness is uniform; 2) The body of the swine is an infinite heat reservoir; 3) Along the length the strip is adiabatic and thus each part can be analyzed individually. The governing equation of one piece of probe is:

$$c \frac{dT}{dt} = \frac{T_{body} - T}{R} \quad Eqn. 29$$

Where c is the heat capacity of Nitinol in the cross section per unit length. It has a unit of $\frac{J}{mK}$. T is the temperature of the Nitinol. The specific heat resistance R with a unit of $\frac{Km}{W}$ is:

$$R = \frac{1}{\frac{1}{R_{foam\ side}} + \frac{1}{R_{foam\ without}}} \quad Eqn. 30$$

To simplify the equation, I use the relative temperature theta:

$$\Omega = T - T_{body} \quad \text{Eqn. 31}$$

The temperature of a piece of Nitinol strip in after time t in the body is:

$$\Omega = \Omega_0 \exp\left(-\frac{t}{Rc}\right) \quad \text{Eqn. 32}$$

where the initial condition is applied.

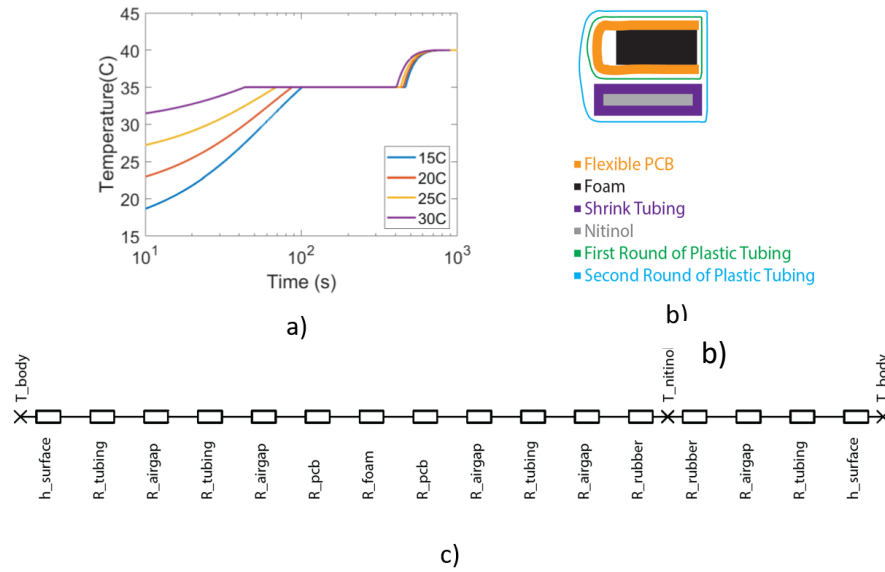


Fig. 13 a) Temperature of the supporting structure as a function of time in the overtube. Note the initial temperatures are four possible room temperatures where the probes are stored. b) Cross section illustration of the sensor cell for heat transfer model. c) Thermal resistance network of the single sensor cell.

The plateau in the graph (Fig. 13 a) is the period when the device reaches the transition temperature. The heat is absorbed into the material as latent heat to drive the phase transition. Before the plateau, the device's temperature rises from the initial room temperatures, set at 15, 20, 25, and 30 °C. To minimize friction and prevent the probe from undergoing phase transition in the overtube, the probe needs to reach the stomach before t_p , which is when the phase transition starts. With an overtube length of 0.5 m, the total allowable delivery times with different initial room temperatures are shown in Table 4.

Table 4 Maximum time to prevent phase transition in overtube in the *in vivo* experiments.

Room temperature (Celsius)	t_p (s)	Maximum allowed delivery time (min)
15	100	4.7
20	90	4.2
25	85	4
30	40	2

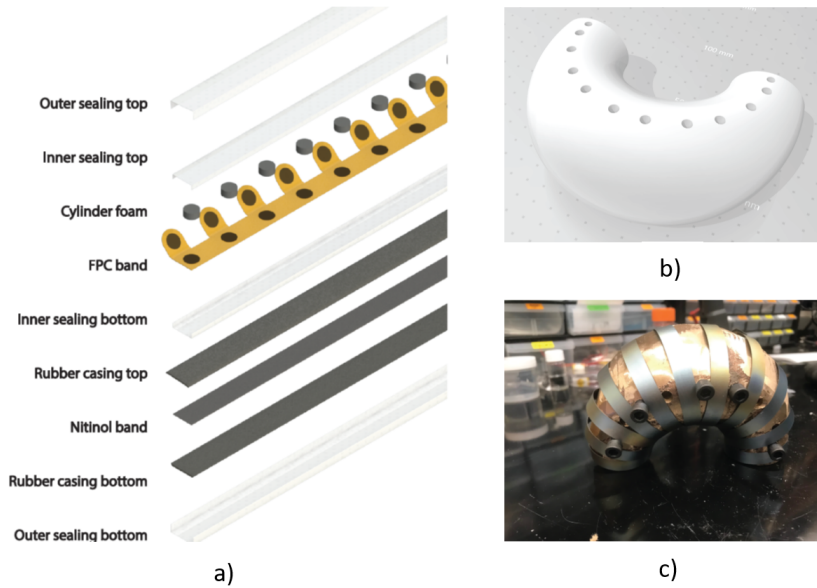


Fig. 14 a) Exploded view drawing of motility probe. b) CAD file of the fixture for Nitinol shape-programming. c) Picture of riveted band on the bronze fixture.

2.4 Sensor probe prototyping and integration with supporting structure

Each of the probes has a linear pressure sensor system composed of a flexible printed circuit (FPC), a Nitinol strip as the supporting structure, and two layers of sealing for impermeability (Fig. 14 a). The probes require no microfabrication nor clean room process. The fabrication process of the globular supporting structure of the stomach probe is shown in Fig. 3 g. Esophageal and rectal probes have the same fabrication process. A Nitinol sheet 1m long, 50cm wide, and 0.5mm thick was purchased from Kellogg’s Research Labs. A water jetting bed (OMAX) was used to cut two 95cm long, 1cm wide strips from the sheet. The two strips were then riveted together. A CAD model of the fixture was made on Fusion 360, and the manufacturing G code was exported from it. A Tormach 440 CNC mill was used to mill the fixture out of a rod of plastic. The plastic fixture was used for sand casting the bronze fixture. The bronze fixture was then drilled and tapped with thread holes (Fig.14 b). The riveted strip was fixed onto the bronze fixture via bolts (Fig. 14 c). Then the entire structure was placed in the furnace at 600C for 1 hour to program the shape of the Nitinol. The supporting structure was then inserted into ½ inch shrink tubing (WindyNation 100 Feet 1/2 inch). A heat gun was used to heat the tubing and make a tight cover on the Nitinol supporting structure. This was done to prevent the edges from tearing the sealing layer. Double sided conductive tape (3M 2-5-9719) was applied on both sides of the 16-1231 anti-static packaging foam sheet. A puncher with diameter ¼ inch was used to punch foam cylinders from the double-sided packaging foam. The foam cylinders were then placed on the FPC sensor band after peeling off the cover of the double-sided tape. The assembled sensor band was placed inside a 1-inch diameter low density polyethylene (LDPE) tubing (Uline S-3520).

The tubing was then adhered to the supporting structure using non-conductive double-sided tapes. Another layer of LDPE was then placed over the entire structure. 40g of well mixed Ecoflex 00-20 silicone mixture was injected into the space between two layers of LDPE tubing. The probe was left in the lab overnight under room temperature to allow the silicone to cure. The probes are all tested and calibrated on bench before conducting *in vivo* experiments.

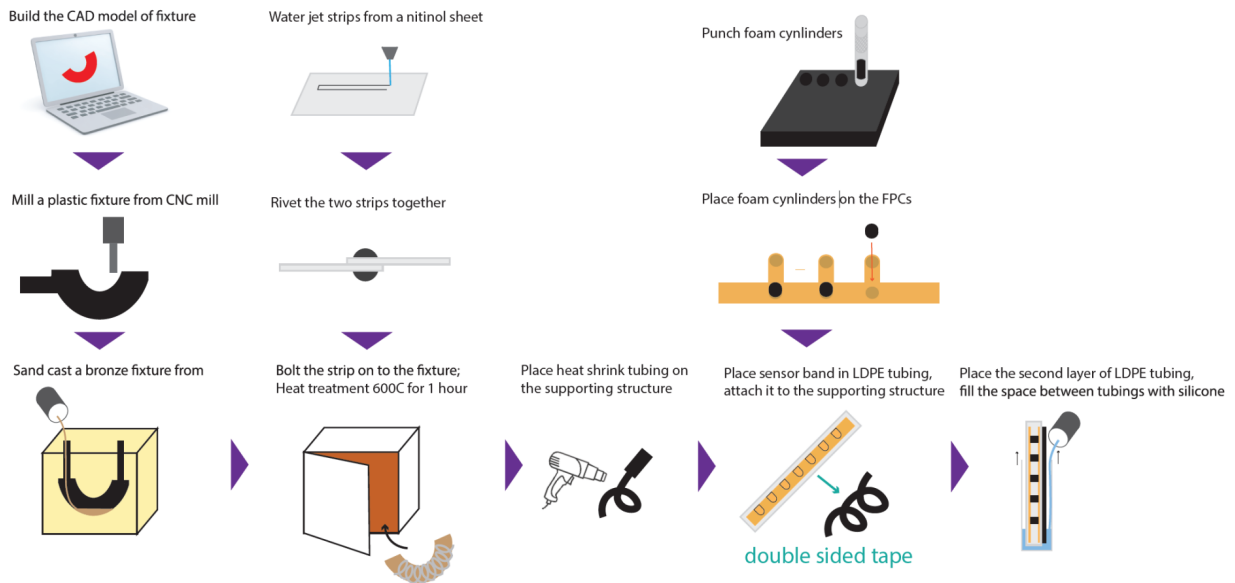


Fig. 15 Bolus supporting structure fabrication and integration of sensors/supporting structure workflow. Note in the tubular probe, the supporting structure was cut from a Nitinol sheet using a water jet bed and then directly integrated with the sensors.

After successfully designing the sensing probe, I also developed an electronic interface capable of reading the data output and conducted *in vivo* evaluations of the system.

Chapter 3. Universal motility mapping system and its *in vivo* validation

3.1 Scanning board design, fabrication, and scanning workflow

The printed circuit board (PCB) of the pressure mapping system and its power supply was mounted on a 10 in x 10 in acrylic board (Fig. 16). The PCB consists of a motherboard, which hosts the microcontroller, amplifiers and multiplexers, and interchangeable daughterboards bearing reference resistors and transimpedance feedback resistors (Appendix A). The governing principle of resistance measurement through a transimpedance amplifier is illustrated in Fig. S3 m. The output voltage of the transimpedance amplifier is described by Eqn.33. To measure the resistance of all sensing elements in the array, I used “zero potential scanning” [186]. As shown in Fig. S3 o, a voltage buffer is connected to each row, and a transimpedance amplifier is connected to each column. By controlling the multiplexer, a known driving voltage is applied to one row of connections while leaving the other row of connections at the ground potential. The transimpedance amplifiers on each column ensure that all columns are also at ground potential. Thus, the sensing elements on the row to which the driving voltage is applied have current through them, while the sensing elements on the other rows are at ground potential. This method ensures that the resistance calculated from the driving voltage and resulting current is not affected by the bypass current flowing through the sensing elements on the non-driven rows, known as “cross-talk”.

$$V_{out} = -\frac{R_{feedback}}{R_{foam}} V_{drive} \quad Eqn. 33$$

The data-path of the pressure mapping system is shown in Fig. S3 n. Pressure sensing foam and reference resistors are electrically arranged in an array with row and column connections. A driving voltage is applied to each row sequentially, and the resulting current is converted to a measurable voltage by a bank of transimpedance amplifiers, then sampled and sent to a host system via USB Serial connection.

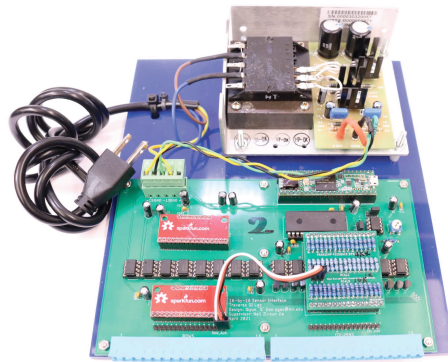


Fig. 16 An image of the 224 channels resistance scanning board.

A simplified circuit layout is shown in Fig. 17. The microcontroller (Teensy 3.6, DigiKey P/N 1568-1442-ND) generates a driving voltage through its digital to analog converter (DAC) and selects one row to apply the driving voltage through the row scanning multiplexer (MX1) (DigiKey P/N 1568-1181-ND) while leaving other rows at ground potential (referred to as ‘selecting’ a row). The driving voltage or ground potential is then applied to each row by a bank of voltage buffers (RA0-15) (DigiKey P/N 296-9554-5-ND). Since column connections are connected to the negative port of transimpedance amplifiers (CA0-15) (DigiKey P/N 296-9554-5-ND), columns are kept at ground potential. Therefore, current only flows through sensing elements on the row with driving voltage applied. Other sensing elements have no current through them since they have ground potential on both sides. The current on each column is converted to voltage by transimpedance amplifiers according to Eqn. 33. As the current on each column is only through one sensing element, resistance or conductance of each sensing element can be measured individually without cross-talk.

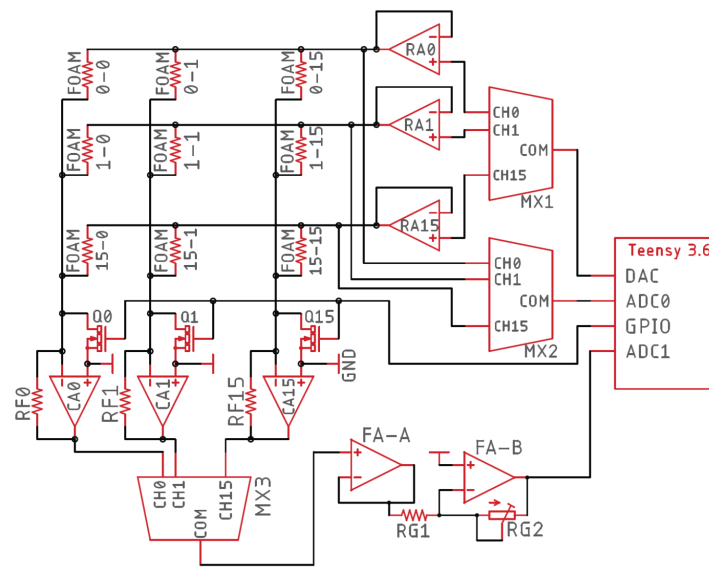


Fig. 17 The electronic wiring diagram.

The output voltage of the transimpedance amplifier on each column is then fed into the column selection multiplexer (MX3) (DigiKey P/N ADG506AKNZ-ND) that screens through all columns while one row is selected. The output of the column selection multiplexer is buffered by amplifier FA-A (DigiKey P/N 2156-NE5532P-ND) and then flipped to a positive voltage with an appropriate gain by inverting amplifier FA-B (DigiKey P/N 2156-NE5532P-ND), and finally sampled by an analog to digital converter (ADC). In the meantime, the row monitoring multiplexer (MX2) (DigiKey P/N 1568-1181-ND) connects the selected row to another ADC in order to accurately measure the voltage on the selected row. Therefore, with voltage

across and current through the sensing element, its resistance can be accurately measured. The system flowchart can be seen from Fig. 18.

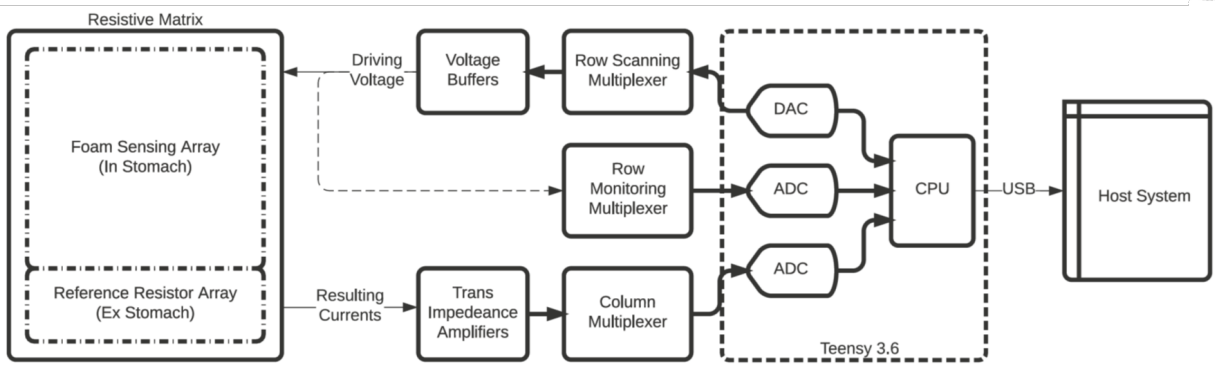


Fig. 18 A diagram of the column-rows scanning structure.

Furthermore, as the capacitance of the sensing element is non-trivial, the system needs a current input large enough to pull row connections to the driving voltage or back to ground potential. Row currents are directly provided by voltage buffers, but column current is limited by feedback resistors. To alleviate this, bypass transistors (Q1-Q15) (DigiKey P/N 2N7000BU-ND) are connected from column connections directly to ground in order to provide a low-resistance path to quickly charge and discharge the capacitance of sensing elements, thereby increasing the row switching speed and the frame rate of the system. The automated protocol of measuring the resistance of the whole sensing matrix is as follows.

1. Turn on Q0-Q15
2. Set MX1 to the apply driving voltage to the desired row
3. Set MX2 to the row driving voltage being applied
4. Turn off Q0-Q15
5. Cycle MX3 through channel 0-15 and sample its output voltage
6. Repeat Step 1-5 until all rows are measured

3.2 Self-calibration and testing protocols of the scanning board

As shown in Fig. 17, output voltage of each column is fed into the column multiplexer, followed by a buffer and an inverting amplifier with a gain of K . Therefore, voltage fed into ADC can be expressed as Eqn. 34, or simplified to Eqn. 35, in which K is a known constant. If driving voltage, feedback resistance, and gain of the inverting amplifier are held as constants, then c , the zero-point drift of op-amp, is also a constant. However, the feedback resistance and gains are subject to manufacturing tolerance and thermal drift, so two reference rows consisting of precision reference resistors are included in order to calibrate with two known resistances, R_1 and R_2 , on each column. In this design, R_1 and R_2 are 1.00 kOhm (DigiKey P/N

RNCF1206TKY1K00CT-ND) and 10.00 kOhm (DigiKey P/N 10KADCT-ND) respectively. The reference resistors are sharing column connections with the array of sensing elements. In this implementation, R_1 and R_2 are optimized to have conductance G_1 , which produces a near full-scale ADC reading, and G_2 , which is the lower-bound of the resistance measured. Therefore, the variation in K between columns can be compensated since reference resistors are subject to the same K as the foam resistances being measured.

In a measurement sequence, suppose V_1 and V_2 are the measured ADC readings when the rows consisting of R_1 and R_2 are not grounded. The V_{foam} 's, which are the ADC readings when the rows consisting of foam sensing elements are active, are also measured sequentially. In each column, the sensed voltages of each resistor are subject to the same K (Eqn. 34-38). Since G_1 and G_2 are known at this step, G_{foam} can be calculated without knowing K . This scanning structure makes the measured results less sensitive to variations in the feedback resistors, thermal drift, and fluctuations in the amplifiers. The factor of k lumps all the parameters together in the measurement. And taking the advantage of the self-calibration, I am able to eliminate the k in the equations and obtain Eqn. 39 from Eqn. 35-38.

$$V_{ADC} = G_{foam} V_{drive} R_{feedback} K + const \quad \text{Eqn. 34}$$

$$V_{ADC} = G_{foam} k + const \quad \text{Eqn. 35}$$

$$V_1 = G_1 k + const \quad \text{Eqn. 36}$$

$$V_2 = G_2 k + const \quad \text{Eqn. 37}$$

$$V_{foam} = G_{foam} k + const \quad \text{Eqn. 38}$$

$$G_{foam} = (G_1 - G_2) \frac{V_{foam} - V_2}{V_1 - V_2} + G_2 \quad \text{Eqn. 39}$$

The pressure mapping system is tested by a variable resistor array and a physical test pattern on sensing elements. The circuit diagram of the variable resistor array is shown in Appendix A f, in which JP1 makes 5 row connections and JP2-3 makes 8 column connections. Appendix A g-h show the physical variable resistor array consisting of 40 trimmer potentiometers (Amazon P/N B07J4NR372). The results are shown in Appendix A i-l. The variable resistor array is connected to row 0-4, column 0-7 for Appendix A i-j, and to row 9-13, column 8-15 for Appendix A k-l. Appendix A i and k show the voltages measured by ADC; Appendix A j and l show the measured resistance. The variable resistor array's value is set into a checkerboard pattern with a range of resistances to reveal any cross-talks and signal degradations. The resistances were also measured by handheld multimeter (Innova 3220). The resistance measured by the pressure mapping system coincides with multimeter reading for 3 significant figures, indicating an error less than 1%.

The performance of the system was evaluated by a variable-resistor array and by a physical test pattern pressed against the sensing elements (Appendix A g-l). Appendix A m was used to calculate the value of the sensing element resistance from the voltage readings. A long belt of sensors was placed into a serpent-like shape under a set pattern to fit into the testing platform (Appendix A n). As seen in Appendix A o, the test pattern consisted of 4 presser plates that form the letters “MIT” when stacked. The width of each protrusion is 20mm, matching the spacing of sensing elements, and the thickness of the plate is ¼ inch (6.35 mm). A belt-shaped sensor with sensing elements arranged linearly is used in this test. The physical test pattern is shown in Appendix A n-p with protrusions forming the letters ‘MIT’ when stacked. The plates are held on an Instron and pressed into the belt-shaped sensing matrix with the protrusions aligned with sensing elements. The pattern is driven into the sensor with a force of 5 N. Such a test pattern causes alternating high-pressure and low-pressure points on the sensor array, demonstrating the MIT letters clearly while also showing the absence of cross-talk between sensing elements as observed in both evaluations (Appendix A p). This result shows the system can map complex pressure pattern thus paves way for further testing.

3.3 Bench-top tests of esophagus, rectum and stomach probe

The setup of the bench-top calibration of esophagus and rectum probe is shown in Fig. 19 a. The linear sensing probe and a probe of HRM were sandwiched between a pneumatic bladder and a wood board covered with foam. The pneumatic bladder was then inflated/deflated. Data obtained from the sensor band and HRM probe are synchronized and plotted into Fig. 19 c. The x-axis is the recorded conductance from each unit in the sensor band, and the y-axis is the pressure reading from the HRM probe. Except sensor units 1 and 2, the conductance and the pressure readings have a clear linear correlation. This data is then used as calibration for future studies. To further test the time resolution of the tubular sensing probe, I taped it to the bench along with the probe of HRM. A rolling rod was then rolled over the probe and sensor band at the same time, shown in Fig. 19 b. The data obtained from the rolling test is plotted into Fig. 19 d and e. X-axis is the time, y-axis is the location of sensing units on the sensor band/probe, and the color shows the value of pressure. The rolling test data from sensor band and probe show great similarity.

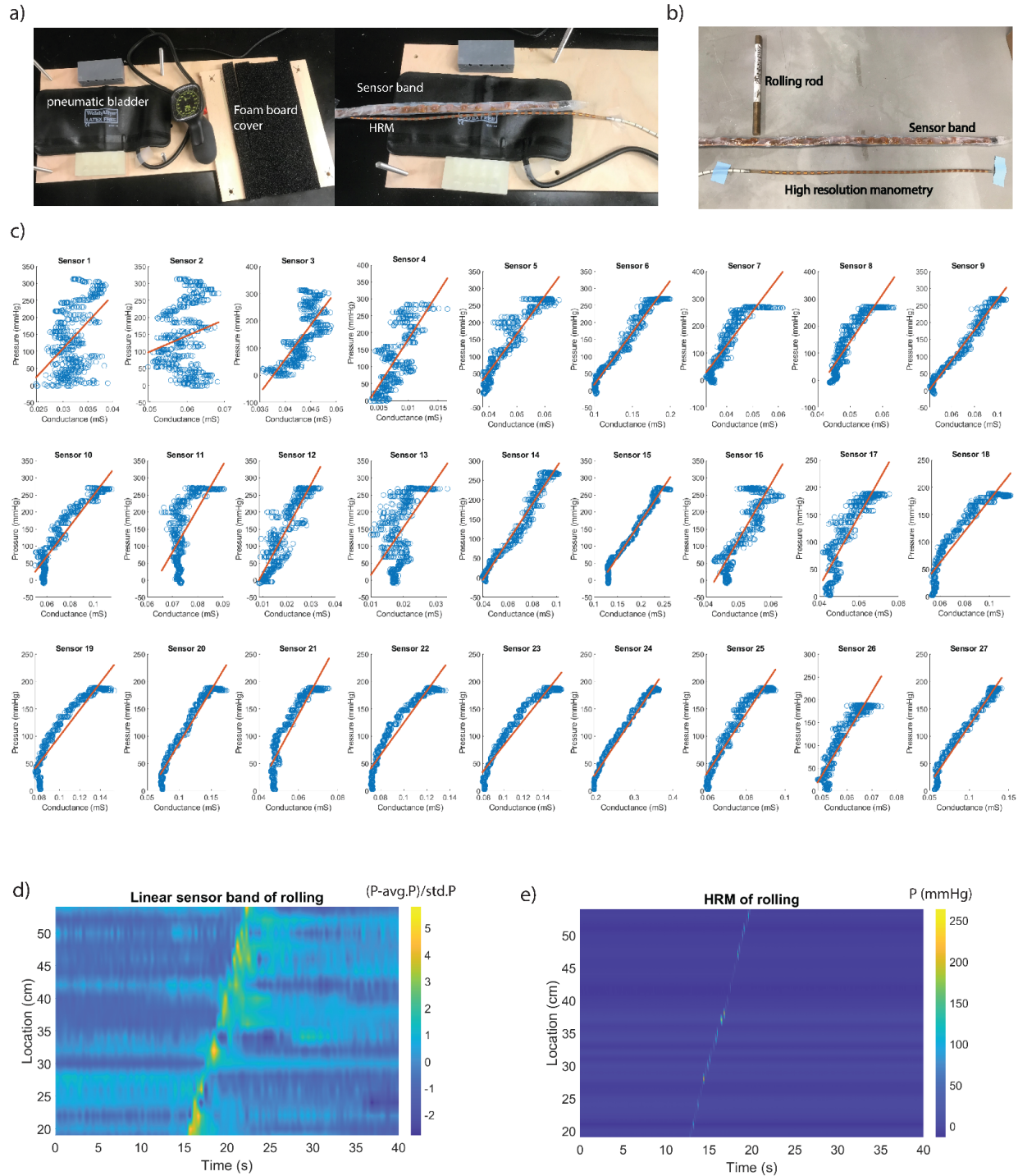


Fig. 19 a) Tubular sensor probe calibration setup. b) A picture of sensor probe and HRM be placed side to side. c) Tubular sensor band calibration data curves. Time vs location vs pressure recording of the pin rolling event. The data were recorded from d) tubular sensor probe, e) HRM.

The bolus sensing probe's ability on spatial-temporal pressure mapping was validated. The sensor belt was first immersed in a water bath heated to 40 degrees Celsius to turn the sensing probe into the programmed shape. Sensor numbers 28, 50 and 73, indicated by arrows in Fig. 20 c in left-to-right order, were tested.

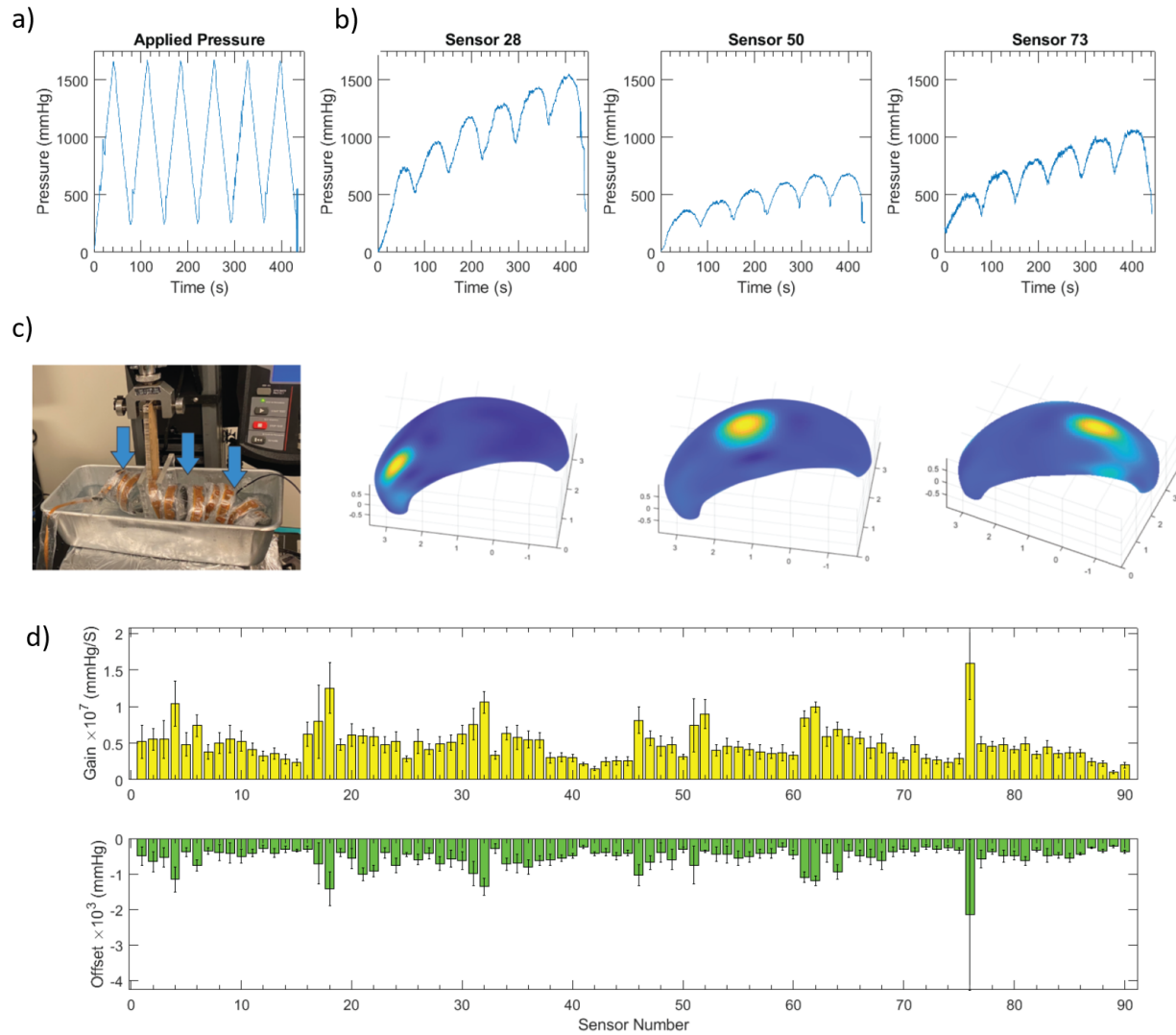


Fig. 20 a) The applied pressure curve of the Instron loading/unloading. b) The pressure response curves of the three points being pressed. c) Bench-top test of the integrated system, Instron's compressor pressed at three different locations with arrows pointing to the locations being pressed. The computer interface shows which location on the sensor system has been pressed corresponding to the three arrows in the photo. d) Calibration data of the all 90 sensor units, gains and offsets for the conductance-pressure correlation.

The sensing probe was mounted on a structure that provided support. Each sensor was subject to a pressure cycle shown in Fig. 20 a. The output of each sensor is shown in Fig. 20 b. Localization and pressure response validation is performed as shown in Fig. 20 c. The individual sensor cells were calibrated in groups to compensate for variation among pieces. Sensor calibration was performed on an Instron platform. A flat pressure plate fixed on the Instron grasp jogged down onto the sensor belt mounted flat on a ¼ inch aluminum plate. The pressure plate was large enough to cover 6 sensor units. For each run, a ramping force with a peak amplitude of 5 N was evenly distributed among the 6 sensors being calibrated. The applied

force ramp consisted of 6 cycles, and the duration of each calibration was 300 seconds. The force applied to and resultant conductance of each sensor were linearly fitted using *cftools* in the MATLAB environment. I subtracted the ‘gains’ (slopes of the fitted lines, representing the sensitivity of the sensor) and ‘offsets’ for each sensor. The gain and offset of each sensor are shown in Fig. 20 d with error bars representing the 95% confidence interval.

3.4 *In vivo* evaluation protocols on a swine model

To validate the proposed concept, three Yorkshire swine, each weighing 75-100 kg, were used to test the platform. During the experiments, all three probes were deployed into the swine, and an electronic connection cable transmitted signals from the individual sensor units to the scanning interface. Data was then streamed to a PC. An electronic interface is developed to record the data streamed from *in vivo* probes.

A clinical HRM was used as the tool of calibration and comparison. The swine were anesthetized before the experiment and several stimulation methods were used to generate motility/reflex. The *in vivo* data collected in this study is processed in MATLAB using moving average filter to remove the noise came from heart beating in the animals. During *in vivo* experiments, I first deployed the sensing probes and HRM probes into the animals. I turned on the devices and observed the live-streamed baseline readings of HRM and sensing probes for 1-2 minutes. After confirming there were no motility/peristalsis/reflex patterns observed on both devices I then subsequently started applying stimulations to the animals.

Animal Sedation:

Pigs were sedated with intramuscular injection of Midazolam 0.25mg/kg with Dexdomitor 0.03mg/kg and after intubation, anesthesia was maintained with isoflurane (1-3% in oxygen).

Recovery:

Pigs are returned to their pen and sedation reversed intramuscularly with the reversal agent Atipamazole. If intubated, the pig is closely monitored until extubation and then is followed by monitoring of the recovery process until the pig is standing and considered bright, alert, and responsive (BAR).

Monitoring/Vitals throughout the study:

After the pig is sedated and weighted, it is placed on a heated operating table with the additional thermal support of a heated blanket Ophthalmic ointment is applied to both eyes. Once the pig is placed on isoflurane (1-2%) and oxygen (1-3%) either via a face mask or an endotracheal (ET) tube, it is then connected to an anesthesia monitoring machine in order to monitor vital signs every 15 minutes until returned to the pen.

Endoscopic Delivery:

Device delivered to stomach via colonoscope placed in orogastric tube/overtube. PENTAX EC-3870TLK (160 cm) for delivering drugs/devices to the stomach of larger pigs(>50 kg) and for retro flexing to visualize the entirety of the stomach.

Overtube specifications:

Material: Urethane PVC; Inner diameter: 5/8 inches; Outer diameter: 3/4 inches; Wall thickness: 1/16 inches.

3.5 In vivo evaluation of the motility mapping probes

A. Esophagus

To verify the accuracy of our device, I conducted comparison studies in the esophagus. First, I tested the effect of a bolus balloon on esophageal peristalsis. I inserted a deflated bolus balloon into the esophagus along with our sensor probe and the HRM sensor catheter together. The tips of the two sensor probes were 20-30cm behind the balloon. I inflated the balloon with 10mL water and moved it up and down the esophagus. This movement created a swallow reflex, and I recorded the data on both machines before repeating this process twice more with a five-minute break in between. Once I finished with the bolus balloon, I ran tests with a dilation catheter. I inserted the sensor band, HRM sensor, and dilation catheter together roughly 20-30cm into the esophagus. Using a syringe, I changed the volume of the dilation catheter by increasing it to 10mL then decreasing it back to 0mL. Each of these cycles took 30-60 seconds. Like the bolus balloon, I conducted three cycles with a five-minute wait between each cycle.

Through endoluminal stimulation from either a balloon or dilation catheter, I observed the patterns of a single strong contraction followed by series of weaker contractions in the esophagus. To evaluate the performance of the esophageal probe I applied a model food bolus (endoscopic placement of a balloon) and quantitatively compared the pressure readings (Fig. 21 a). The peristalsis peaks were captured by both the esophagus sensing probe and a commercial HRM which served as a comparator, with correlation factors of 0.581, 0.486, and 0.487 at 18, 20, 22cm from the incisors and p-values of the Wilcoxon rank sum test of $4 \cdot 10^{-17}$, $5 \cdot 10^{-8}$, and $2 \cdot 10^{-8}$, respectively. The spectral intensity graph of the two sensing readings is shown in Fig. 22 a. The correlation between the two spectra is 0.6645. The pressure-time-location graphs from 10 to 36 cm are shown in Fig. 23 a and b. A clear similarity can be seen in the two graphs, in which three strong pulses are observed at $t = 0, 35,$ and 90 s with subsequent periodic contractions. I then used a dilation catheter to stimulate a single pulse of contraction in the esophagus. Fig. 21 b shows the strong single pulse captured by both devices, with correlation factors of 0.5578, 0.5597, and 0.6120 at 18, 20, 22cm from the

incisors, respectively, and p-values of the Wilcoxon rank sum test of $5 \cdot 10^{-6}$, $1 \cdot 10^{-5}$, and $2 \cdot 10^{-6}$, respectively. The spectral intensity graph of the two devices is shown as Fig. 22 b, with a correlation factor 0.6202 for the two signals. The pressure-time-location graphs of the dilation catheter case are shown in Fig. 23 c and d. A single strong pulse was recorded in both devices, followed by the subsequent smaller pulses.

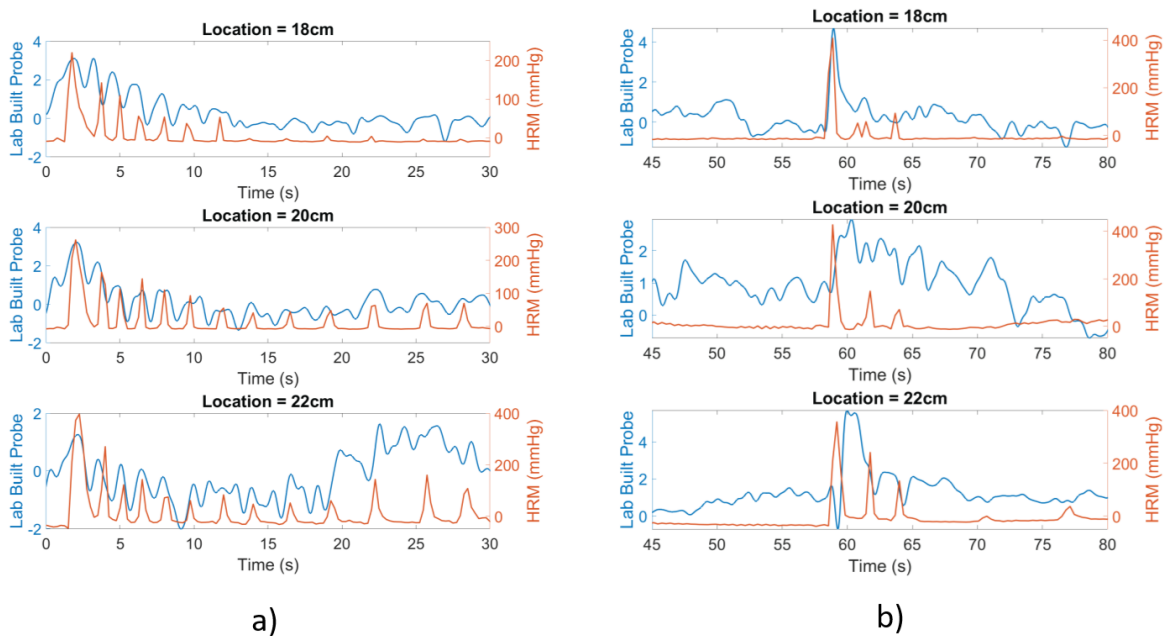


Fig. 21 Pressure-time-location plots at three different locations from a) esophagus stimulated by a bolus balloon, b) esophagus stimulated by a dilation catheter.

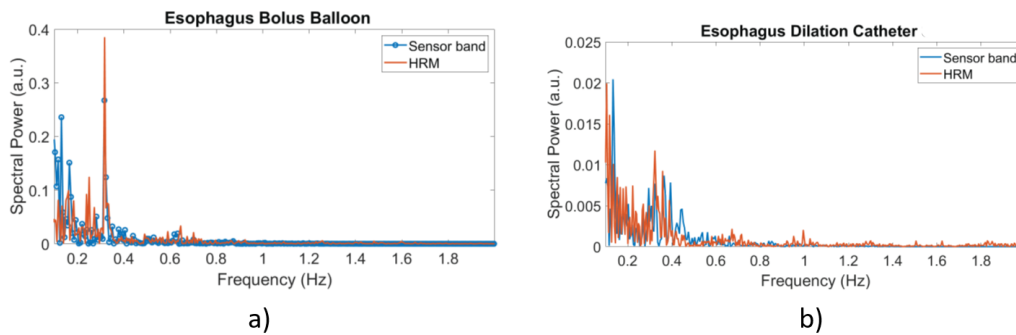


Fig. 22 a) Spectral power of motility signals in the esophagus where a dilation catheter is used to stimulate. b) Spectral power of motility signals in the esophagus where a bolus balloon is used to stimulate.

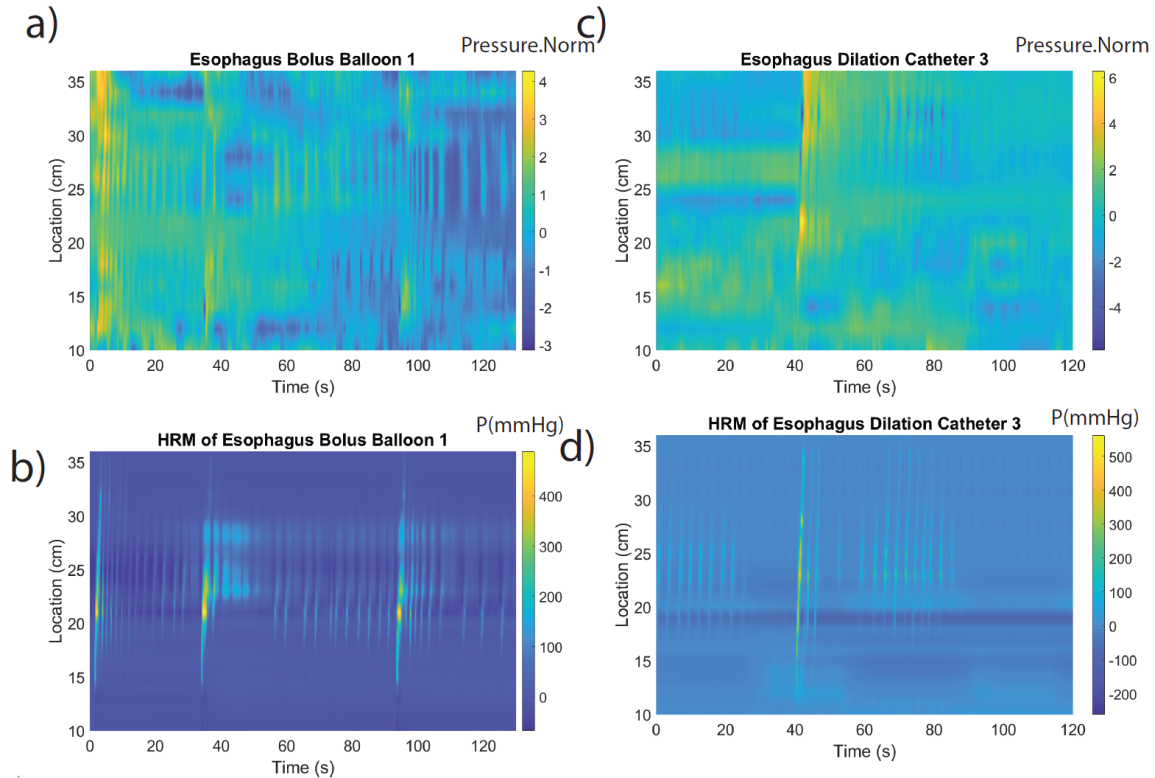


Fig. 23 Motility mapping graphs obtained from a) tubular organ sensor band b) HRM in the esophagus of a swine model. A bolus balloon is used to stimulate the esophagus. Motility mapping graphs obtained from c) esophagus probe created by the authors d) HRM in the esophagus of a swine model.

B. Rectum

I inserted a bolus balloon into the rectum along with the HRM probe and our sensor probe. The two probes were inserted 10cm into the rectum. I started collecting data and recorded one minute of a baseline on both devices. At 80s, I inserted the bolus balloon into the rectum. Then I inflated the balloon with 20 mL water at 140s and held it for two minutes. I deflated the balloon and held it for two minutes. I repeat this process two more times.

I evaluated an endogenous reflex in the rectum called the rectoanal inhibitory reflex which involves relaxation of the internal anal sphincter in response to rectal distention to facilitate the passage of stool [187]. I placed a balloon into the rectum of the swine along with the sensing probe and the HRM catheter. I inserted the balloon at 80s (see Fig. 24 a, annus panel) and thus at the anus there was a significant increase of pressure at around that time. This insertion was also captured by the sensing probe at location = 4cm shown in the blue line. At 140s, I inflated the balloon to simulate rectal stool filling. The filling was accompanied with a decrease in pressure at the level of the anal canal (see Fig. 24 a, annus panel 140s). The data from the rectum pressure mapping are presented in pressure-time-location graphs in Fig. 24 b and

c. The inflation event, which corresponds with an increase of pressure, occurs at 140s at 4 and 6 cm; the relaxation event in the anus at 0 cm occurs around the same time point.

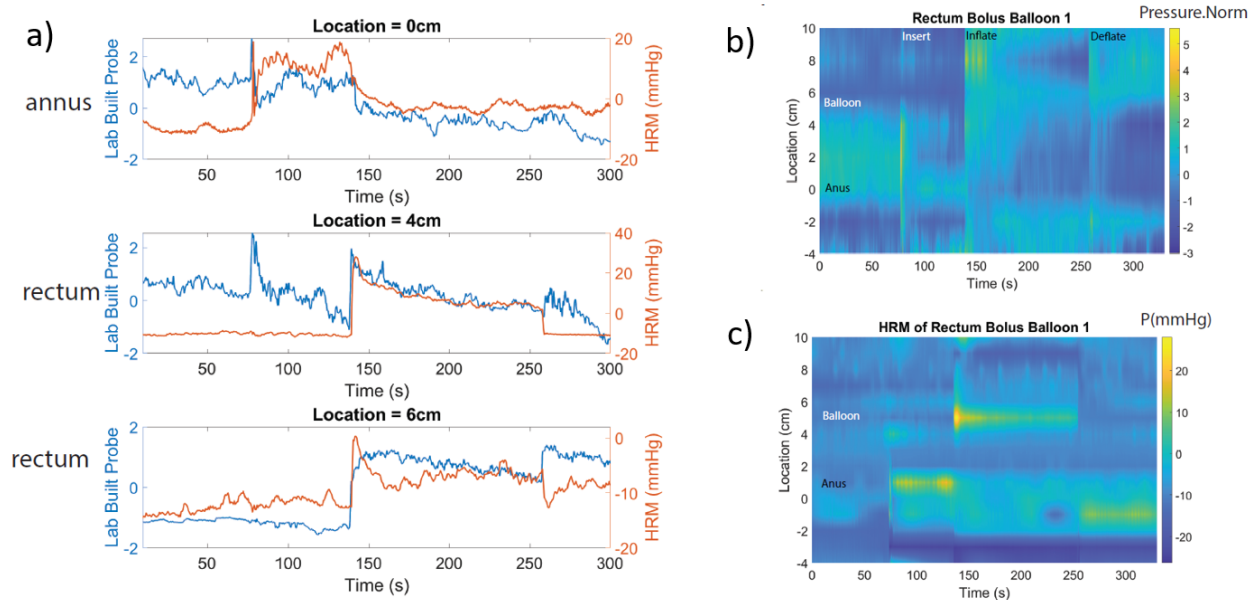


Fig. 24 a) Pressure-time-location plots at three different locations from rectum stimulated by a bolus balloon. Reflex recording graphs obtained from b) rectum probe created in this work c) HRM in the rectum of a swine model. A bolus balloon is used to stimulate the rectum.

C. Stomach

The coil conformal arrangement was evaluated *in vivo* in the stomach of swine. Testing was performed through external abdominal palpation. For internal force, I secured a hose clamp on the end of the overtube so that the stomach was a closed system. Using the endoscope, I then inflated the stomach for 30 seconds then deflated the stomach for 30 seconds. External force was applied by applying palpation on the abdomen. On the abdomen was a pressure sensor, whose calibration is depicted in Fig. 20 d. I obtained this calibration graph with an Instron measuring force and multimeter measuring resistance simultaneously. Tests for external force were conducted for 10 minutes in cycles, where each cycle consisted of five seconds of application and ten seconds of rest. A force sensor was placed under the hand to record the pressure applied by the hand. Sensing unit 24 on the probe was selected for comparison with the external pressure and concordant pressure changes were observed. The pressure distribution of the device as a function of time is shown as well. As can be seen, external compression causes a pressure increase in two areas: on the distal lesser curvature, and on the proximal greater curvature (Fig. 25 a). I also evaluated the effect of repeated gastric insufflation with a period of around 30s (Fig. 25 b): each peak in the graph relates to a deflation

event. During the deflation events, I had the capacity to observe discrete changes throughout the gastric walls.

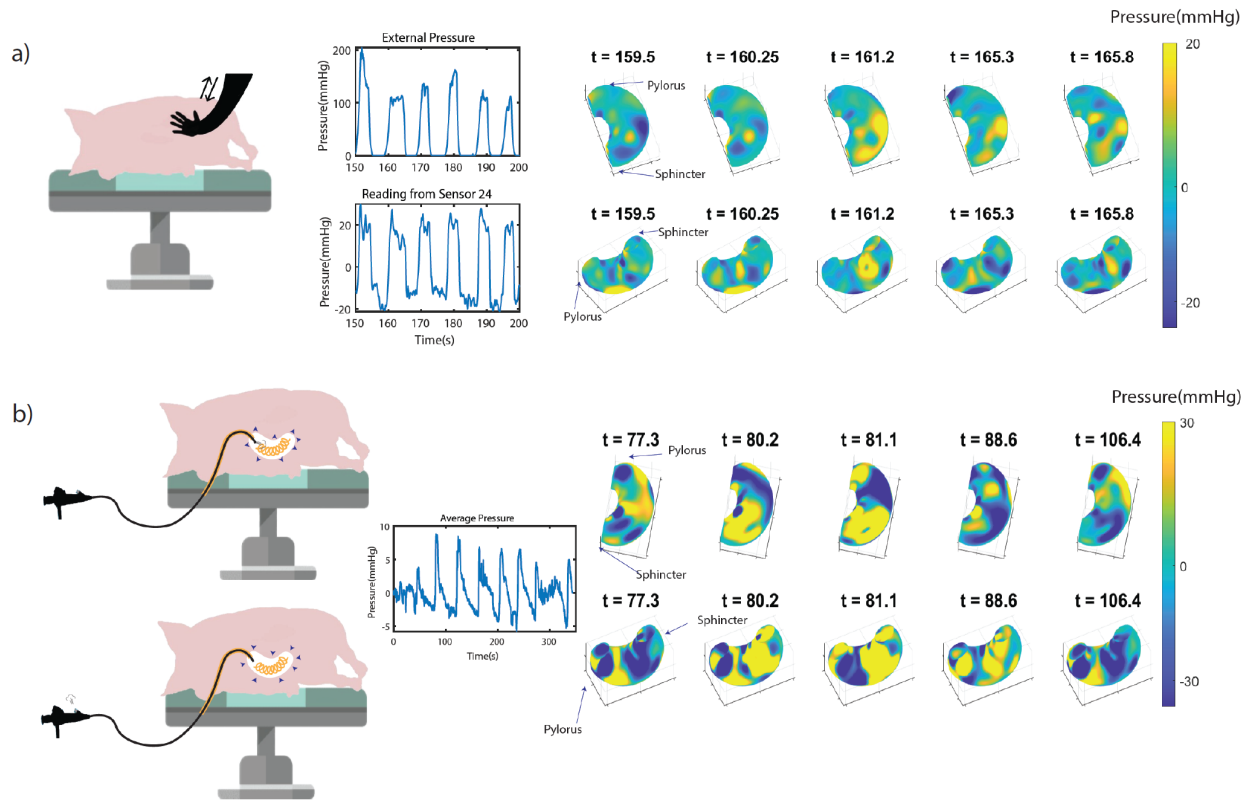


Fig. 25 a) Application of external force on the abdomen of the swine via palpation. External pressure and reading from sensor 24 are plotted into two separated line plots. The mapping results at different time points are shown by contour graphs on the right. b) Applications of internal force by inflating and deflating the stomach with an endoscope. The average pressure from all sensors is plotted into a line graph. The mapping results at different time points are shown by contour graphs on the right.

Chapter 4. Motorized expansion head dynamic satiety stimulator and its *in vivo* validation

4.1 *Dynamic satiety stimulation*

To address the need for an effective weight loss treatment with both high efficacy and minimal invasiveness, I considered the intragastric balloon, a temporary balloon placed within the stomach. This procedure is minimally invasive, but its efficacy has been limited. A study on a swine model found that satiety induction was only effective in the first week after balloon placement [188]. Over the course of the first week, food intake was reduced by 50%. However, in the following weeks, food intake increased at the same rate as the control group. A similar trend was also observed in human trials of intragastric balloons, where the effect of inducing feelings of fullness decreased over time. [189].

This observation led us to hypothesize that the cause of the loss of efficacy was due to the accommodation of the balloon in the stomach, which resulted in a loss of stimuli. Satiety factors are released by the GI tract and enter the bloodstream or stimulate the vagus nerve to send satiety signals to the brain [190]. The gastric muscles relax, and the gastric cavity expands in response to ingested food, a process known as gastric accommodation. With a static placement of the balloon, the stomach is forced to accommodate the balloon's volume, resulting in the loss of stimuli. To increase the occupational satiety induction efficacy, I and Dr. Traverso propose simulating natural feeding behavior and satiety signal induction. The intragastric stimulator can be delivered via the esophagus and expand before meals and shrink back to a minimal volume after meals. I developed two stimulators using motorized and balloon technology and have validated their functionality through testing on a swine model.

4.2 *Structural analysis of the skeleton motorized expansion head*

The motorized expansion stimulator developed in this work is a capsule that can be delivered endoscopically to the stomach and subsequently expand during the meal (Fig. 26 a, the expandable cover is not shown). The mechanical model of the skeleton device and the sliding connector are shown in Fig. 26 b and c. The slider with a threaded inner bore (labeled as point A) is hinged with four inner arms (labeled as AB). A leadscrew is connected to a motor that spins and applies actuation force (F_a) on slider, causing the four outer arms (labeled as CD) to expand with the displacement of the slider.

In the first part of the design, it was important to minimize the actuation force F_a to reduce power consumption. Actuation force F_a works against force F , which is applied on each arm by the surrounding tissue, to expand the stomach. The expansion of the device results in an increased volume of the stomach

and a stretched protection cover. F_a is a function of force applied on the arm and its geometry. I assumed that the force F was applied perpendicular to the center axis of the expansion head, which applies force on the stomach wall to expand the volume. In a skeleton device, the amount of force needed is dependent on the total force required to expand the volume (F_{vol}) and the number of arms (N_{arm}), which is four in this design. This relationship is described as:

$$F = \frac{F_{vol}}{N_{Arm}} \quad \text{Eqn. 40}$$

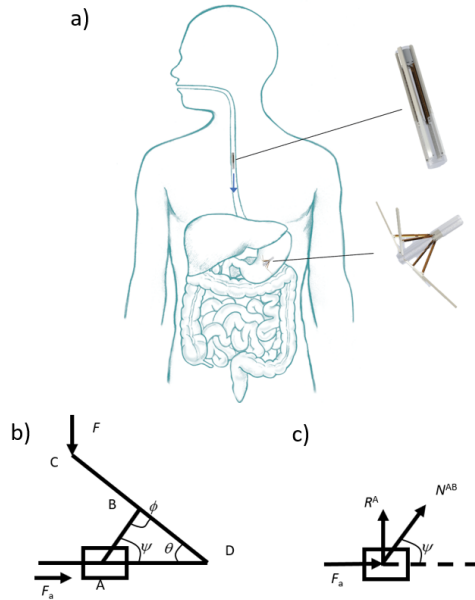


Fig. 26 a) Illustration of the endoscopic placement and intragastric expansion of the motorized expansion head. Free body diagram of the b) motorized skeleton and c) the slider.

To determine the volume force required to expand the stomach, I used clinical data from [147] where a balloon was inflated inside the stomach. The energy delivered by expanding the radius of the gastric cavity by dr is equal to the energy required to expand the volume of the balloon (PdV). The volume of the gastric balloon is proportional to the square of the radius r , the length of the balloon which is lumped into a factor of α that can be obtained from the maximum volume, and diameter of the balloon placed inside the stomach ($V = \alpha r^2$). Therefore, the volume force needed to expand the stomach can be calculated as:

$$F_{vol} = P \frac{dV}{dr} = 2P\alpha r \quad \text{Eqn. 41}$$

From the free body diagram of the slider (Fig. 1c), the actuation force (F_a) can be seen to be equal to the projection of the compression force N^{AB} to the axis of the device. For a given θ , angle ψ can be derived using Eqn. 42.

$$\psi = \sin^{-1}\left(\frac{l_{BD} \sin \theta}{l_{AB}}\right) \quad \text{Eqn. 42}$$

Angle $\phi = \pi - \theta - \psi$. In this design, I set $l_{AB} + l_{BD} = l_{CD}$, thus at the folded state $l_{AD} = l_{CD}$. With actuation force F_a pushes the slider and expands the system, the distance slider travels is defined as stroke length $s = l_{CD} - l_{AD}$:

$$s = l_{CD} - l_{AB} \sin(\phi) / \sin(\theta) \quad \text{Eqn. 43}$$

According to the virtual work principle, the actuation force F_a and F_{total} are related as shown in Eqn. 5:

$$F_a ds = F_{vol} \cos(\theta) l_{CD} d\theta \quad \text{Eqn. 44}$$

Utilizing the equations I have so far:

$$\frac{d\theta}{ds} = \frac{1/l_{BD} + (l_{AB}^2 - (l_{CD} - s)^2 - l_{BD}^2) / (2 * l_{BD} * (s - l_{CD})^2)}{(1 - \cos(\theta))^2)^{0.5}} \quad \text{Eqn. 45}$$

Using Eqns. 41, 44 and 45, I have the actuation force with different inner arm l_{AB} lengths at $l_{CD} = 5\text{cm}$. As shown in Fig. 27, the peak actuation force with $l_{AB} = 1, 1.5, 2\text{cm}$ is 63, 60, 104 N respectively. In this work, l_{AB} is set as 1.5cm to minimize the load on the motor.

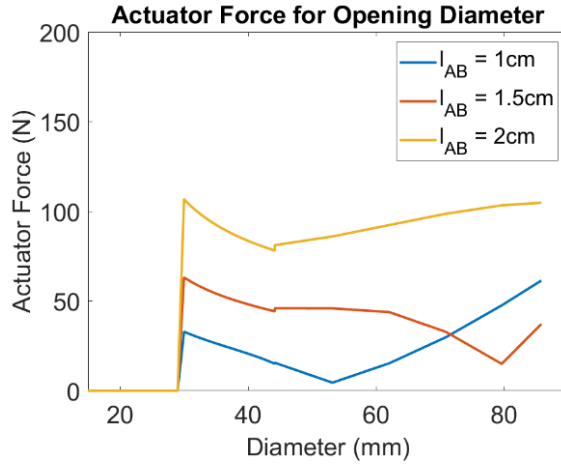


Fig. 27 Actuation force F_a as a function of open diameter with different inner arm lengths without a cover.

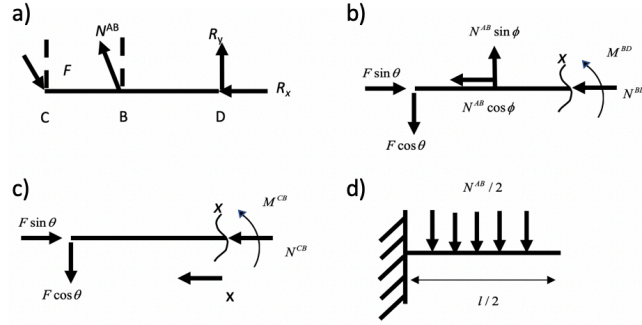


Fig. 28 The free body diagram of the a) outer beam, b) right part of the outer beam, c) left part of the outer beam, d) half of the pin at hinge point B.

After calculating the F_a , I aimed to determine the maximum stresses within the structure. I considered the following stresses: inner arm AB compression stress and buckling load, outer arm CD maximum bending stress, pin bending stress at hinge connection B, and leadscrew buckling load. The free body diagrams are shown in Fig. 28 a-d.

The outer arm CD is modeled as a beam pivoted at D (Fig. 28 a), and parts BD and CB of the outer arm are considered separately. The torque and compression force at the cross-section is a function of x , the distance from the cross-section to the pivoted point D or B (Fig. 28 b and c). Via the balance of force along the axis of actuation as shown in Fig. 26 c, the compression force in the inner arm AB is:

$$N^{AB} = \frac{F_a}{\cos(\psi) N_{Arm}} \quad \text{Eqn. 46}$$

The compression stress in the arm AB is:

$$\sigma_{compression}^{AB} = \frac{N_{max}^{AB}}{A_{AB}} \quad \text{Eqn. 47}$$

The inner arm was modeled as a 1.5mm by 1.5mm square column with both ends pivoted. The buckling load was calculated from Euler's critical load equation [191]:

$$F_{critical} = \frac{\pi^2 EI_{AB}}{l_{AB}^2} \quad \text{Eqn. 48}$$

Where E is the Young's Modulus of the material and I_{AB} is the cross-section moment of inertia whose value depends on width a and height d of the inner arm:

$$I_{AB} = \frac{ad^3}{12} \quad \text{Eqn. 49}$$

The critical compression stress considering the buckling is $F_{critical}/ad$. Similarly, the steel leadscrew was also considered for its buckling load:

$$F_{leadscrew} = \frac{4\pi^2 EI_{leadscrew}}{l_{leadscrew}^2} \quad Eqn. 50$$

Where $I_{leadscrew}$ is the moment of inertia of the cross-section, the axial force balance is:

$$N^{BD} = N^{AB} \cos(\phi) - F \sin(\theta) \quad Eqn. 51$$

The bending torque derived from free body diagram is:

$$M^{BD} = (l_{BD} - x)N^{AB} \sin(\phi) - (l_{CD} - x)F \cos(\theta) \quad Eqn. 52$$

For CB in the outer arm, the axial force balance gives the compression force:

$$N^{CB} = F \sin(\theta) \quad Eqn. 53$$

$$M^{CB} = (l_{CD} - x)F \cos(\theta) \quad Eqn. 54$$

The maximum bending stress can be derived from the following equation:

$$\sigma_{bending}^{CD} = \frac{hM_{max}^{CD}}{2I_{CD}} \quad Eqn. 55$$

Where I_{CD} is the moment of the inertia of the arm CD, whose value depends on height h and width b of the arm:

$$I_{CD} = \frac{bh^3}{12} \quad Eqn. 56$$

The compression stress in the arm CD is:

$$\sigma_{compression}^{CD} = \frac{N_{max}^{CD}}{bh} \quad Eqn. 57$$

In the calculation, I define the maximum stress in arm CD as:

$$\sigma^{CD} = \sigma_{compression}^{CD} + \sigma_{bending}^{CD} \quad Eqn. 58$$

I also determined the maximum stress in the connection pins at joints A and B. I modeled half of the pin, which has a length of $2l$, as a cantilever beam under a uniform load of $N^{AB}/2l$ (as shown in Fig. 28 d) for symmetry purposes. The torque in the pin can be obtained by:

$$M_{pin} = -\frac{(l-x)^2 N^{AB}}{2l} \quad Eqn. 59$$

The maximum bending stress in the pin can be expressed as:

$$\sigma_{pin} = \frac{r_{pin} M_{pin}^{max}}{I_{pin}} \quad \text{Eqn. 60}$$

Where r_{pin} is the radius of the pin, and the moment of inertia of the pin I_{pin} is:

$$I_{pin} = \frac{\pi r_{pin}^4}{4} \quad \text{Eqn. 61}$$

Table 5 The value of stresses in the skeleton motorized expansion head.

Parameters			
Maximum actuation force F_a (N)	60	60	60
Outer arm width b (mm)	4	4	4
Outer arm thickness h (mm)	2	2	3
Inner arm width a (mm)	2	2	2
Inner arm height d (mm)	1	1.5	1
Inner and outer arm material	Al 6061	Al 6061	Al 6061
Arms material yield strength (MPa)	240	240	240
Pin diameter at pivoted connection A r_{pin} (mm)	0.75	0.75	0.75
Pin material	Steel 304	Steel 304	Steel 304
Pin material yield strength (MPa)	250	250	250
Leadscrew length $l_{leadscrew}$ (mm)	30	30	30
Leadscrew diameter (mm)	3	2	2
Leadscrew material	Steel 304	Steel 304	Steel 304
Max inner compression stress $\sigma_{compression}^{AB}$ (MPa)	8.2	5.5	8.2
Max outer arm stress σ^{CD} (MPa)	58	58	26
Max pin stress σ_{pin} (MPa)	37	37	37
Critical stress of buckling for inner beam (MPa)	249	559	249
Critical load of buckling leadscrew (N)	17790	3514	3514
Arm strength requirement	Yes	Yes	Yes

Pin strength requirement	Yes	Yes	Yes
Leadscrew strength requirement	Yes	Yes	Yes

Through our analysis, I have determined the various stresses present in the system. These values have been calculated and listed in Table 5. The yield strength of steel 304 and Al 6061 is 205 and 276 MPa [192], [193]. To ensure the system's strength, the following conditions must be met:

1. The maximum compression strength in the inner arm must be less than the inner arm material's yield strength.
2. The maximum compression strength in the inner arm must be less than the inner arm's critical buckling stress.
3. The maximum stress in the outer arm must be less than the outer arm material's yield strength.
4. The maximum stress in the connection pins must be less than the pin material's yield strength.
5. The maximum actuation force must be less than the leadscrew's buckling load.

As seen in Table 5, any one of the three material/geometric parameter sets can provide sufficient strength.

4.3 Analysis of protection cover and covered motorized expansion head

In this study, the addition of an elastic latex cover onto the motorized skeleton is necessary to ensure protection against fouling and gastric contents. There are two main factors to consider when evaluating the cover's performance: maximum elongation and protection for the tissue. The design needs to ensure that the cover does not exceed its maximum elongation rate, which is between 300-650% for latex rubber [194]. When the covered device is surrounded by the tissue, tissue pushes into the cover with an indentation angle β , shown in Fig. 29. When $\beta > 90\text{deg}$, the tissue is under the arm and will be grasped when the device collapses. The critical contact angle of safety is set at 90 degrees. This ensures that the tissue is not grasped when the device collapses. Additionally, the impact of the protective cover on the strength requirements must also be evaluated.

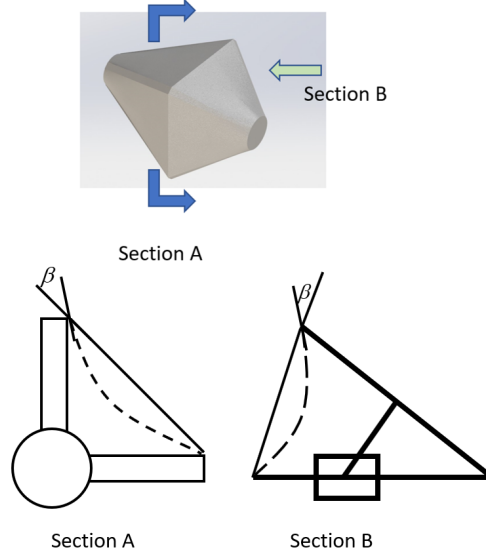


Fig. 29 The illustrations of the motorized expansion head covered with latex rubber and cross-sections with indentation angle β .

The tensile stress of stretching the cover is:

$$\sigma = eG \quad \text{Eqn. 62}$$

Where G is the tensile strength of the material, e is the elongation ratio. The force due to the elongation is:

$$F_{stretch} = wt\sigma \quad \text{Eqn. 63}$$

Where w is the width of the cross-section of the cover and t is the thickness. The energy cost to stretch the material is calculated using the difference between the surface area of the cover before and after stretching:

$$E_{stretch} = \int wteGL_0 de = wtL_0G \cdot \frac{1}{2}e^2 = \frac{1}{2}GtS_i e^2 = \frac{1}{2}GtS_i \left(\sqrt{\frac{S}{S_i}} - 1\right)^2 \quad \text{Eqn. 64}$$

Here the L_0 is the total length of the cross-section, S_i is the surface area in its neutral state, S is the surface area of the cover after stretching. In Eqn. 64, I assume t is a constant. The actuation force needed to expand with a cover was obtained by considering the contribution of pressure applied by the stomach tissue and the energy needed to stretch the cover. The area of the cover when the arm open angle is θ :

$$S_0 = l_{CD}^2 2\sqrt{2} \sin(\theta) \left(1 + 2\sin\left(\frac{\theta}{2}\right)\right) + S_i \quad \text{Eqn. 65}$$

The force needed to stretch the cover can be obtained from the virtual work principle, where the input of work is used to increase stretching energy:

$$\begin{aligned}
F_{stretch} &= \frac{dE_{stretch}}{dr} = \frac{d}{dr} \left(\frac{1}{2} EtS_t (\sqrt{\frac{S_0}{S_t}} - 1)^2 \right) \\
&= Etl_{CD} \left(1 - \sqrt{\frac{S_t}{S_0}} \right) \sqrt{2} \left(1 + \sin\left(\frac{\theta}{2}\right) + \tan(\theta) \cos\left(\frac{\theta}{2}\right) \right)
\end{aligned} \tag{Eqn. 66}$$

Thus, the total force for the actuation calculation is:

$$F_{total} = F_{vol} + F_{stretch} \tag{Eqn. 67}$$

With F_{total} replacing F_{vol} in Eqn. 41 and conducting the internal stress analysis, I can calculate the stresses in the new condition. After the head expands in the stomach, the tissue will compress the cover and push into the space between the arms. The new surface area can be obtained from:

$$S = l_{CD}^2 \frac{\beta}{\sin(\beta)} 2\sqrt{2} \sin(\theta) \left(1 + 2\sin\left(\frac{\theta}{2}\right) \right) + S_t \tag{Eqn. 68}$$

The tissue pushed into the cover is a volume of:

$$\Delta V = \left(\frac{2}{3} + 2\sqrt{2} \sin(\theta) \right) l_{CD}^3 \sin^2(\theta) \frac{\beta - \sin(2\beta) / 2}{\sin^2(\beta)} \tag{Eqn. 69}$$

By assuming S_t is relatively small and can be dropped when calculating $\sqrt{\frac{S}{S_0}}$, the elongation ratio where S_0 is used as the new neutral state is:

$$\sqrt{\frac{S}{S_0}} - 1 \approx \sqrt{\frac{\beta}{\sin(\beta)}} - 1 \tag{Eqn. 70}$$

$$P\Delta V = \frac{1}{2} EtS_0 \left(\sqrt{\frac{S}{S_0}} - 1 \right)^2 \tag{Eqn. 71}$$

$$\frac{P \left(\frac{2}{3} + 2\sqrt{2} \sin(\theta) \right) l_{CD} \sin(\theta)}{\sqrt{2} Et \left(1 + 2\sin(\theta/2) \right)} = \left(\sqrt{\frac{\beta}{\sin(\beta)}} - 1 \right)^2 / \left(\frac{\beta - \sin(2\beta) / 2}{\sin^2(\beta)} \right) \tag{Eqn. 72}$$

In the range from 0 to $\pi/2$, the right-hand side of the equation can be approximated as:

$$\left(\sqrt{\frac{\beta}{\sin(\beta)}} - 1 \right)^2 / \left(\frac{\beta - \sin(2\beta) / 2}{\sin^2(\beta)} \right) \approx 0.0105 \beta^3 \tag{Eqn. 73}$$

By calculating contact angle β 's and the elongation ratio as function of opening diameter, commercially available latex rubbers were evaluated, including a condom (thickness 0.08mm) and a 646Q balloon (thickness 0.4mm). The results, shown in Fig. 30, indicated that either a single or double layer of 646Q balloon could achieve a maximum contact angle of less than 90 degrees and an elongation rate of less than

100%. Thus, a single layer of 0.4mm thick latex rubber (646Q balloon) was found to be the optimal solution, as it provided sufficient tissue protection while using the minimum amount of material. The actuation force with a single layer cover is shown in Fig. 31, with L_{AB} set as 1.5cm. With the addition of the cover, the peak actuation force is 1059N.

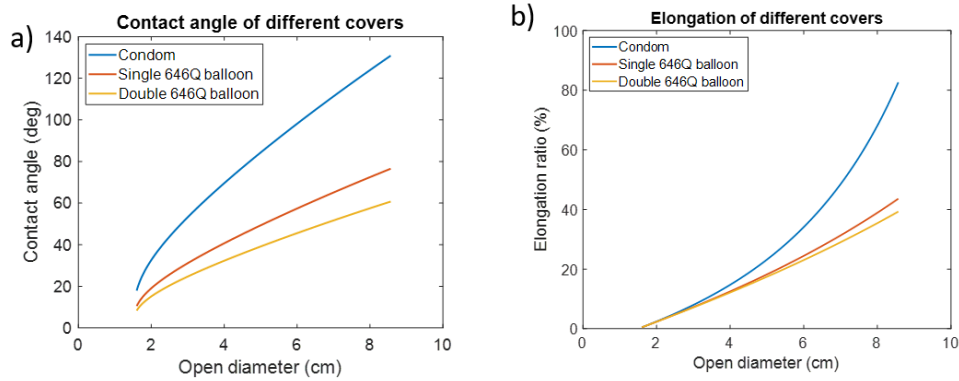


Fig. 30 a) Contact angle β and b) elongation rate of three different protective covers during the device expansion.

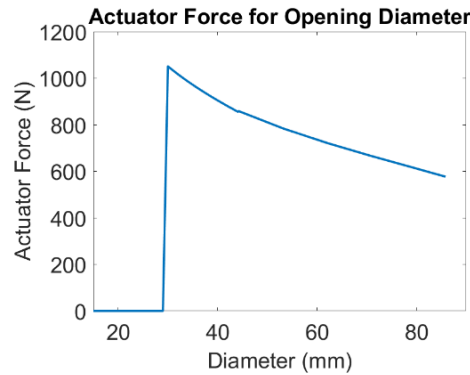


Fig. 31 Actuation force as a function of open diameter with single 646Q balloon covers.

Table 6 The value of stresses in a single 646Q balloon covered motorized expansion head.

Parameters		
Maximum actuation force F_a (N)	1059	1059
Outer arm width b (mm)	4	4
Outer arm thickness h (mm)	2	2
Inner arm width a (mm)	2	2
Inner arm height d (mm)	1	1
Inner and outer arm material	Al 6061	Titanium Ti-6Al-4V

Arm material yield strength (MPa)	240	880
Pin diameter at pivoted connection A r_{pin} (mm)	0.75	0.75
Pin material	Steel 304	Titanium Ti-6Al-4V
Pin material yield strength (MPa)	250	880
Leadscrew length $l_{leadscrew}$ (mm)	30	30
Leadscrew diameter (mm)	3	2
Leadscrew material	Steel 304	Steel 304
Max inner compression stress $\sigma_{compression}^{AB}$ (MPa)	130	130
Max outer arm stress σ^{CD} (MPa)	451	451
Max pin stress σ_{pin} (MPa)	562	562
Critical stress of buckling for inner beam (MPa)	249	416
Critical load of buckling leadscrew (N)	3514	3514
Arm strength requirement	No	Yes
Pin strength requirement	No	Yes
Leadscrew strength requirement	Yes	Yes

The results of the stress analysis indicate that Titanium Ti-6Al-4V is required for the construction of the arms and pins to ensure sufficient strength. On the other hand, Steel 304 can be used for the leadscrew material. The data in Table 6 also reveals that if the arms are constructed using Al6061, they will not have enough strength to resist and would buckle, while if the pins are made of Steel 304, they may fail under maximum load.

4.4 Motorized expansion head parts selection and manufacturing

In this work, efforts were made to make the device as compact as possible. To achieve this, the smallest leadscrew and motor that can provide sufficient actuation force were sought. An online calculator was used to convert actuation load into torque load [195], and the N20-6V DC motor is selected for its compact size and availability of gearboxes with different ratios [196]. The leadscrew and nut were chosen to be #5-40 UNC thread. The Al6061 was selected as the prototype material due to its machinability. The Tormach 440 PCNC was used to manufacture the inner and outer arms, while the housing was 3D printed with a Formlab 3D printer. The bottom plate was cut out of a 1/8inch thick Al6061 slab using an OMAX water jet. The

resulting prototype is depicted in Fig. 32, and a condom was selected as the protective cover. More details of the fabrication can be found in Table 7.

Table 7 Device actuation system data

Maximum load (N)	1059
Leadscrew type	#5-40 UNC
Leadscrew pitch diameter (mm)	3.175
Leadscrew pitch (mm)	0.635
Screw-nut type	Steel-Bronze
Coefficient of friction	0.04
Torque load (mN*m)	175
Motor model	N20 6V
Motor stall torque (mN*m)	0.7
Gear-box ratio	298
Output torque (mN*m)	108
Sufficient actuation	Yes

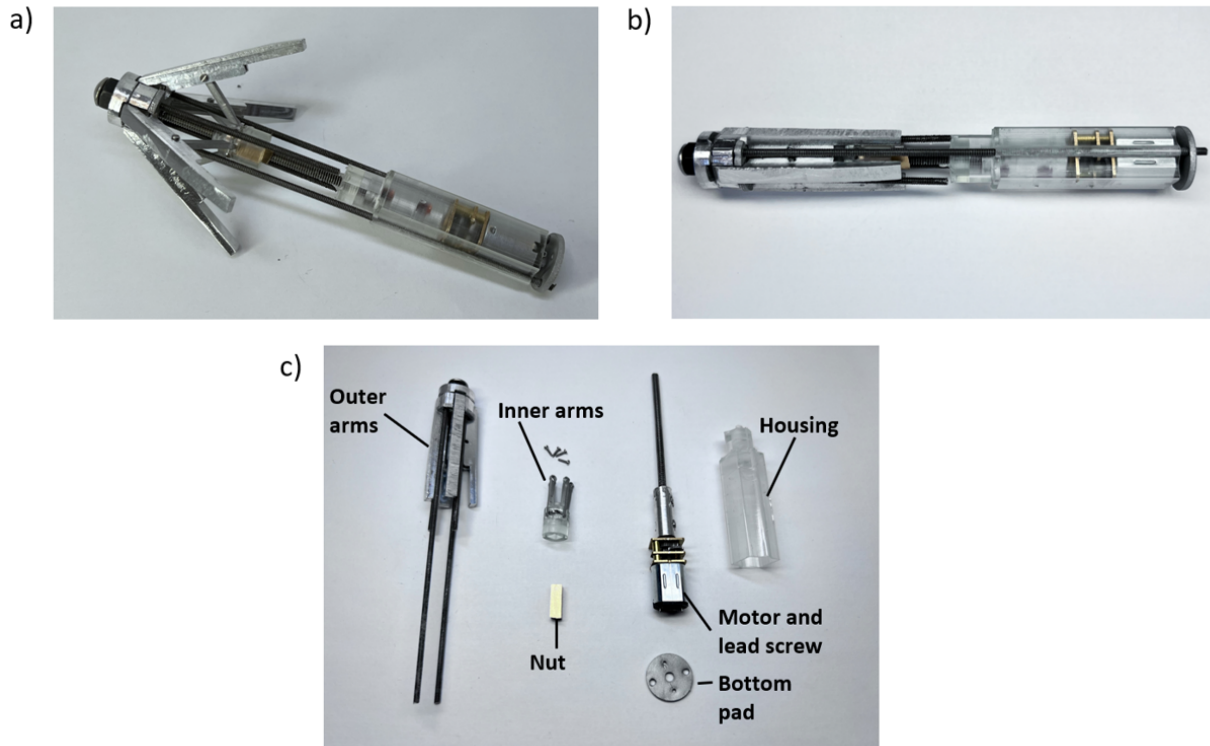


Fig. 32 a) Expanded and b) collapsed state of the prototype. c) Prototype disassembled.

4.5 *Ex vivo* and *in vivo* validations of motorized expansion head

In the *ex vivo* validation, I utilized a fully-grown pig's stomach (130kg) to test the stimulator's functionality of expansion. The device was operated using an Arduino Motor Shield Rev3 and an Arduino Uno microcontroller, which can be seen in Fig. 33. The Motor Shield provides 6V power to drive the N20 motor with a rated current of 160mA. To ensure that the device could expand freely and consistently, I conducted a series of tests by holding the expand button on the terminal for intervals of 5, 10, 15, and 20 seconds, repeating three times. Subsequently, I placed the expansion head in the pig's stomach and activated the expand button for 20 seconds, followed by pressing the contract button for 20 seconds to evaluate its performance.

In the *in vivo* studies, Yorkshire swine were obtained from Cummings School of Veterinary Medicine at Tufts University (Grafton, USA) and the experiments were pre-approved by the Massachusetts Institute of Technology Committee on Animal Care. The experiments were conducted in accordance with the approved protocols and all necessary precautions were taken to ensure the welfare of the animals. Pigs were sedated with an intramuscular injection of Midazolam 0.25mg/kg with Dexdomitor 0.03mg/kg and after intubation, anesthesia was maintained with isoflurane (1-3% in oxygen). After the experiment, pigs were returned to their pen and sedation was reversed intramuscularly with the reversal agent Atipamazole. If intubated, the pig was closely monitored until extubation and then was followed by monitoring of the recovery process until the pig was standing and considered bright, alert, and responsive. During the experiment, the pig was placed on a heated operating table with the additional thermal support of a heated blanket. Ophthalmic ointment is applied to both eyes. Once the pig was placed on isoflurane (1-2%) and oxygen (1-3%) either via a face mask or an endotracheal (ET) tube, it was then connected to an anesthesia monitoring machine in order to monitor vital signs every 15 minutes until returned to the pen. The motorized expansion head was delivered to a female pig of 95 kg through a 2cm incision on the stomach, with the aid of upper endoscopy and X-ray imaging to evaluate the expansion and contraction of the device in the stomach.

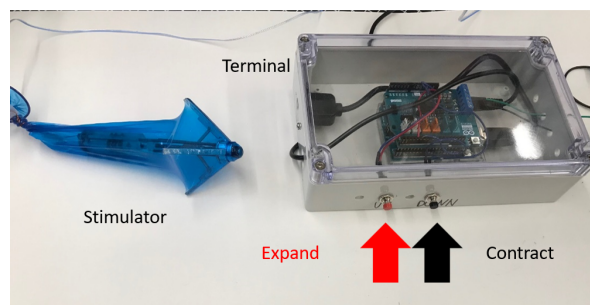


Fig. 33 Motorized expansion stimulator prototype with control terminal.

As shown in Fig. 34 a, the motorized stimulator requires 20 seconds to expand from a diameter of 20mm to 80mm. The stimulator was placed inside the pig's stomach and its expansion and contraction behavior was monitored. The results demonstrate that the stimulator is capable of expanding against the weight of the gastric tissue, as seen in Fig. 34 b. During the *in vivo* validation, an endoscopy video and X-ray (Fig. 34 c) were taken to observe the device during expansion. These images clearly show that the stimulator can push against the gastric tissue and expand.

Despite the success of the motorized expansion head, I found the manufacturing process to be lengthy and complex. As a result, I began exploring a less complex approach to the problem.

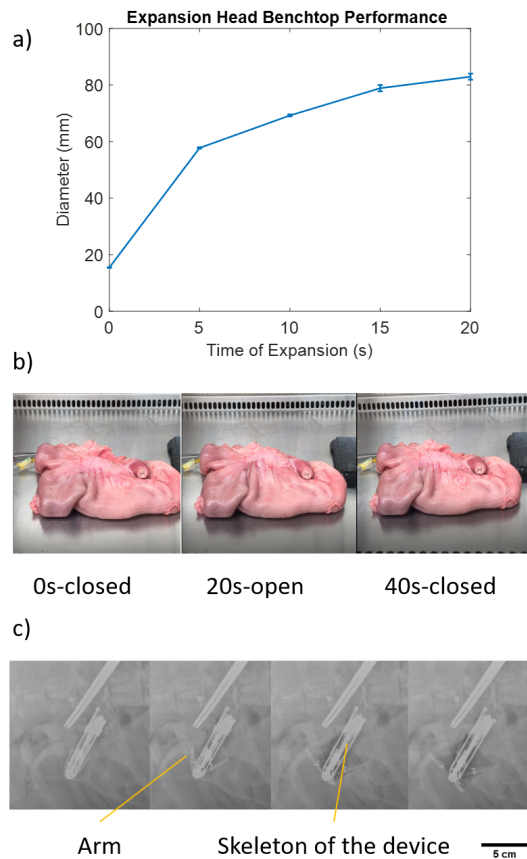


Fig. 34 a) Motorized stimulator head diameter vs expansion time. b) A cycle of expansion of the motorized stimulator head in the pig stomach. c) X-ray of motorized stimulator expands in the pig stomach in vivo.

Chapter 5. Pump-balloon dynamic satiety stimulator and its *in vivo* validation

5.1 Air balloon inflation system design and optimization

A simpler method of inducing satiety is through the placement of a gastric balloon in the stomach. This balloon inflates to create satiety and then deflates to prevent stomach accommodation. The procedure involves implanting a subject with a Percutaneous Endoscopic Gastrostomy (PEG) tube and delivering the balloon endoscopically to the stomach. The balloon is connected to a portable system via the PEG tube, as shown in Fig. 35.

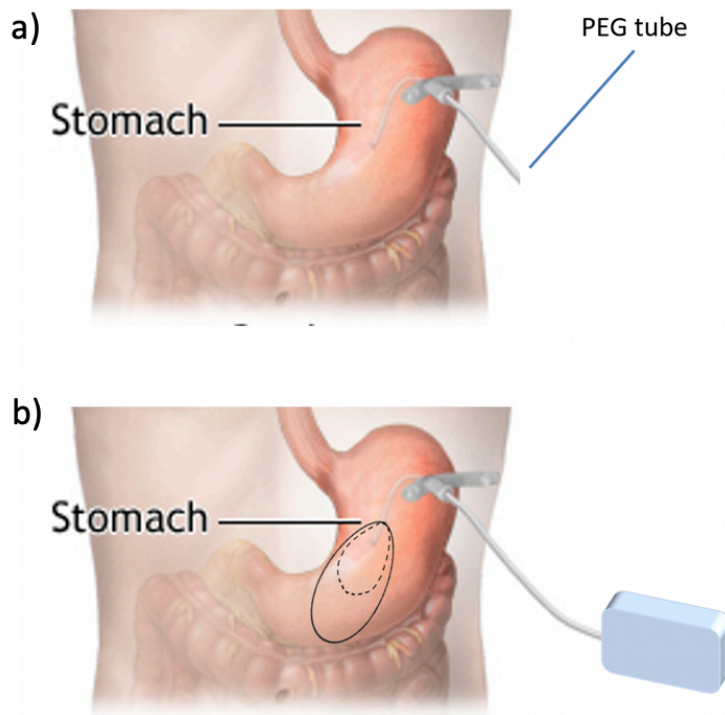


Fig. 35 Air balloon satiety stimulator system. a) PEG tube deployed onto the subject. b) An inflation tube connects the balloon with a portable pack.

To optimize the inflation system, I derived the pressure equation by integrating the Euler equation along the streamline. This equation (Eqn. 71) takes into account the stagnation pressure of the air bump (P_{stag}), air density (ρ), airflow rate (u), blade diameter (D_{blade}), blade width (b), volume rate (Q), pump input voltage (V) and current (I), pressure loss coefficients in the connections (k_{tot}), inner cross-section area of the tube (A), tube length (L), dynamic viscosity of air (μ), and blade angle (γ). The pressure loss is broken down into three components and written on the left-hand side of the equation: due to the blade (second term), connections (third term), and along the tubing (fourth term)[197].

$$P_{stag}(V, I) - \frac{\rho u \cot \gamma}{\pi D_{blade} b} Q - \frac{1}{2} k_{tot} \rho \left(\frac{Q}{A}\right)^2 - \frac{32 \mu L}{D^2} \cdot \frac{Q}{A} = P_{balloon} \quad \text{Eqn. 74}$$

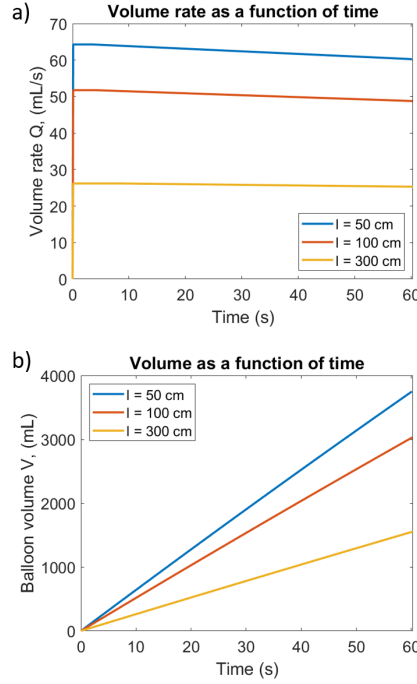


Fig. 36 a) The volume rate and b) balloon volume as a function of time with different inflation tubing lengths.

In this study, I used a commercially available air pump with a 65kPa stagnation pressure at 7.4V input voltage (Delinx Inc.). I chose not to modify the pump blade to maintain its structural stability. To determine the main source of pressure loss, I conducted an order of magnitude analysis. In the analysis, I set the cross-section of inflation tubing to have a 2mm inner diameter and the pump fills a 1L balloon in 60s. The results showed that the pressure loss due to connections was negligible considering a typical loss factor k_{tot} is about 10 to 1 (Eqn. 75), while the pressure loss along the tubing was significant, reaching up to 30% of the stagnation pressure (Eqn. 76).

$$f_{loss-connection} = \frac{P_{loss-connection}}{P_{stagnation}} = \frac{\rho Q^2}{2P_{stag} A^2} \approx 0.004 \quad \text{Eqn. 75}$$

$$f_{loss-tubing} = \frac{P_{loss-tubing}}{P_{stagnation}} = \frac{32 \mu Q}{D^2 A P_{stag}} \approx 0.3 \quad \text{Eqn. 76}$$

To further quantify the impact of tubing length and inner diameter on the inflation system, I numerically solved Eqn. 71 using a finite difference method on MATLAB. Results showed that as tubing length

increased, the volume rate decreased, and the balloon volume was smaller after 60s of inflation (Fig. 36). Additionally, alterations in the tubing inner diameter resulted in a significant change in both volume rate and volume over time (Fig. 37). These findings highlight the importance of selecting the appropriate tubing for an optimized inflation system. Considering these factors, I selected a Polyurethane inflation tube with 3mm outer diameter, 1.6mm inner diameter and 1.5m length as the inflation tube.

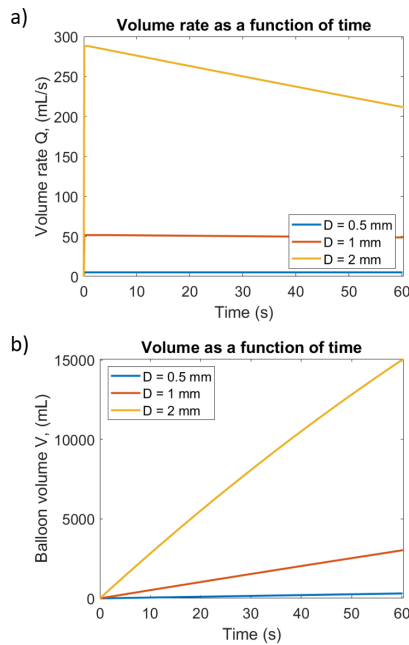


Fig. 37 a) The volume rate and b) balloon volume as a function of time with different inflation tubing inner diameters.

5.2 Design and fabrication of air valve and bifurcation

I developed a custom valve to regulate the airflow in the system. The housing was created by cutting an 11mm diameter McMaster FR4 rod into 25.5mm segments using a band saw. A 5/16inch tap was used to drill and thread the inner wall of the rod, forming a hollow cylindrical shape. This design allows the screw and motor-gearbox to open and close the valve. A hole, 10mm from the top, was drilled perpendicular to the axis of the housing using a drill press. The soft tubing was inserted into this hole, and a piston was added to clamp the tubing and regulate airflow. The design of the housing is depicted in Fig. 38. The components were assembled by inserting the shaft of the motor-gearbox into the complementary bore of the piston. The loose fit between the shaft and bore allows the piston to rotate with the shaft while moving along the housing axially. The motor ports were soldered with two wires. The housing was then placed onto the motor-gearbox, with the piston inside. Careful application of epoxy was used to secure the connection between the housing and the motor-gearbox, and shrink tubing was placed on top for added protection. A

5/16inch bolt stopper was inserted into the other end of the housing to create a tight clamp between the piston and bolt. The shrink wrap at the motor-gearbox end was also sealed with epoxy to protect its moving parts. The soft tubing was inserted through the drill-pressed hole in the housing. When the motor-gearbox rotates, the soft tubing is either clamped or unclamped. The valve was tested for airtightness during balloon inflation and deflation to ensure proper functioning. The finished air valve is shown in Fig. 39.

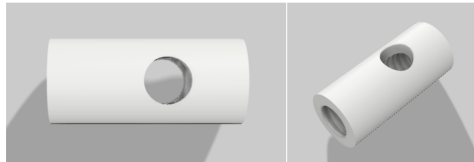


Fig. 38 Custom housing where the piston and soft tubing interact to restrict airflow to the balloon.

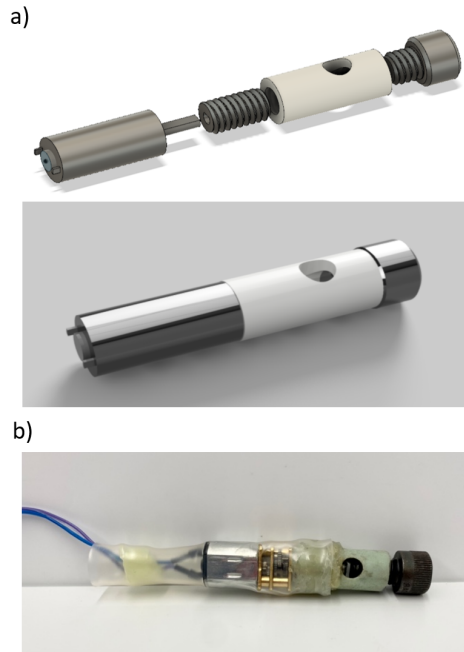


Fig. 39 a) The complete valve and its components, from left to right, consist of a motor-gearbox, a piston with a 5/16 inch outer thread, the housing, and a 5/16 inch thread bolt stopper. b) A photo of the functioning valve is shown with shrink tubing and epoxy securely connecting the top of the valve and the motor-gearbox.

The bifurcation serves as the link between the motor, valve, and balloon to regulate airflow. A 3-inch piece of 5.5mm diameter Delinx soft tubing and two 3-inch pieces of 3mm tubing were cut. The two pieces of 3mm tubing were inserted at least 0.5 inches deep into one end of the soft tubing. Epoxy was used to ensure a secure connection between the tubes, and shrink tubing was added to ensure an airtight seal. The final product is a bifurcation that connects the air pump to the soft tubing channel on one end, and the 3mm

tubing pieces to the valve and balloon for inflation on the other. An illustration and picture of the bifurcation are shown in Fig. 40.

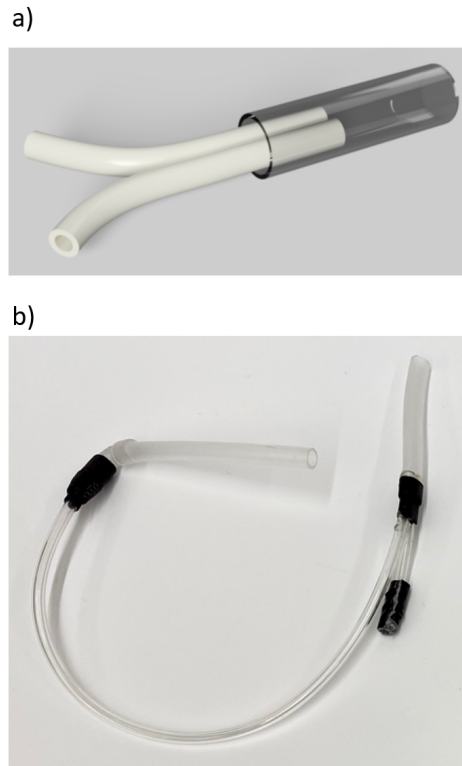


Fig. 40 a) The bifurcation is comprised of two pieces of 3mm tubing inserted into a piece of soft tubing. These tubes connect to the valve and air pump. The other end of the soft tubing connects to the balloon for inflation. b) A photo of the bifurcation design is shown with the left branch leading to the valve, the right branch leading to the balloon, and the top of the bifurcation connecting to the air pump through its soft tubing.

90-degree tubes were 3D printed to accommodate the angles in the box assembly and prevent tubing collapse during routing. One tube was attached directly to the motor with epoxy to ensure an airtight seal. The other end of the 90-degree tube was connected to the bifurcation using soft tubing. A second 3D-printed tube was also incorporated into the valve: one end of the tube was fitted with soft tubing, while the other end was fitted with 3mm tubing secured using duct tape. The system was tested by inflating and deflating the balloon to verify that the connections were airtight with the addition of the 3D-printed tubes. The 90-degree tube and the assembly of the airflow system are shown in Fig. 41.

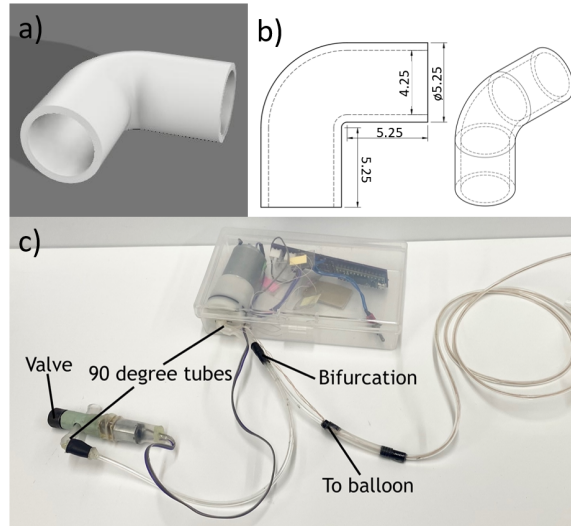


Fig. 41 a) An illustration of the 90-degree tube. b) Dimensional drawing of the 90-degree tube. c) Assembly of the airflow system.

5.3 Balloon durability and fluid mechanical tests

Given that the balloon will remain in the stomach once inserted, it is crucial to select a material that can withstand repeated inflation cycles for at least 3 months. To determine the balloon's durability, I conducted a series of tests on various types of balloons in a simulated stomach environment. The durability experiment involved several components, including a balloon, a water tank, an acrylic plate, a water sensor, a water sensor holder, a container lid, a power supply, a digital multimeter, and a laptop, as shown in Figs. 42 and 43. To prepare the water tank for the experiment, I followed these steps: first, I marked the water level on the side of a 5L transparent plastic tank with increments of 0.25L. Then, I added 0.25L of water at a time to the tank and marked the tank's water level until it reached 4.5L. I secured an acrylic plate as the partition at the 2.5L mark to prevent the balloon from floating post-inflation. The partition was large enough to block the balloon but didn't prevent water from flowing freely. I also cut out two openings on the lid, one on the edge for water sensor placement and the other for the balloon tube to go through. These components were critical to the success of the experiment and ensured accurate measurements of the balloon's durability.

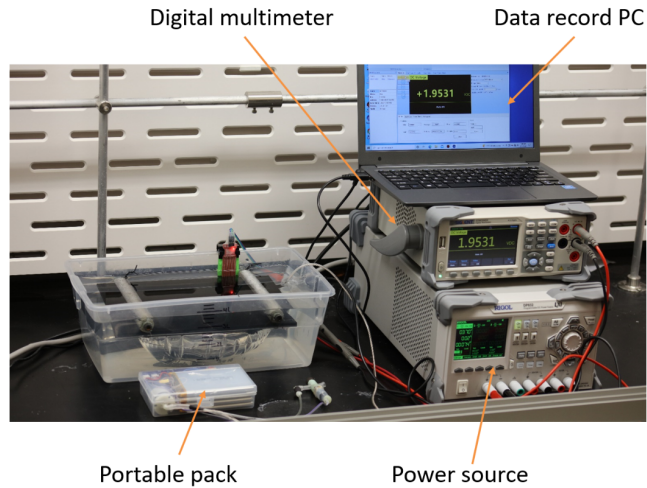


Fig. 42 Durability test set up.

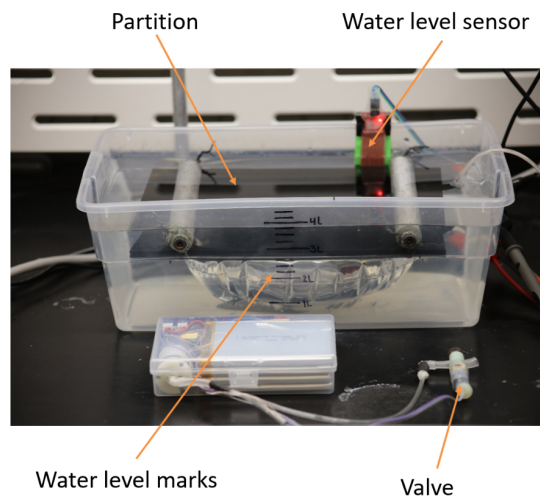


Fig. 43 The partition-tank system to monitor the water level/balloon volume.

For this experiment, I used the Songhe water sensors, which have three pins: input, ground, and signal. I connected the pins to the water sensor using female-to-male jumper wires and then placed the wires through heat shrink tubing to ensure waterproof protection. Next, I applied epoxy on the connections to secure them in place, blew hot air to shrink the tubing, and waited for 5 minutes for the epoxy to dry. To hold the water sensor in place, I made a holder according to the dimensions and specifications outlined in Fig. 44. I then placed the water sensor into the holder, which allowed us to collect accurate measurements of the balloon's durability in the simulated stomach environment.

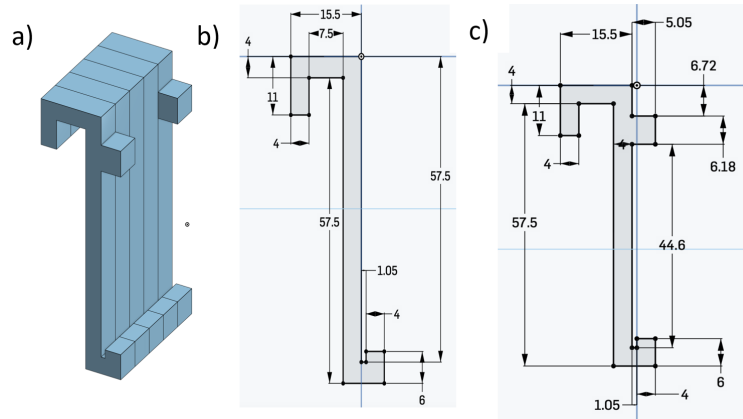


Fig. 44 CAD drawings of the water sensor holder composing five individual strips. a) Isometric view, b) sketch of inner strips, and c) sketch of outer strips are shown with dimensions in millimeter.

Once I prepared the tank, lid, and water sensors, I passed the balloon through the hole cut out on the lid and placed it underneath the partition in the water tank. Using the holder, I hung the water sensor in the interior of the tank and added water until it reached the bottom of the water level sensor, which was approximately 2.5L. To minimize evaporation, I closed the lid. I supplied 3.3V to the water sensor and connected the signal terminal to the positive terminal of the digital multimeter (DMM), making sure the power source, multimeter, and water sensor were all connected to the same ground. After connecting the DMM to a computer with the EasyDMM software installed, I turned on the device and recorded the data using the autosave function. As the experiment could take multiple days, I made sure the computer was connected to a power source and turned off the automatic sleep mode.

Before conducting the durability tests, I wanted to confirm that the tank setup could accurately simulate the stomach environment in terms of confinement. To achieve this, I conducted *in vivo* experiments and found that the pressure inside the balloon in real situations could range from approximately 96 kPa (uninflated) to 101 kPa (at full inflation) (Fig. 45 a). I then compared the *in vivo* test graph with the partition-tank system graph (Fig. 45 b) and found that by inflating the balloon from 0L to 1.5L, I could create a pressure inside the balloon that ranged from approximately 98 kPa to 106 kPa. These results confirmed that the partition-tank system could simulate confinement comparable to the real stomach, which allowed us to conduct accurate and meaningful durability tests on the balloon.

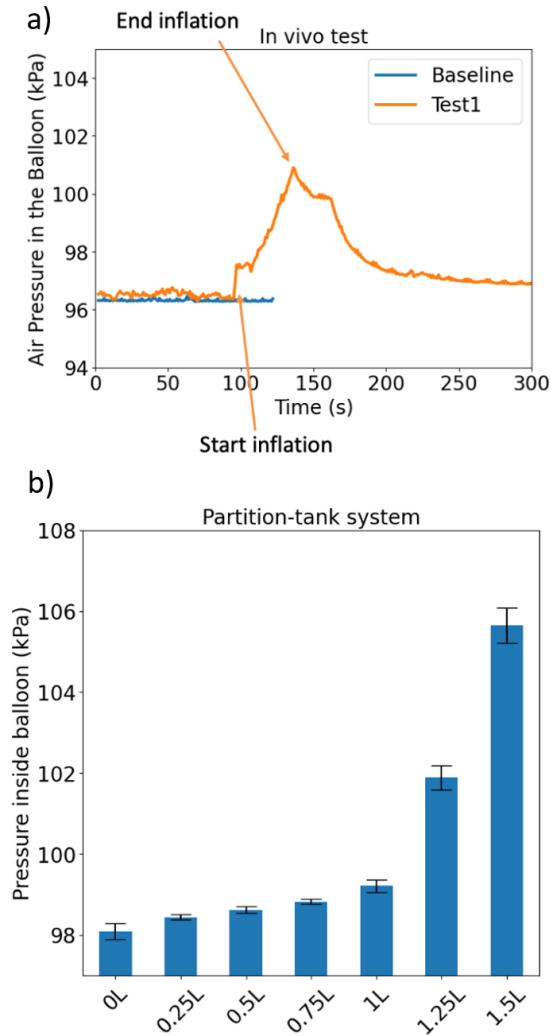


Fig. 45 Intra-balloon pressure measured a) in-vivo versus in the b) partition-tank system during an inflation cycle.

To test the durability of each balloon, I repeatedly inflated and deflated the balloon until it burst or leaked inside the tank. The water level sensor monitored the condition of the balloon, inflation and deflation cycles resulted in regular alterations in water levels. Any burst or leakage of the balloon resulted in an irregular change in the water level. I recorded the water level change to count the number of cycles the balloon endured and the point at which it failed. I selected the 20-inch PVC balloon among three candidate materials, which included a latex condom and an 18-inch latex balloon, based on its performance in the durability test. As shown in Fig. 46-48, the condom and latex balloon remained functional for only about 30 and 100-200 cycles in the pH7 environment, respectively, while the PVC balloon survived over 2000 cycles in a pH2 environment. The pH2 environment is created by mixing Acetic acid with water. These results indicated that the PVC balloon was the most durable of the three materials and could withstand repeated inflation and deflation cycles for an extended period of time.

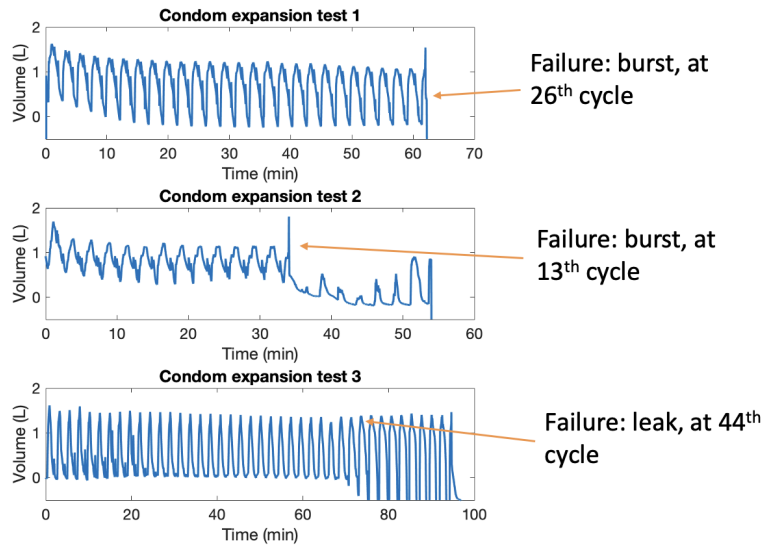


Fig. 46 Inflation cycle graphs of the condom balloon in pH7 environment.

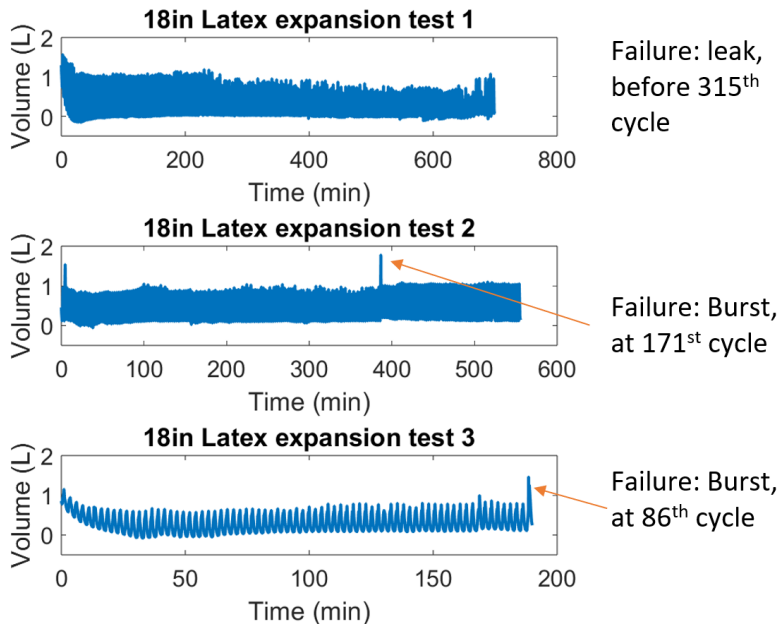


Fig. 47 Inflation cycle graphs of latex balloon in pH7 environment.

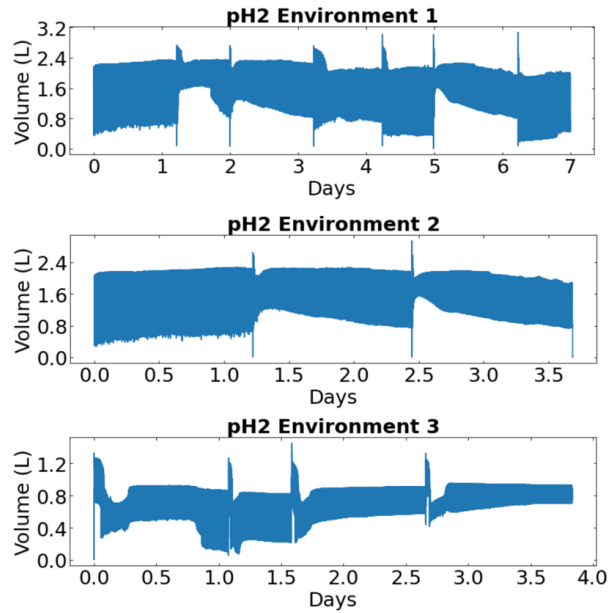


Fig. 48 Inflation cycle graphs of PVC balloon in pH2 environment.

I conducted further tests to verify that the PEG clip did not interfere with the inflation of the balloon. After placing the PEG tube onto the subject, the clip is required to clamp the tube, thus avoiding the exit of gastric content through the PEG tube. The PEG tube connected to the balloon passed through a PEG clip with six levels, providing eight different tightness levels ranging from no clamp to the tightest level (Fig. 49). The clamp levels, from least to most tight, were as follows: no clamp, sham, level 1, level 2, level 3, level 4, level 5, and level 6.

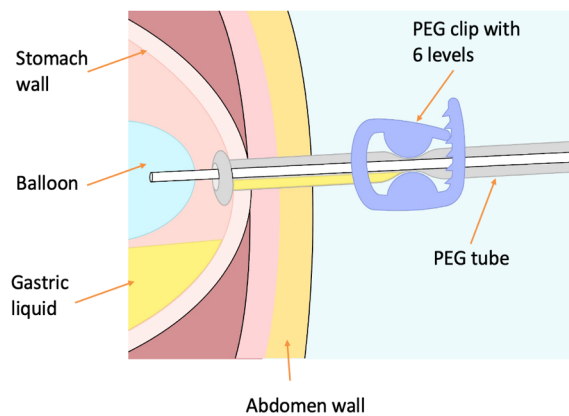


Fig. 49 Demonstration of the PEG tube and clip setup.

To measure the effect of the PEG clip on balloon inflation, I conducted experiments and recorded the results, which are shown in Fig. 50. The findings indicated that the time it took to increase the water level by 1.5 L was approximately 100 seconds for all levels of tightness, except for level 6, where the time

increased to approximately 200 seconds. These results suggest that clipping the PEG tube at any level from 1-5 will not affect the inflation of the balloon. However, using level 6 may cause a significant delay in the time it takes to inflate the balloon, which may impact the results of future experiments. Therefore, I concluded using a PEG clip with a tightness level of 5 or lower to ensure that the inflation of the balloon is not affected by the clip.

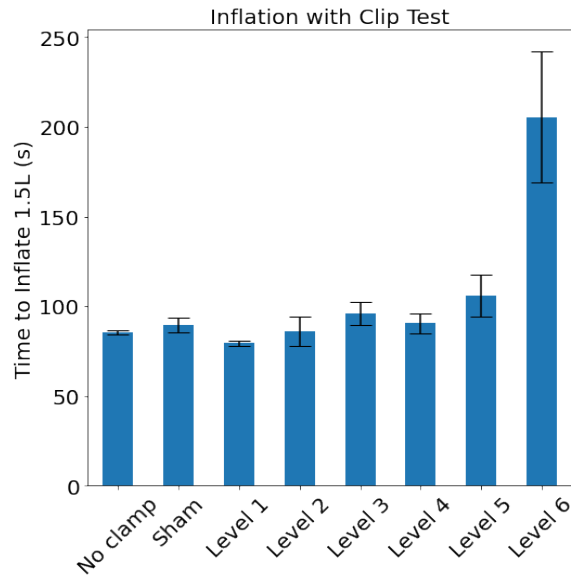


Fig. 50 Time to inflate the balloon by 1.5L with different levels of the clip.

5.4 Electronic design and control algorithms of balloon stimulator

In the prototype, I employed a Teensy 3.2 board and a custom PCB board to control the inflation and deflation of a PVC balloon located inside a pig's stomach. The balloon is inflated prior to feeding time to occupy the stomach and induce satiety, thereby reducing the amount of food taken by the pig during the meal. After eating, the balloon is deflated, and the device enters a dormant state until the next feeding time. The design of the device, including its airflow and wiring, is shown in Fig. 51. The inflation tube is placed inside the PVC balloon and the other end is connected to a bifurcation. This bifurcation splits into two channels, one connecting to the pump and the other to the valve, allowing us to control the inflation, hold, and deflation stages.

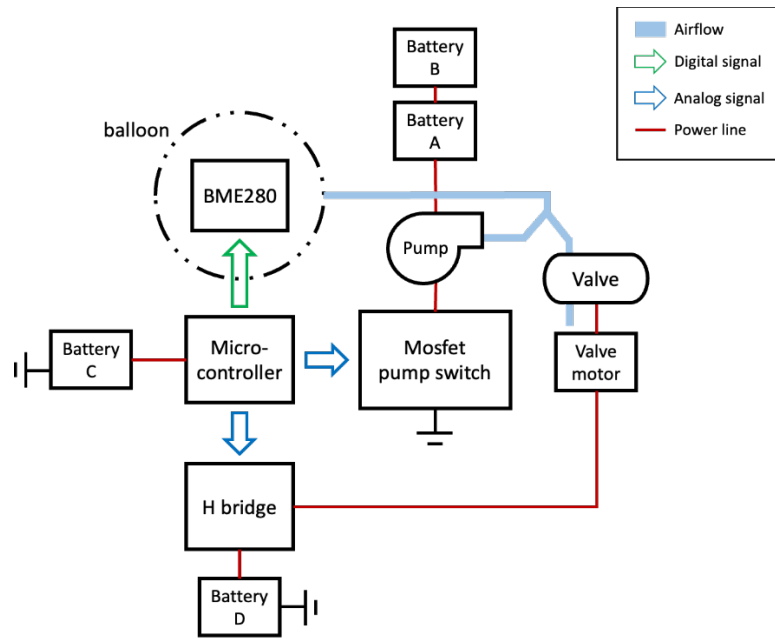


Fig. 51 The wiring and airflow diagram of the balloon dynamic satiety stimulator system.

The BME280 pressure sensor breakout is integrated with the Teensy board through an I2C bus. The sensor continuously sends digital signals reflecting the current pressure inside the balloon. The control function maintains a record of the latest 10 readings and calculates the moving average as the current pressure within the balloon. When the moving average reaches the predetermined threshold pressure, the inflation pump is automatically turned off to ensure the safety of the subject. The valve and pump are powered by lithium batteries, with the valve powered by a 3.7V battery and the pump by two 3.7V batteries connected in series to produce a 7.4V voltage. Two analog I/O ports on the Teensy 3.2 are connected to the H-bridge controlling the valve, enabling the motor to rotate and move the piston, opening and closing the soft tubing channel. The pump is controlled by a MOSFET switch connected to one analog I/O port. The PCB board file and circuit schematics are shown in Figs. 52 and 53 respectively. The battery utilized in this system possesses a 6Ah capacity per cell. During the in vivo evaluation of the system, which will be detailed subsequently, the pump's rated current during balloon inflation was recorded at 0.6A. Given that each inflation cycle requires 60 seconds, the dual battery configuration can sustain 600 operational rounds. If the balloon is inflated three times daily before each main meal - breakfast, lunch, and dinner - the pumping system, powered by two batteries, can function for a total of 200 days. It is worth noting that both the valve and the microcontroller are also powered by a 6Ah lithium battery. The valve is propelled by an N20 motor, with a rated voltage of 3V and a current rating of 50mA. The valve motor necessitates 10 seconds to either close or open the inflation tube. With an energy cost of 1.5J per inflation/deflation, the battery can facilitate 53,280 rounds of operation. The microcontroller demands 60mA of current in its awakened state and merely

100uA in sleep mode. For every day of operation, the microcontroller is active for a cumulative 110 seconds, maintaining system functionality, while remaining in sleep mode the rest of the time. This amounts to a daily energy cost of 56J, and a single lithium battery pack can support 1,430 days of such operation. Upon comparing the maximum operational duration of the pumping system, valve, and microcontroller, it is evident that the device can run for 200 days without interruption, with the pumping system acting as the operational limit.

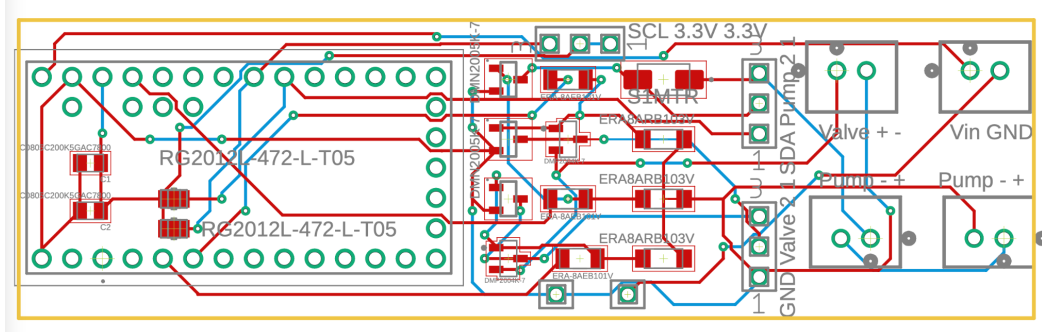


Fig. 52 PCB file created on Eagle PCB.

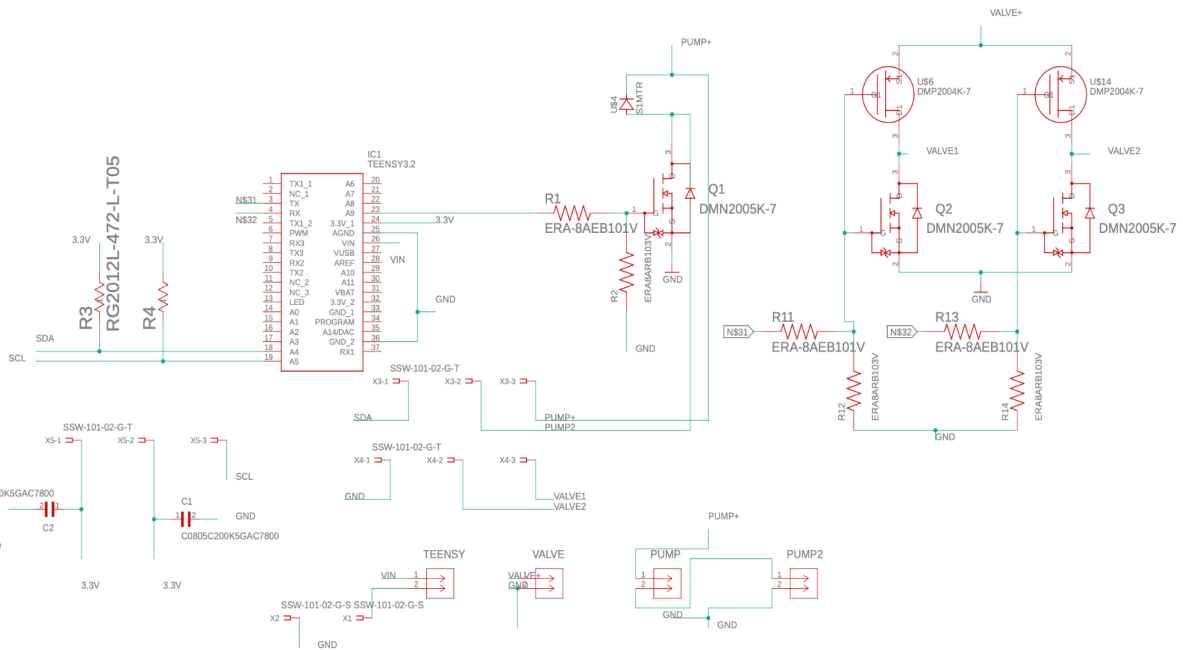


Fig. 53 System circuit schematic.

Our device operates in five distinct modes: Initial Delay, Inflation, Hold, Deflation, and Snooze. Inflation, Hold, and Deflation make up a single cycle of inducing satiety, while the Initial Delay compensates for the time required to set up the device on the subject. The Snooze mode is a low-power consumption sleep state. I have created a feeding schedule for the subject, and input the feeding times into the Teensy 3.2. A control

algorithm has been programmed to inflate and deflate the balloon according to the pre-set feeding schedule. To conserve energy, I have integrated a Snooze library that allows the Teensy 3.2 to enter sleep mode between active operations. The feeding times of the pig are entered into the control algorithm before device setup, and are used to calculate the timing and duration of each Snooze period. Throughout the day, the device transitions through different modes based on the set feeding times, as illustrated in Fig. 54.

The device operates in the following sequence:

1. Upon initial activation, the device enters an Initial Delay mode, in which it is set to Snooze until the next scheduled feeding time. This delay allows for the preparation of the device and its deployment. The time remaining until the next feeding time is pre-entered into the device before it is set to Snooze.
2. At the scheduled feeding time, the device is awoken from Snooze mode and begins inflating the balloon. During inflation, the valve is closed by rotating the valve motor forward and the pump motor is activated to pump air into the balloon. Inflation stops either when the pressure inside the balloon reaches the set threshold or the pre-determined inflation time has elapsed.
3. After the balloon is inflated to the desired pressure, the device enters a Hold status, in which the pump motor stops pumping air into the balloon and the valve remains closed to maintain the balloon's pressure. The Hold status lasts for one hour.
4. The device then enters a Deflation mode, during which the pump motor remains at a low voltage and the valve motor rotates in a backward direction to open the valve and deflate the balloon. This process takes approximately 5 seconds. The device then returns to Snooze mode until the next scheduled feeding time.
5. The Teensy Snooze library is utilized to put the device into a low-power status. The Snooze Alarm function is used to periodically wake the device up every hour to prevent any malfunction in time calculation.

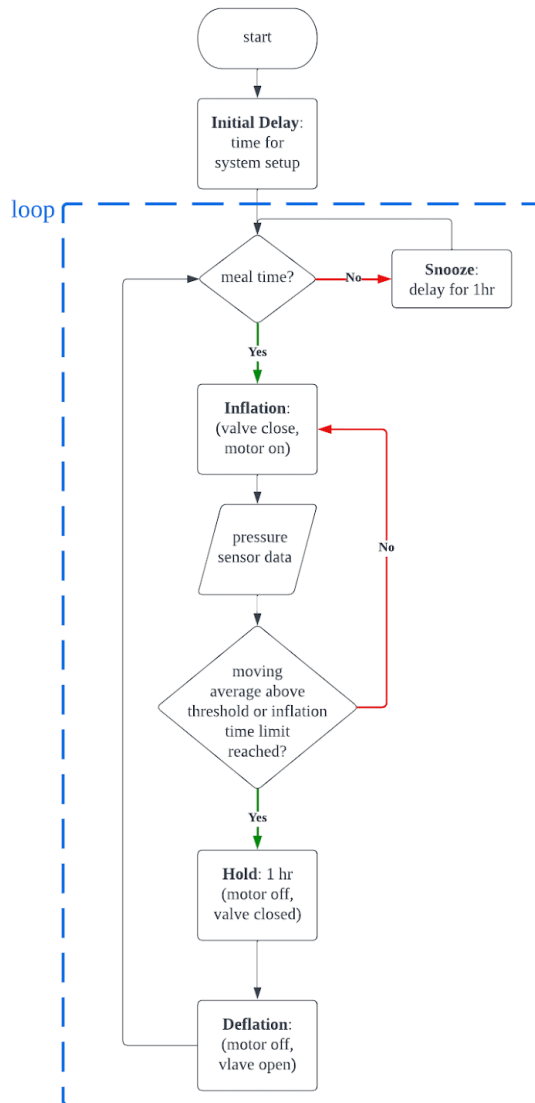


Fig. 54 System control algorithm flow chart.

The stopping mechanism of the inflation process involves both pressure and time thresholds. Based on preliminary *in vivo* studies, I have determined that a pressure of 103,000 Pa is ideal to accommodate the anatomy of the pig's stomach, corresponding to a balloon volume of 1-2L depending on body weight. Any readings above 130,000 Pa or below 80,000 Pa are considered outliers and are filtered out. If the moving average exceeds 103,000 Pa, the inflation is stopped. The time threshold for inflation is set at 1 minute, which is the estimated time for the balloon to reach 2L. The decision to use a 2L inflation volume was made after meticulous consideration of the balloon size required to induce satiety. As per the referenced study [188], balloons of 1.2L or 1.8L are sufficient to induce satiety in pigs that weigh between 20-25kg. Considering the pigs utilized in this study have an average body weight of approximately 40kg, a 2L gastric occupation is deemed appropriate and reasonable. If either the pressure or time threshold is exceeded, the

inflation process is terminated. The Teensy Snooze library provides three snooze options: Sleep, Deep Sleep, and Hibernate. In this work, I use the Deep Sleep function and Snooze Alarm to set the Freescale Kinetis processor in the Teensy board to a low-power mode and later wake it up. The procedure to configure the Snooze function is as follows:

1. Include the Snooze library header:
`#include <Snooze.h>`
2. Load the desired driver classes:
`SnoozeTouch touch;`
`SnoozeDigital digital;`
`SnoozeTimer timer;`
3. Install the Timer and Digital drivers to the SnoozeBlock:
`SnoozeBlock config(timer, digital);`
4. Configure the drivers, typically by changing certain parameters:
`timer.setTimer(5000); // milliseconds`
`digital.pinMode(21, INPUT_PULLUP, RISING); // pin, mode, type`
`digital.pinMode(22, INPUT_PULLUP, RISING); // pin, mode, type`
5. Provide the SnoozeBlock to the desired Snooze function from the Snooze class:
`Snooze.sleep(config);`
`Snooze.deepSleep(config);`
`Snooze.hibernate(config);`

I performed an *in vitro* test to evaluate the functionality and sleep-wake behavior of the system. During the test, the balloon was positioned under the partition in the water tank to simulate the stomach environment. The control algorithm was loaded into the Teensy board and programmed to inflate the balloon at 8am, 12pm, and 5pm, hold the volume for 1 hour after each inflation, and then deflate it. This mimics the pig's feeding schedule in the *in vivo* experiments, and the volume change of the balloon was recorded by monitoring the water level. The DMM multimeter was turned on and the water sensor data was recorded using EasyDMM. The device was allowed to run for three days, and the recorded water level sensor data was analyzed to confirm normal inflation behavior. Fig. 55 shows the data collected by the water level sensor over a three-day interval during the *in vitro* experiment. Each spike in the graph represents a complete inflation-hold-deflation cycle. The results indicate that the system can operate stably for 2 days with 3 cycles per day.

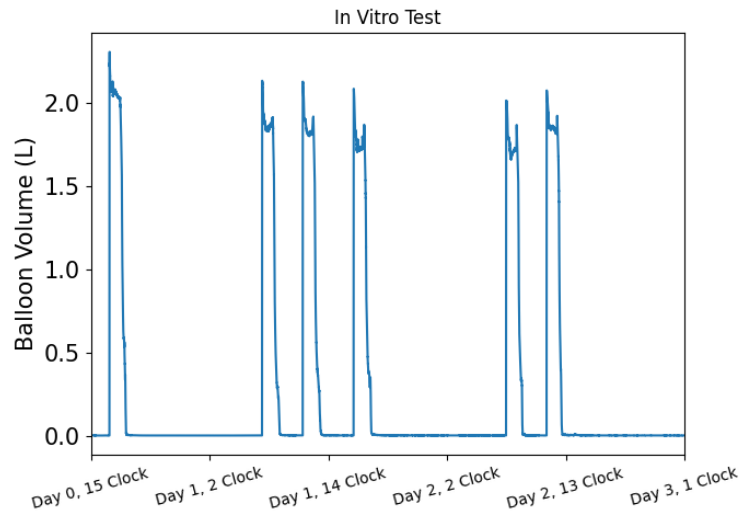


Fig. 55 Water level data for the three days in vitro evaluation.

5.5 Portable balloon stimulator integration

I have designed a portable pack for an *in vivo* survival study to investigate whether the prototyped device can decrease satiety in swine. Given the need for space efficiency, I have condensed the device to ensure ease of use. The flow of the integration process is depicted in Fig. 56. Initially, I mount parts onto the PCB manufactured by OSH Park and upload the code that automates timed inflation and deflation onto the Teensy 3.2 microcontroller. Next, I prepare the balloon and container. Lubrication is injected into a 1.5 meter long 1.8mm inflation tube, through which four thin wires for the air pressure sensor are threaded. The wires are soldered onto the air pressure sensor, which is then inserted into the balloon. I seal the balloon with epoxy to maintain its airtightness and move on to modify the container. Two holes are cut out of the container, one for wiring and the other for the tubes, and I place the four batteries, the PCB, a power switch, and a motor inside. Finally, I connect the balloon air pressure sensor wires to the PCB and use a 90-degree tube to facilitate airflow in harsh bending angles. To ensure the durability of the compact system, I perform *in vitro* tests. I begin by placing a horizontal partition inside a 5L box and positioning the balloon below the divider. I then fill the box with water, allowing a water level sensor to detect any changes in balloon volume as it inflates and deflates. The data from both the water level sensor and air pressure sensor is monitored and recorded externally using a computer.

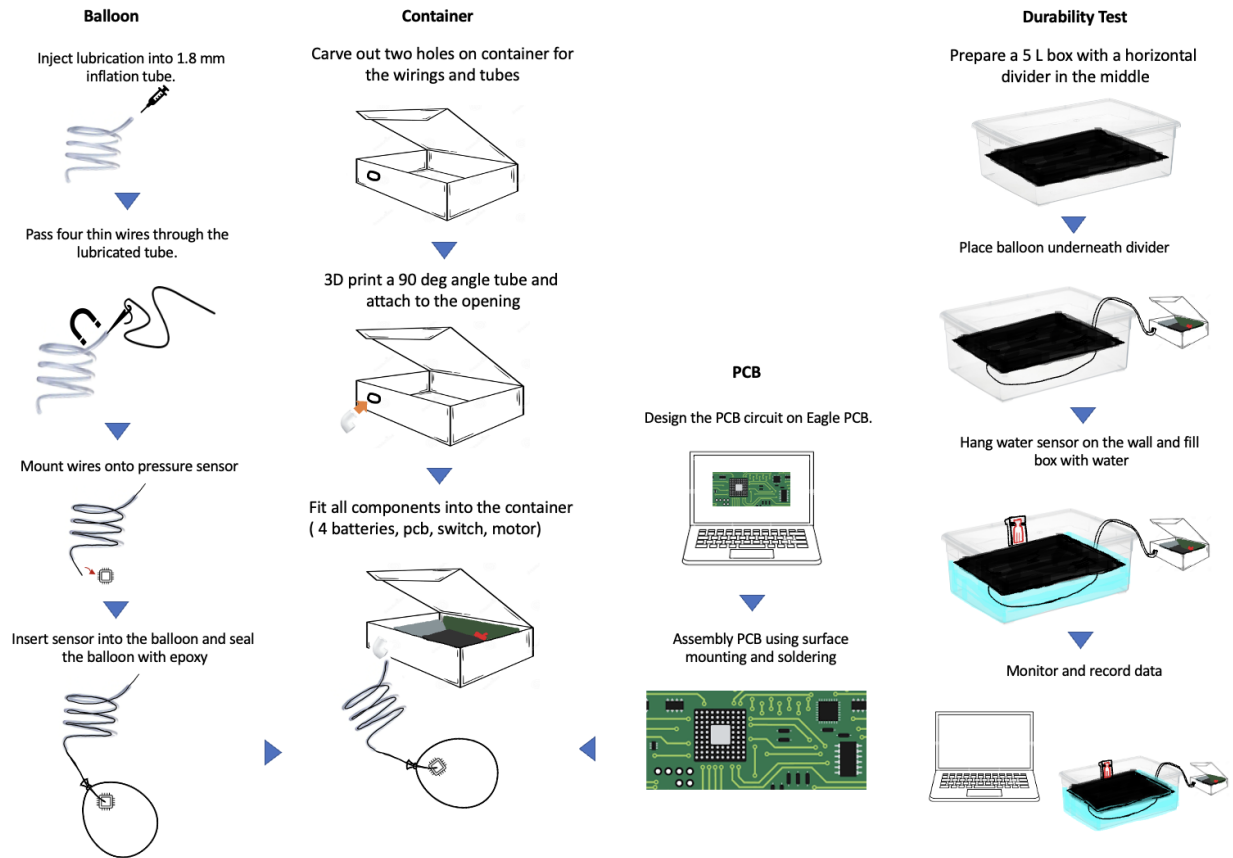


Fig. 56 Integration chart showing instructions on portable pack assembling and durability test setup.

5.6 In vivo validation of air balloon stimulator

The preliminary *in vivo* study in swine models involves the use of a balloon with an internal air pressure sensor, an Arduino Uno board with four gator pins, a power source, a pump to inflate and deflate the balloon, and a PEG tube. The study begins by deploying an overtube into the pig. A fishing wire through the PEG tube into the stomach and retrieved using a clip in the endoscope. PAM oil is applied to the balloon to reduce friction before delivering the balloon system into the stomach. The fishing wire is attached to the inflation tube, opposite the balloon. To prevent fluid and debris from entering the airflow system, a tube cap is inserted into the tube at the end away from the balloon (Fig. 57). The fishing wire is then pulled from the PEG tube until the 3mm tube exits the PEG tube, providing access to the system. After the balloon is placed into the stomach of the pig, the inflation tube is subsequently connected to the portable pack. A PEG clip is used to stop the exit of gastric content through the PEG tube. The portable pack is secured onto the back of the pig using bandages. The PEG tube is flushed with saline once a day and the bandages on the pig are changed twice a week.

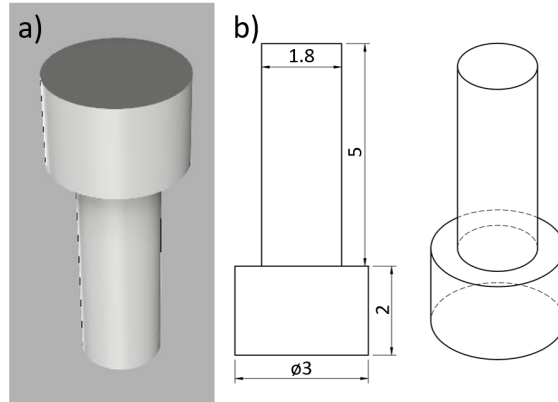


Fig. 57 a) The model and b) the dimensions of the 3D-printed tube cap is designed to fit into the 3mm tubing and prevent debris from entering the air tubing during retrieval through the esophagus and stomach.

I conducted an *in vivo* test to validate the air balloon stimulator. As shown in Fig. 58, the inflation tube can be passed through the PEG tube, and the PEG clip can be used to prevent the overflow of gastric content. After placement, the balloon was inflated for 1 minute via the inflation tube, resulting in the visible expansion of the abdomen.

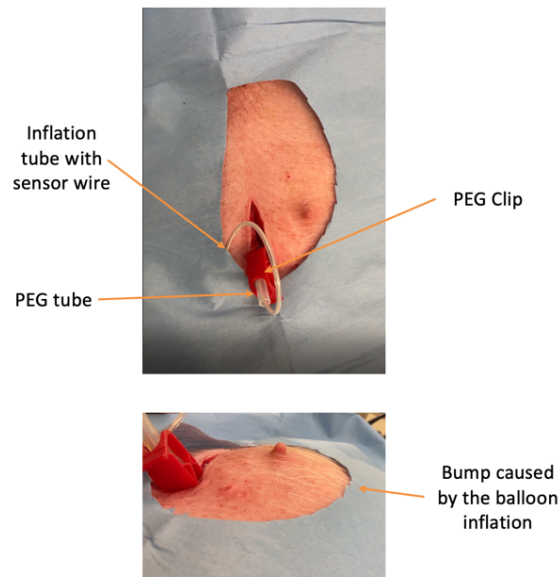


Fig. 58 The air balloon stimulator device during an *in vivo* deployment (top) and the resulting expansion of the abdomen due to balloon inflation (bottom).

The functionality of the device was further validated through the collection of air pressure data within the balloon. The balloon contained an air pressure sensor that recorded levels of inflation in the stomach. As depicted in Fig. 59, the collected data showed a consistent increase in air pressure, demonstrating the

compatibility of the air balloon stimulator with the PEG tube and clip. The air pressure data displayed a consistent increase and trajectory in all three tests above the baseline, thereby validating the air balloon system *in vivo*.

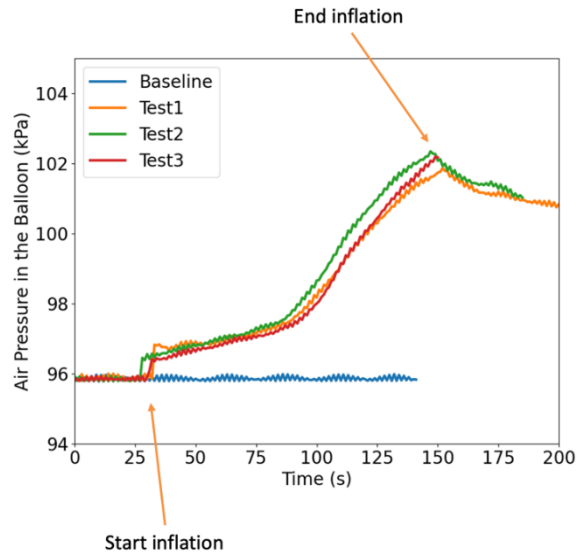


Fig. 59 Data collected from inflation tests based on readings from the air pressure sensor. A baseline measurement taken without inflation was included.

5.7 Feeding behavior change caused by air balloon stimulator

To evaluate the effectiveness of the device in reducing food intake, I conducted a feeding behavior study using a swine model. We purchased a 40 kg Yorkshire swine from Cummings School of Veterinary Medicine at Tufts University (Grafton, USA), and the study was pre-approved by the Massachusetts Institute of Technology Committee on Animal Care to ensure animal welfare. We followed all approved protocols and took necessary precautions to guarantee the swine's well-being. To start the experiments, we placed a PEG tube in the sedated swine and allowed it to recover for two days before deploying the stimulator. Throughout the study, we fed the swine twice a day, at 08:30 AM and 01:30 PM, with 1360g (3lbs) of pellets each time. During the 30-minute feeding period, we monitored the amount of food consumed and weighed the remaining food, which we later returned to the pig in accordance with the Massachusetts Institute of Technology Committee on Animal Care's policy.

The experiment comprised three types of days: control, sham, and measuring. During control days, the pig had the PEG tube but not the satiety stimulator. On sham days, we placed the satiety stimulator in the pig, but it remained inactive. Measuring days involved expanding the satiety stimulator twice a day in the pig's

stomach at 08:30 AM and 01:30 PM. The valve closed the air channel, held the air for 30 minutes, and subsequently deflated. On the morning of days 3, 7, and 10, the pig was sedated to allow for bandage exchange and was only fed at 01:30 PM. The device was deployed into the pig on the third day of the experiment and removed on the thirteenth day. To offset the growth factor of the pig, I mixed measuring days and sham days when the device was placed on the pig. The experiment schedule is presented in Table 8 and the 30 minutes food intakes are shown in Fig. 60.

As shown in Fig. 60, the mean food intake during control, sham, and measuring meals were 268g, 284g, and 94g, respectively, with corresponding standard deviations of 133g, 144g, and 118g. The p-values between control-measuring, sham-control, and sham-measuring were 0.8, 0.02, and 0.01, respectively. The study revealed a significant decrease in food intake during the measuring meals, where the balloon was expanded prior to feeding. The reduction in food intake was over 60% compared to the control and sham groups (p -value < 0.05). However, I observed no significant changes in feeding behavior due to the presence of the balloon in the stomach, as indicated by the small differences in food intake between the sham and control groups and a very large p -value. Based on this result, it can be concluded that the inflation of the balloon prior to the meal is the sole factor responsible for the observed changes in feeding behavior.

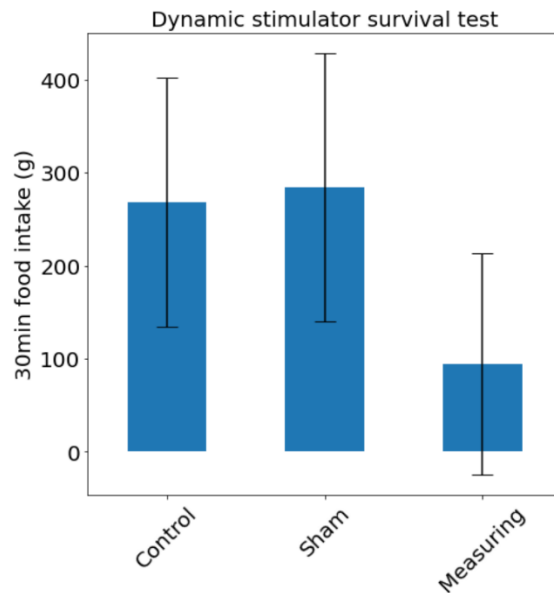


Fig. 60 30 minutes food intakes during the feeding behavior experiment.

Table 8 The feeding schedule during the feeding behavior experiment.

Day	1	2	3	4	5	6	7	8	9
Type	Control	Control	Sham	Measuring	Sham	Measuring	Sham	Measuring	Sham
Day	10	11	12	13	14	15	16	17	18
Type	Sham	Measuring	Sham	Control	Control	Control			

Chapter 6. Conclusion and outlook

In my thesis I developed of a conformal motility mapping platform that can measure 3D global pressure distribution in the GI tract. This platform is able conform to anatomic and dimensional variation across subjects and demonstrates the ability to evaluate changes in pressure within the stomach, esophagus, and anorectal canal. To achieve measurements of pressure in these distinct areas I employed a shape memory metal (Nitinol)-support coupled to sensing arrays. The sensing probes use thin Nitinol strips, designed according to the anatomic shape/dimension of the GI tract, as supporting structures and can be linearized to support endoluminal deployment. Linear Nitinol strips are used as supports in esophagus and rectum probes. The supporting Nitinol of the stomach probe is pre-programmed into a coil-like structure. Once the probe is inside the body, the thermal energy from the subject triggers the phase transition in the Nitinol and the probe then conforms to the shape of the stomach. The probes deliver pressure sensing units to the luminal wall and map the motor patterns. Upon completion, all three probe can be retrieved by withdrawing a cable connected to the probe. Through *in vivo* swine studies, I benchmarked the performance of the system to an FDA-approved HRM catheter through pressure mapping in the esophagus and rectum. The accuracy of the stomach sensing probe was confirmed by applying known external and internal forces to the animal and measuring the resulting pressure distribution.

In the benchtop prototype, the maximum width of the sensing probe is 1 cm. Based on the *in vivo* study in the swine model, this probe is small enough to support deployment and retrieval. Given that the maximum diameter of an FDA-approved HRM probe is 4mm, future work will be focused on further miniaturization of the system.

The dimensions of the stomach sensing probe are highly dependent on the size of the stomach and the Nitinol support has the capacity for future personalization depending on body habitus of the subject. In this work, I designed the supporting structure based on the dimensions of the stomach in a 75-100 kg female swine model. In the current prototype the sensors were directly attached to the supporting Nitinol band. In the future, further personalized measurements could decouple these elements.

Evaluation of gastric motility in clinical practice is limited to evaluation of gastric emptying only. However, patients without delayed gastric emptying or any structural abnormalities commonly experience a constellation of symptoms described as “functional dyspepsia,” which is poorly understood. This is due to the uncertain correlation between perception of discomfort and changes in gastric motility/pressure, for which evaluation is limited as there is no existing method to map spatial pressure distribution within the stomach. I have developed a device capable of mapping gastric pressure in a minimally-invasive manner,

which may be applied to human investigations in the future. This may enable correlation of symptoms with changes in gastric motility patterns, which has the potential to transform our understanding, diagnosis, and treatment for patients with yet-to-be defined gastric motility disorders.

Future successful translation of these technologies will require further evaluation across a range of disease states as well further development on fabrication techniques and exploration of the potential for personalized probes that maximize data collection across a range of subject body habitus.

In my thesis, I developed two dynamic satiety stimulators for endoscopic delivery, designed to promote feelings of fullness over the course of several weeks. These stimulators expand pre-meal to stimulate satiety and then contract post-meal to prevent gastric accommodation and loss of stimulation. Two methods have been developed for stomach expansion: a motorized expansion head and a balloon approach. The motorized expansion head features a system with four arms driven by a DC motor to expand against gastric tissue. A latex cover is added to protect the tissue from being grasped by the arms during contraction. This approach has been validated in a swine model and shown to expand freely within the stomach. The balloon stimulator system includes a PVC balloon delivered endoscopically, a PEG tube allowing inflation, and a portable pack for controlling inflation and deflation. Prior to a meal, the portable pack inflates the balloon and holds the air for the duration of the meal. After the meal, the pack releases the air and allows the balloon to collapse within the stomach. The balloon also has an internal pressure sensor to monitor gas pressure and avoid over-inflation, ensuring safety. To minimize energy costs and extend operation time, the balloon is programmed to enter sleep mode during non-active times. A feeding behavior study in a swine model showed a 60% average reduction in food intake with the activation of the balloon stimulator.

The development of a fully functional motorized head capable of stimulating an awake subject presents a challenge due to the high cost of the required high-strength Titanium Ti-6Al-4V. This significantly limits the practical application of the system and calls for further improvement in its structural design to minimize internal stress and reduce fabrication costs using cheaper materials.

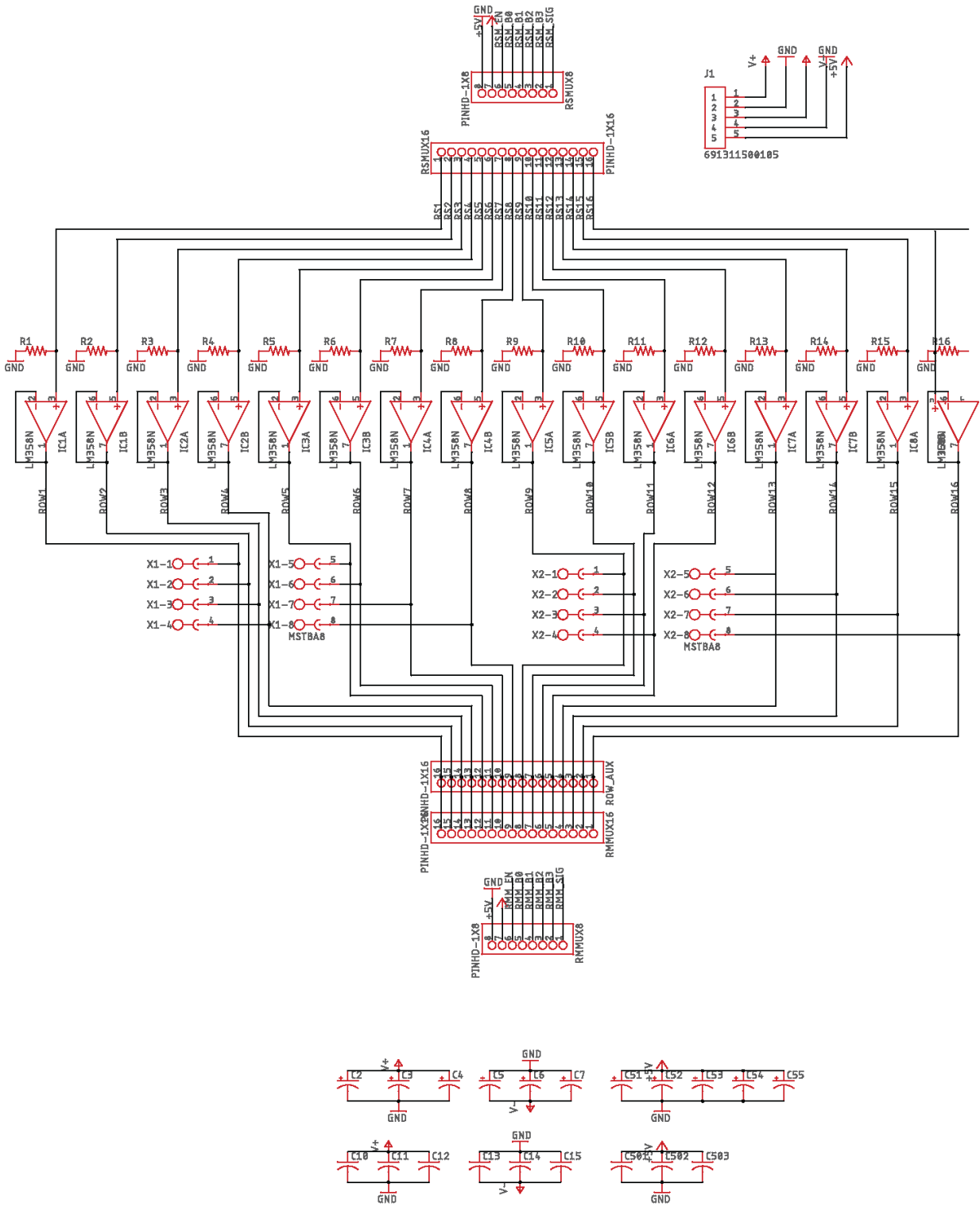
While this study has demonstrated the effectiveness of the balloon dynamic satiety stimulator in altering feeding behavior and reducing food intake, it remains uncertain if this dynamic stimulation can outperform static stimulation in avoiding stomach accommodation. Further research, such as a long-duration comparison study with a static intragastric balloon, is necessary to fully understand the potential benefits of the dynamic stimulation approach.

Appendix A. Scanning board circuits

Appendix A a-b are the full circuit diagram of the motherboard of the pressure mapping system. The connector RMUX8 and RMUX16 are the sockets of CD74HC4060 multiplexers mounted on breakout boards (DigiKey P/N 1568-1181-ND). Similarly, RSMUX8 and RSMUX16 are the sockets of CD74HC4060 multiplexers mounted on breakout boards (DigiKey P/N 1568-1181-ND). Connector X1-2 holds a 16-pin Molex (DigiKey P/N 102-6418-ND) for row connections of the sensing matrix. Connector X3-4 holds a 16-pin Molex (DigiKey P/N 102-6418-ND) for column connections of the sensing matrix. Appendix A c is the PCB board file of the scanning system. Appendix A d is the circuit diagram of the daughterboard with all reference resistors and feedback resistors. As governed by Eqn. 33, the feedback resistors' must be optimized to produce a measurable voltage without saturating the amplifier or causing excessive current (Appendix A m). In this design, reference resistors are 1.00 kOhm (DigiKey P/N RNCF1206TKY1K00CT-ND) and 10.00 kOhm (DigiKey P/N 10KADCT-ND), and feedback resistors are 4.70 kOhm (DigiKey P/N 4.7KADCT-ND). Placing these resistors on a daughterboard enables the measurement of various ranges of resistances by replacing daughterboards with another.

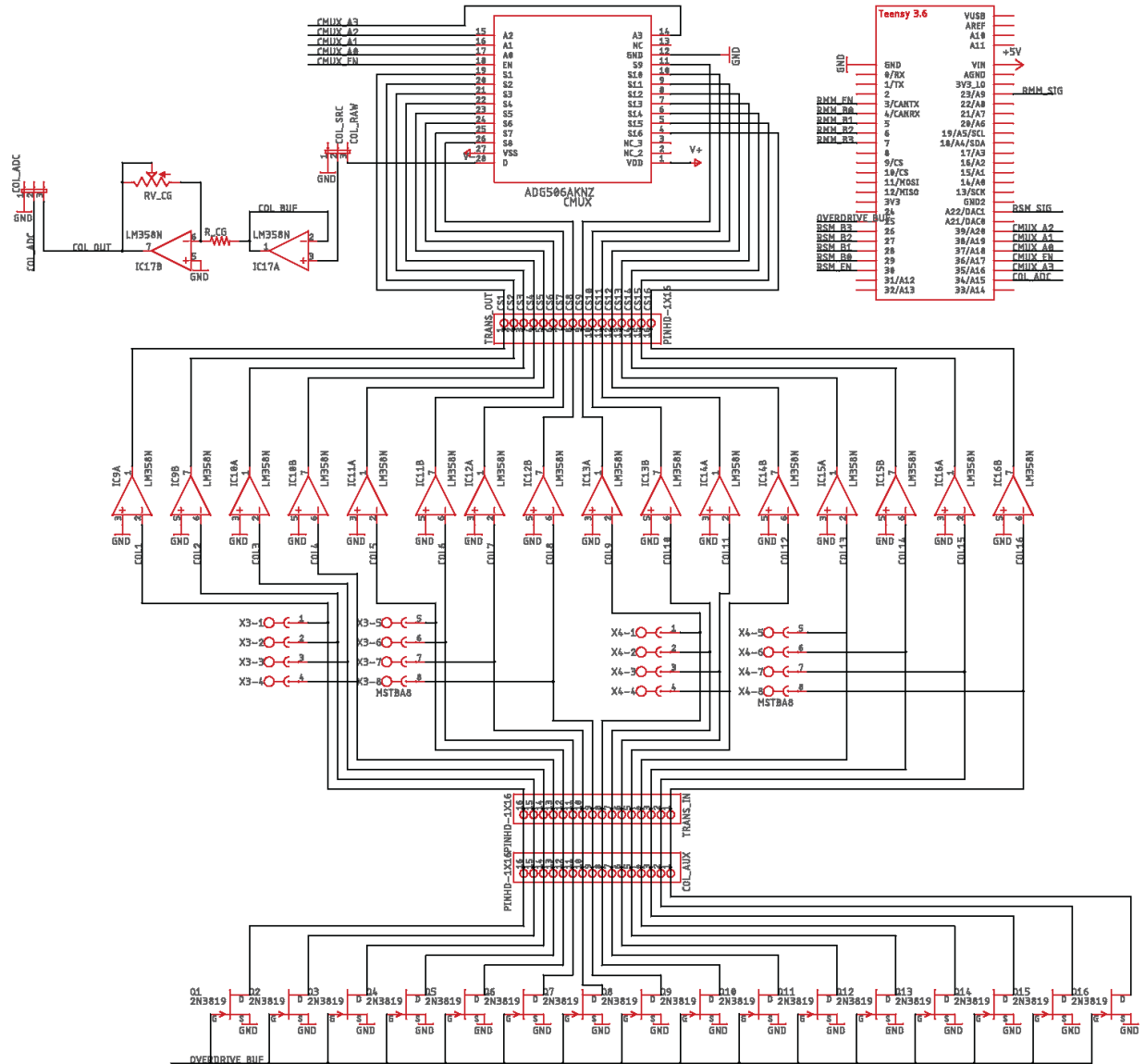
The connectors TRANS_IN and TRANS_OUT connect to the daughterboard. They connect the feedback resistors on the daughterboard to the output and negative feedback port of each operational amplifier (Appendix A b) (LM358N, DigiKey P/N 296-9554-5-ND). Since the connector TRANS_IN is connected to X3-4 (Appendix A b), reference resistor R17-R48 (Appendix A d) (DigiKey P/N 4.7KADCT-ND) shares the column connections in the sensing array. Therefore, these reference resistors become additional rows to the sensing array. The row connections of reference resistors are made through JP3 (Appendix A d) to connect ROW_AUX (Appendix A b) via jumper wires and become row 14 and 15. Appendix A c- e show the PCB layout of the motherboard and daughterboard. Boards are manufactured with FR-4 process, 1.6mm board thickness and 1oz copper density.

a)

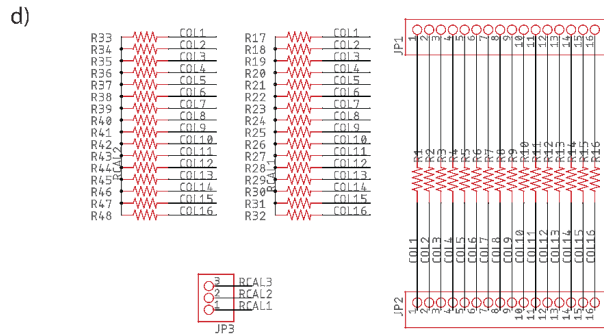
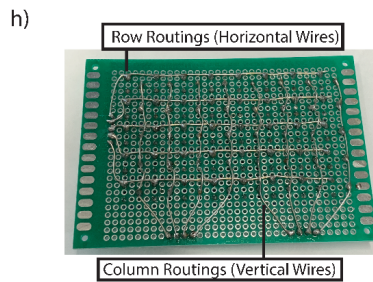
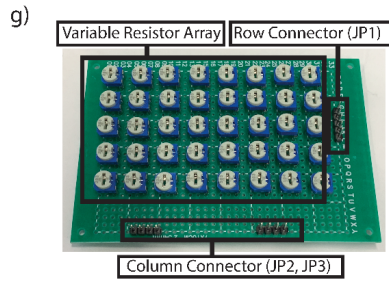
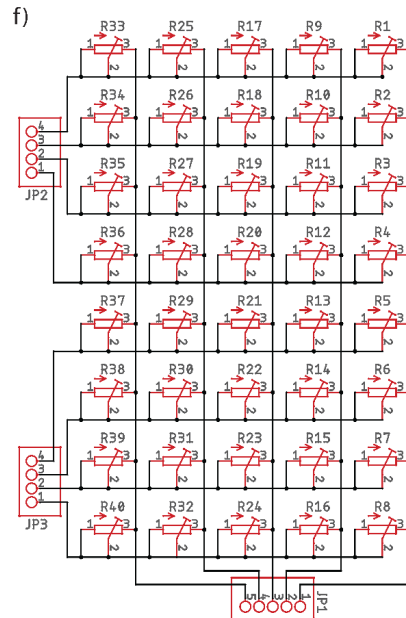
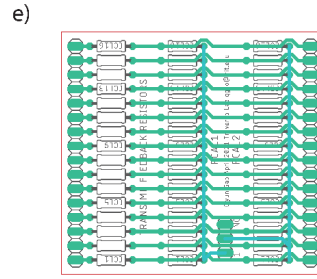
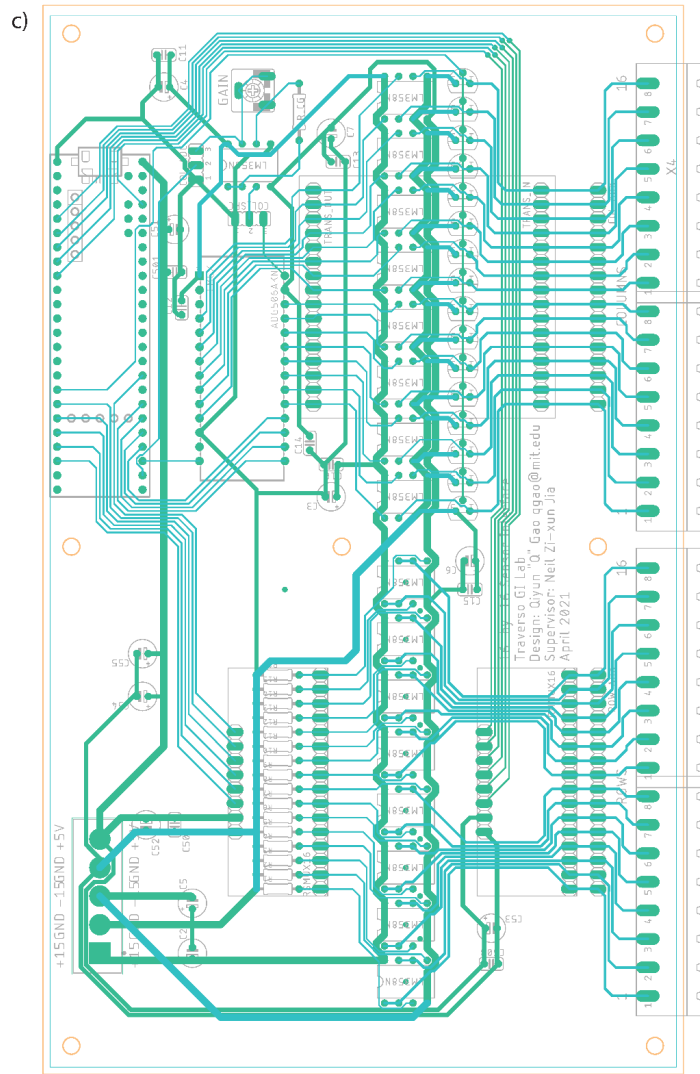


a) Full schematic of the scanning board row part.

b)

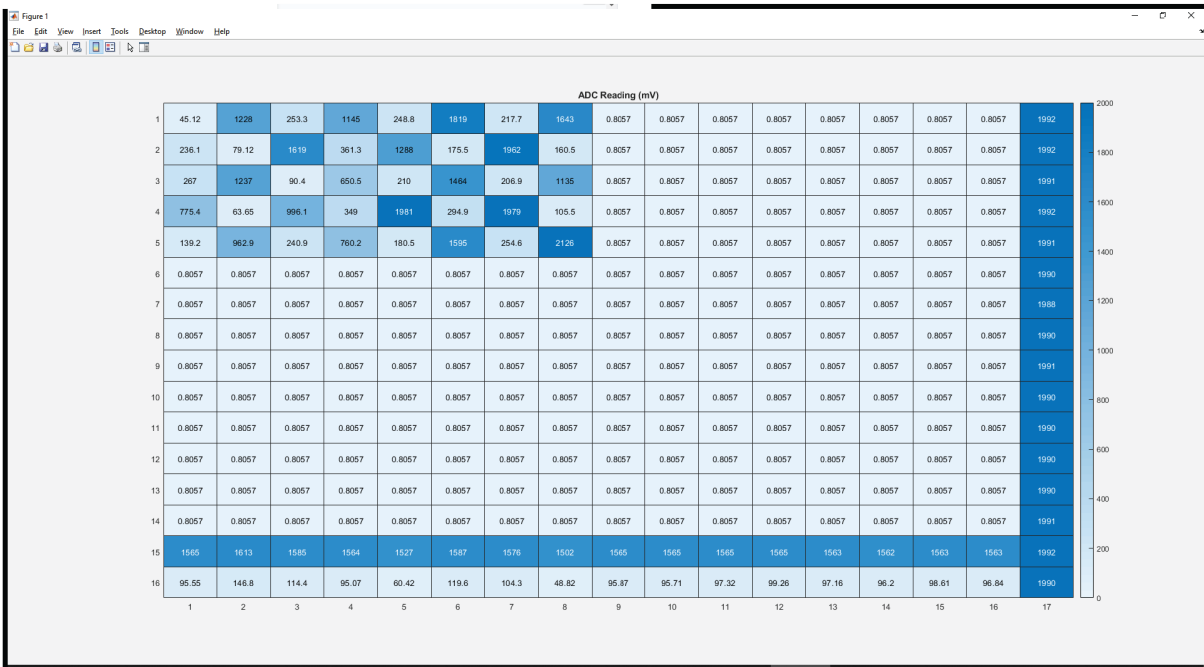


b) Full schematic of the scanning board column part.

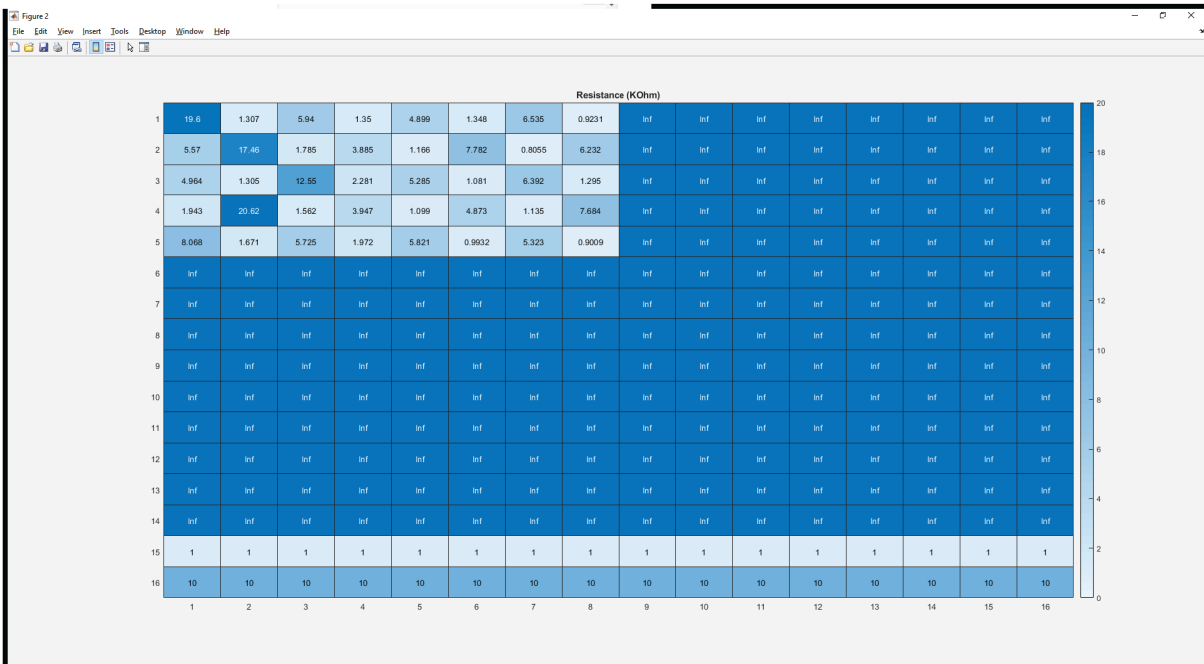


c) PCB file of the scanning board. d) Schematic of the resistance reference board. e) PCB file of the resistance reference board. f) Schematic of the resistor array used for crosstalk test. Resistor array g) front and h) back photo.

i)



j)

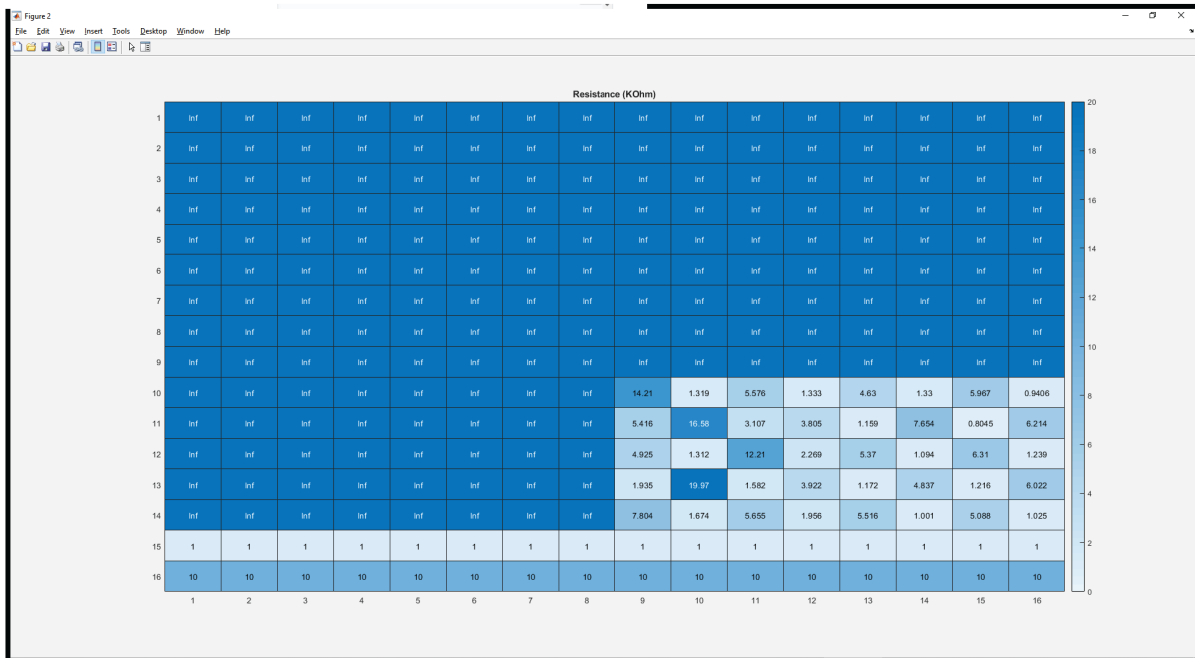


i) MATLAB interface screenshots of voltage when resistor array is connected to row 1-5, column 1-8. j) MATLAB interface screenshots of resistance when resistor array is connected to row 1-5, column 1-8.

k)

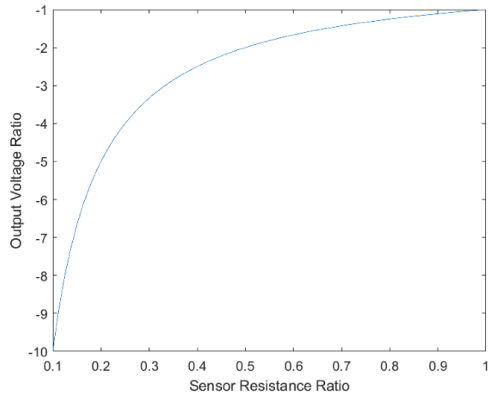


l)

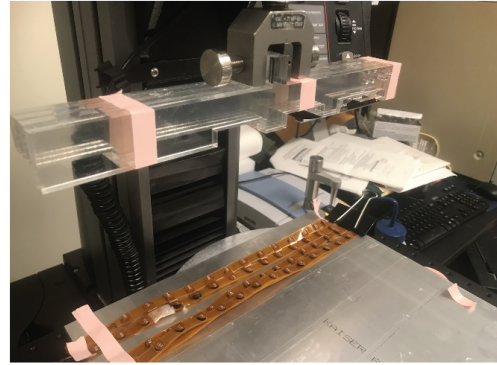


k) MATLAB interface screenshots of voltage when resistor array is connected to row 10-14, column 9-16. l) MATLAB interface screenshots of resistance when resistor array is connected to row 10-14, column 9-16.

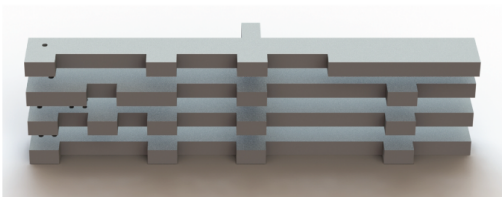
m)



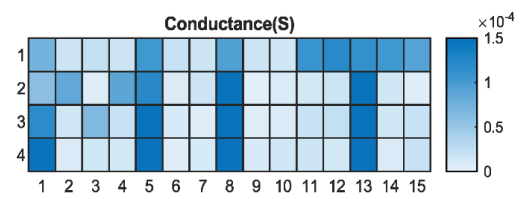
n)



o)



p)



m) Resistance calculation curve. n) A picture of a compression test setup for the “MIT” pattern. o) Laser cut “MIT” patterns to test the cross-talk in the scanning board. p) The result of the “MIT” patterns cross-talk test.

References

- [1] V. D. Graaff and K. M., "Anatomy and physiology of the gastrointestinal tract," *The Pediatric Infectious Disease Journal*, vol. 5, no. 1, pp. 11–16, Feb. 1986.
- [2] R. K. Goyal and A. Chaudhury, "Physiology of Normal Esophageal Motility," *J Clin Gastroenterol*, vol. 42, no. 5, pp. 610–619, 2008, doi: 10.1097/MCG.0b013e31816b444d.
- [3] "How common are abnormal contractions in the healthy subject ?" http://www.oeso.org/OESO/books/Vol_4_Prim_Motility/Articles/ART006.HTML (accessed Jul. 15, 2022).
- [4] S. Brandstaeter, S. L. Fuchs, R. C. Aydin, and C. J. Cyron, "Mechanics of the stomach: A review of an emerging field of biomechanics," *GAMM-Mitteilungen*, vol. 42, no. 3, Sep. 2019, doi: 10.1002/gamm.201900001.
- [5] "First Principles of Gastroenterology." <https://www.cag-acg.org/membership/publications/first-principles-of-gastroenterology> (accessed Aug. 15, 2022).
- [6] J. T. Collins, A. Nguyen, and M. Badireddy, "Anatomy, Abdomen and Pelvis, Small Intestine," in *StatPearls*, Treasure Island (FL): StatPearls Publishing, 2022. Accessed: Aug. 15, 2022. [Online]. Available: <http://www.ncbi.nlm.nih.gov/books/NBK459366/>
- [7] L. L. Azzouz and S. Sharma, "Physiology, Large Intestine," in *StatPearls*, Treasure Island (FL): StatPearls Publishing, 2022. Accessed: Jul. 14, 2022. [Online]. Available: <http://www.ncbi.nlm.nih.gov/books/NBK507857/>
- [8] L. Kloetzer *et al.*, "Motility of the antroduodenum in healthy and gastroparetics characterized by wireless motility capsule," *Neurogastroenterology & Motility*, vol. 22, no. 5, pp. 527–e117, 2010, doi: 10.1111/j.1365-2982.2010.01468.x.
- [9] F. Narducci, G. Bassotti, M. Gaburri, and A. Morelli, "Twenty four hour manometric recording of colonic motor activity in healthy man.," *Gut*, vol. 28, no. 1, pp. 17–25, Jan. 1987, doi: 10.1136/gut.28.1.17.
- [10] J. N. Rao and J.-Y. Wang, *Intestinal Architecture and Development*. Morgan & Claypool Life Sciences, 2010. Accessed: Aug. 07, 2022. [Online]. Available: <https://www.ncbi.nlm.nih.gov/books/NBK54098/>
- [11] L. Miller *et al.*, "Physiology of the upper segment, body, and lower segment of the esophagus," *Ann N Y Acad Sci*, vol. 1300, pp. 261–277, Oct. 2013, doi: 10.1111/nyas.12250.
- [12] "General Structure of the Digestive System | SEER Training." <https://training.seer.cancer.gov/anatomy/digestive/structure.html> (accessed Aug. 10, 2022).
- [13] K. N. Browning and R. A. Travagli, "Central Nervous System Control of Gastrointestinal Motility and Secretion and Modulation of Gastrointestinal Functions," *Compr Physiol*, vol. 4, no. 4, pp. 1339–1368, Oct. 2014, doi: 10.1002/cphy.c130055.
- [14] M. Costa, "Anatomy and physiology of the enteric nervous system," *Gut*, vol. 47, no. 90004, pp. 15iv–1519, Dec. 2000, doi: 10.1136/gut.47.suppl_4.iv15.
- [15] J. B. Furness, "Types of neurons in the enteric nervous system," *Journal of the Autonomic Nervous System*, vol. 81, no. 1, pp. 87–96, Jul. 2000, doi: 10.1016/S0165-1838(00)00127-2.

- [16] W. A. A. Kunze and J. B. Furness, "The Enteric Nervous System and Regulation of Intestinal Motility," *Annual Review of Physiology*, vol. 61, no. 1, pp. 117–142, 1999, doi: 10.1146/annurev.physiol.61.1.117.
- [17] J. B. Furness, C. Jones, K. Nurgali, and N. Clerc, "Intrinsic primary afferent neurons and nerve circuits within the intestine," *Progress in Neurobiology*, vol. 72, no. 2, pp. 143–164, Feb. 2004, doi: 10.1016/j.pneurobio.2003.12.004.
- [18] N. J. Spencer and H. Hu, "Enteric nervous system: sensory transduction, neural circuits and gastrointestinal motility," *Nat Rev Gastroenterol Hepatol*, vol. 17, no. 6, pp. 338–351, Jun. 2020, doi: 10.1038/s41575-020-0271-2.
- [19] M. D. Binder, N. Hirokawa, and U. Windhorst, Eds., "Intestinofugal Neurons," in *Encyclopedia of Neuroscience*, Berlin, Heidelberg: Springer, 2009, pp. 2018–2018. doi: 10.1007/978-3-540-29678-2_2549.
- [20] A. Brehmer, F. Schrödl, and W. Neuhuber, "Morphological classifications of enteric neurons -- 100 years after Dogiel," *Anatomy and Embryology*, vol. 200, no. 2, pp. 125–135, Jun. 1999, doi: 10.1007/s004290050267.
- [21] B. G. Nezami and S. Srinivasan, "Enteric Nervous System in the Small Intestine: Pathophysiology and Clinical Implications," *Curr Gastroenterol Rep*, vol. 12, no. 5, pp. 358–365, Oct. 2010, doi: 10.1007/s11894-010-0129-9.
- [22] M. Camilleri *et al.*, "Gastroparesis," *Nat Rev Dis Primers*, vol. 4, no. 1, Art. no. 1, Nov. 2018, doi: 10.1038/s41572-018-0038-z.
- [23] *The Human Central Nervous System*. Accessed: Jan. 05, 2023. [Online]. Available: <https://link.springer.com/book/10.1007/978-3-540-34686-9>
- [24] P. E. Ludwig, V. Reddy, and M. Varacallo, "Neuroanatomy, Central Nervous System (CNS)," in *StatPearls*, Treasure Island (FL): StatPearls Publishing, 2022. Accessed: Jan. 05, 2023. [Online]. Available: <http://www.ncbi.nlm.nih.gov/books/NBK442010/>
- [25] S. M. Altschuler, J. Escardo, R. B. Lynn, and R. R. Miselis, "The central organization of the vagus nerve innervating the colon of the rat," *Gastroenterology*, vol. 104, no. 2, pp. 502–509, Feb. 1993, doi: 10.1016/0016-5085(93)90419-d.
- [26] H.-R. Berthoud, A. Jedrzejewska, and T. L. Powley, "Simultaneous labeling of vagal innervation of the gut and afferent projections from the visceral forebrain with Dil injected into the dorsal vagal complex in the rat," *Journal of Comparative Neurology*, vol. 301, no. 1, pp. 65–79, 1990, doi: 10.1002/cne.903010107.
- [27] K. M. Sanders, S. D. Koh, S. Ro, and S. M. Ward, "Regulation of gastrointestinal motility—insights from smooth muscle biology," *Nat Rev Gastroenterol Hepatol*, vol. 9, no. 11, pp. 633–645, Nov. 2012, doi: 10.1038/nrgastro.2012.168.
- [28] R. A. Travagli, G. E. Hermann, K. N. Browning, and R. C. Rogers, "Brainstem Circuits Regulating Gastric Function," *Annu Rev Physiol*, vol. 68, pp. 279–305, 2006, doi: 10.1146/annurev.physiol.68.040504.094635.
- [29] R. C. Garry, "The nervous control of the caudal region of the large bowel in the cat," *J Physiol*, vol. 77, no. 4, pp. 422–431, Mar. 1933.
- [30] M. H. Vriesman, I. J. N. Koppen, M. Camilleri, C. Di Lorenzo, and M. A. Benninga, "Management of functional constipation in children and adults," *Nat Rev Gastroenterol Hepatol*, vol. 17, no. 1, Art. no. 1, Jan. 2020, doi: 10.1038/s41575-019-0222-y.

- [31] B. Barberio, C. Judge, E. V. Savarino, and A. C. Ford, "Global prevalence of functional constipation according to the Rome criteria: a systematic review and meta-analysis," *Lancet Gastroenterol Hepatol*, vol. 6, no. 8, pp. 638–648, Aug. 2021, doi: 10.1016/S2468-1253(21)00111-4.
- [32] M. I. Pinto Sanchez and P. Bercik, "Epidemiology and burden of chronic constipation," *Can J Gastroenterol*, vol. 25, no. Suppl B, pp. 11B-15B, Oct. 2011.
- [33] C. J. Black, D. A. Drossman, N. J. Talley, J. Ruddy, and A. C. Ford, "Functional gastrointestinal disorders: advances in understanding and management," *The Lancet*, vol. 396, no. 10263, pp. 1664–1674, Nov. 2020, doi: 10.1016/S0140-6736(20)32115-2.
- [34] C. N. Andrews and M. Storr, "The pathophysiology of chronic constipation," *Can J Gastroenterol*, vol. 25, no. Suppl B, pp. 16B-21B, Oct. 2011.
- [35] L. Chang, S. Sultan, A. Lembo, G. N. Verne, W. Smalley, and J. J. Heidelbaugh, "AGA Clinical Practice Guideline on the Pharmacological Management of Irritable Bowel Syndrome With Constipation," *Gastroenterology*, vol. 163, no. 1, pp. 118–136, Jul. 2022, doi: 10.1053/j.gastro.2022.04.016.
- [36] B. E. Lacy, "Diagnosis and treatment of diarrhea-predominant irritable bowel syndrome," *Int J Gen Med*, vol. 9, pp. 7–17, Feb. 2016, doi: 10.2147/IJGM.S93698.
- [37] G. F. Longstreth, W. G. Thompson, W. D. Chey, L. A. Houghton, F. Mearin, and R. C. Spiller, "Functional Bowel Disorders," *Gastroenterology*, vol. 130, no. 5, pp. 1480–1491, Apr. 2006, doi: 10.1053/j.gastro.2005.11.061.
- [38] G. Juckett and R. Trivedi, "Evaluation of Chronic Diarrhea," *afp*, vol. 84, no. 10, pp. 1119–1126, Nov. 2011.
- [39] J. L. Buono, K. Mathur, A. J. Averitt, and D. A. Andrae, "Economic Burden of Irritable Bowel Syndrome with Diarrhea: Retrospective Analysis of a U.S. Commercially Insured Population," *JMCP*, vol. 23, no. 4, pp. 453–460, Apr. 2017, doi: 10.18553/jmcp.2016.16138.
- [40] G. Bazzocchi, J. Ellis, J. Villanueva-Meyer, S. N. Reddy, I. Mena, and W. J. Snape, "Effect of eating on colonic motility and transit in patients with functional diarrhea: Simultaneous scintigraphic and manometric evaluations," *Gastroenterology*, vol. 101, no. 5, pp. 1298–1306, Nov. 1991, doi: 10.1016/0016-5085(91)90080-5.
- [41] A. Lembo, S. Sultan, L. Chang, J. J. Heidelbaugh, W. Smalley, and G. N. Verne, "AGA Clinical Practice Guideline on the Pharmacological Management of Irritable Bowel Syndrome With Diarrhea," *Gastroenterology*, vol. 163, no. 1, pp. 137–151, Jul. 2022, doi: 10.1053/j.gastro.2022.04.017.
- [42] D. A. Patel *et al.*, "Economic and survival burden of dysphagia among inpatients in the United States," *Dis Esophagus*, vol. 31, no. 1, p. dox131, Nov. 2017, doi: 10.1093/dote/dox131.
- [43] P. Chilukuri, F. Odufalu, and C. Hachem, "Dysphagia," *Mo Med*, vol. 115, no. 3, pp. 206–210, 2018.
- [44] M. R. Spieker, "Evaluating Dysphagia," *afp*, vol. 61, no. 12, pp. 3639–3648, Jun. 2000.
- [45] A. E. Bharucha, "EPIDEMIOLOGY AND NATURAL HISTORY OF GASTROPARESIS," *Gastroenterol Clin North Am*, vol. 44, no. 1, pp. 9–19, Mar. 2015, doi: 10.1016/j.gtc.2014.11.002.
- [46] E. Rey, R. S. Choung, C. D. Schleck, A. R. Zinsmeister, N. J. Talley, and G. R. Locke, "Prevalence of Hidden Gastroparesis in the Community: The Gastroparesis 'Iceberg,'" *J*

- Neurogastroenterol Motil*, vol. 18, no. 1, pp. 34–42, Jan. 2012, doi: 10.5056/jnm.2012.18.1.34.
- [47] N. Liu and T. Abell, “Gastroparesis Updates on Pathogenesis and Management,” *Gut Liver*, vol. 11, no. 5, pp. 579–589, Sep. 2017, doi: 10.5009/gnl16336.
- [48] “Symptoms & Causes of Gastroparesis | NIDDK,” *National Institute of Diabetes and Digestive and Kidney Diseases*. <https://www.niddk.nih.gov/health-information/digestive-diseases/gastroparesis/symptoms-causes> (accessed Jul. 28, 2022).
- [49] Y. J. Chen *et al.*, “Health-care resource use and costs associated with diabetic and idiopathic gastroparesis: A claims analysis of the first 3 years following the diagnosis of gastroparesis,” *Neurogastroenterology & Motility*, vol. n/a, no. n/a, p. e14366, doi: 10.1111/nmo.14366.
- [50] C. Cock and T. Omari, “Systematic Review of Pharyngeal and Esophageal Manometry in Healthy or Dysphagic Older Persons (>60 years),” *Geriatrics*, vol. 3, no. 4, p. 67, Oct. 2018, doi: 10.3390/geriatrics3040067.
- [51] M. Goyal and S. Nagalli, “Esophageal Motility Disorders,” in *StatPearls*, Treasure Island (FL): StatPearls Publishing, 2022. Accessed: Jul. 20, 2022. [Online]. Available: <http://www.ncbi.nlm.nih.gov/books/NBK562155/>
- [52] J. A. Murray, R. E. Clouse, and J. L. Conklin, “Components of the standard oesophageal manometry,” *Neurogastroenterol Motil*, vol. 15, no. 6, pp. 591–606, Dec. 2003, doi: 10.1046/j.1365-2982.2003.00446.x.
- [53] “What to Expect During an Esophageal Manometry Test,” *Verywell Health*. <https://www.verywellhealth.com/esophageal-manometry-test-4157830> (accessed Jun. 16, 2022).
- [54] D. A. Carlson and P. J. Kahrilas, “How to Effectively Use High-Resolution Esophageal Manometry,” *Gastroenterology*, vol. 151, no. 5, pp. 789–792, Nov. 2016, doi: 10.1053/j.gastro.2016.09.024.
- [55] “ManoScan™ ESO High Resolution Manometry System | Medtronic.” <https://www.medtronic.com/covidien/en-us/products/motility-testing/manoscan-eso-high-resolution-manometry-system.html> (accessed Jul. 29, 2022).
- [56] “High Resolution Manometry System,” *SMIT Medical*. <https://www.smitmedical.com/project/manoscan-high-resolution-manometry-system-diagnostic-definition/> (accessed Jul. 29, 2022).
- [57] “Solar GI HRM,” *Laborie*. <https://www.laborie.com/product/solar-gi-hrm/> (accessed Jul. 29, 2022).
- [58] “Solid State Catheters,” *GI+Supply*. <https://www.gi-supply.com/products/gi-motility/solid-state-catheters/> (accessed Feb. 13, 2023).
- [59] “THD® Anopress: portable Clinical Anorectal Manometry - THDLAB - CO UK | THD.” <https://www.thdlab.co.uk/healthcare-professionals/products/thd-anopress> (accessed Feb. 13, 2023).
- [60] “Landing page,” *Lasermed AG*. <https://www.lasermed.ch/pages/landing-page> (accessed Feb. 13, 2023).
- [61] A. D. Farmer, S. M. Scott, and A. R. Hobson, “Gastrointestinal motility revisited: The wireless motility capsule,” *United European Gastroenterol J*, vol. 1, no. 6, pp. 413–421, Dec. 2013, doi: 10.1177/2050640613510161.

- [62] GIS, “Capsule Endoscopy,” *Gastrointestinal Society*. <https://badgut.org/information-centre/a-z-digestive-topics/capsule-endoscopy/> (accessed Feb. 13, 2023).
- [63] D. U. M.D, “MR Enterography | Maryland Radiologist | Charter Radiology.” <https://www.charterradiology.com/mr-enterography/> (accessed Feb. 13, 2023).
- [64] “CT Enterography - Los Angeles, CA,” *Cedars-Sinai*. <https://www.cedars-sinai.org/programs/imaging-center/exams/ct-scans/enterography.html> (accessed Feb. 13, 2023).
- [65] A. H. Maurer, “Gastric Emptying Scintigraphy,” in *Gastroparesis: Pathophysiology, Presentation and Treatment*, H. P. Parkman and R. W. McCallum, Eds., in *Clinical Gastroenterology*. Totowa, NJ: Humana Press, 2012, pp. 97–111. doi: 10.1007/978-1-60761-552-1_9.
- [66] “Anorectal Manometry,” *Cleveland Clinic*. <https://my.clevelandclinic.org/health/diagnostics/12760-anorectal-manometry> (accessed Jun. 24, 2022).
- [67] T. H. Lee and A. E. Bharucha, “How to Perform and Interpret a High-resolution Anorectal Manometry Test,” *J Neurogastroenterol Motil*, vol. 22, no. 1, pp. 46–59, Jan. 2016, doi: 10.5056/jnm15168.
- [68] K. Tran, R. Brun, and B. Kuo, “Evaluation of regional and whole gut motility using the wireless motility capsule: relevance in clinical practice,” *Therap Adv Gastroenterol*, vol. 5, no. 4, pp. 249–260, Jul. 2012, doi: 10.1177/1756283X12437874.
- [69] “A Technical Review and Clinical Assessment of the Wireless Motility Capsule – Gastroenterology & Hepatology.” <https://www.gastroenterologyandhepatology.net/archives/december-2011/a-technical-review-and-clinical-assessment-of-the-wireless-motility-capsule/> (accessed Jun. 24, 2022).
- [70] “SmartPill™ Motility Testing System | Medtronic.” <https://www.medtronic.com/covidien/en-us/products/motility-testing/smartpill-motility-testing-system.html> (accessed Jun. 22, 2022).
- [71] “SmartPill™ Motility Testing System | Medtronic.” <https://www.medtronic.com/covidien/en-us/products/motility-testing/smartpill-motility-testing-system.html> (accessed Jun. 22, 2022).
- [72] “Radioisotope Vendors | Office of Clinical and Research Safety.” <https://www.vumc.org/safety/rad/radioisotope-vendors> (accessed Aug. 17, 2022).
- [73] “Capsule Endoscopy Market Size Report, 2021-2028.” <https://www.grandviewresearch.com/industry-analysis/capsule-endoscopes-market> (accessed Jun. 24, 2022).
- [74] G. Masselli and G. Gualdi, “CT and MR enterography in evaluating small bowel diseases: when to use which modality?,” *Abdom Imaging*, vol. 38, no. 2, pp. 249–259, Apr. 2013, doi: 10.1007/s00261-012-9961-8.
- [75] H. A. Siddiki *et al.*, “Prospective Comparison of State-of-the-Art MR Enterography and CT Enterography in Small-Bowel Crohn’s Disease,” *American Journal of Roentgenology*, vol. 193, no. 1, pp. 113–121, Jul. 2009, doi: 10.2214/AJR.08.2027.
- [76] R. Ilangovan, D. Burling, A. George, A. Gupta, M. Marshall, and S. A. Taylor, “CT enterography: review of technique and practical tips,” *BJR*, vol. 85, no. 1015, pp. 876–886, Jul. 2012, doi: 10.1259/bjr/27973476.

- [77] “CT Enterography,” Nov. 19, 2019. <https://www.hopkinsmedicine.org/health/treatment-tests-and-therapies/ct-enterography> (accessed Jul. 01, 2022).
- [78] “MR Enterography,” Sep. 14, 2020. <https://www.hopkinsmedicine.org/health/treatment-tests-and-therapies/mr-enterography> (accessed Jul. 01, 2022).
- [79] “Guide to CT Scanner Types, Brands, and Models (2022),” May 19, 2022. <https://lbnmedical.com/guide-to-ct-scanners/> (accessed Jul. 01, 2022).
- [80] “Top MRI Manufacturers Compared: Choosing the Best for Your Needs.” <https://info.blockimaging.com/top-mri-manufacturers-compared-choosing-the-best-for-your-needs> (accessed Jul. 01, 2022).
- [81] T. L. Abell *et al.*, “Consensus Recommendations for Gastric Emptying Scintigraphy: A Joint Report of the American Neurogastroenterology and Motility Society and the Society of Nuclear Medicine,” *Journal of Nuclear Medicine Technology*, vol. 36, no. 1, pp. 44–54, Mar. 2008, doi: 10.2967/jnmt.107.048116.
- [82] K. P. Banks, K. Syed, M. Parekh, and N. McWhorter, “Gastric Emptying Scan,” in *StatPearls*, Treasure Island (FL): StatPearls Publishing, 2022. Accessed: Jun. 24, 2022. [Online]. Available: <http://www.ncbi.nlm.nih.gov/books/NBK531503/>
- [83] L. B. Solnes, S. Sheikhabahaei, and H. A. Ziessman, “Nuclear Scintigraphy in Practice: Gastrointestinal Motility,” *American Journal of Roentgenology*, vol. 211, no. 2, pp. 260–266, Aug. 2018, doi: 10.2214/AJR.18.19787.
- [84] A. H. Maurer, “Gastrointestinal Motility, Part 1: Esophageal Transit and Gastric Emptying,” *Journal of Nuclear Medicine*, vol. 56, no. 8, pp. 1229–1238, Aug. 2015, doi: 10.2967/jnumed.112.114314.
- [85] “Thyroid scintigraphy Gamma camera - All medical device manufacturers.” <https://www.medicalexpo.com/medical-manufacturer/thyroid-scintigraphy-gamma-camera-56423.html> (accessed Aug. 03, 2022).
- [86] G. O’Grady *et al.*, “Abnormal initiation and conduction of slow-wave activity in gastroparesis, defined by high-resolution electrical mapping,” *Gastroenterology*, vol. 143, no. 3, pp. 589-598.e3, Sep. 2012, doi: 10.1053/j.gastro.2012.05.036.
- [87] J. Tomek, P. Mlejnek, V. Janásek, P. Ripka, P. Kašpar, and J. Chen, “The precision of gastric motility and volume sensing by implanted magnetic sensors,” *Sensors and Actuators A: Physical*, vol. 142, no. 1, pp. 34–39, Mar. 2008, doi: 10.1016/j.sna.2007.04.020.
- [88] L. R. Silva, P. J. Sousa, L. M. Goncalves, and G. Minas, “Flexible gastrointestinal motility pressure sensors based on aluminum thin-film strain-gauge arrays,” *J. Micromech. Microeng.*, vol. 25, no. 7, p. 074007, Jun. 2015, doi: 10.1088/0960-1317/25/7/074007.
- [89] “Electrogastrogram,” *Healthgrades*, Jul. 22, 2014. <https://www.healthgrades.com/right-care/digestive-health/electrogastrogram> (accessed Jul. 26, 2022).
- [90] K. Nan *et al.*, “Low-cost gastrointestinal manometry via silicone–liquid-metal pressure transducers resembling a quipu,” *Nat. Biomed. Eng.*, Mar. 2022, doi: 10.1038/s41551-022-00859-5.
- [91] C. Dagdeviren *et al.*, “Flexible piezoelectric devices for gastrointestinal motility sensing,” *Nat Biomed Eng*, vol. 1, no. 10, Art. no. 10, Oct. 2017, doi: 10.1038/s41551-017-0140-7.

- [92] L. K. Cheng, P. Du, and G. O'Grady, "Mapping and Modeling Gastrointestinal Bioelectricity: From Engineering Bench to Bedside," *Physiology*, vol. 28, no. 5, pp. 310–317, Sep. 2013, doi: 10.1152/physiol.00022.2013.
- [93] P. DU *et al.*, "High-resolution Mapping of In Vivo Gastrointestinal Slow Wave Activity Using Flexible Printed Circuit Board Electrodes: Methodology and Validation," *Ann Biomed Eng*, vol. 37, no. 4, pp. 839–846, Apr. 2009, doi: 10.1007/s10439-009-9654-9.
- [94] J. W. Arkwright *et al.*, "In-vivo demonstration of a high resolution optical fiber manometry catheter for diagnosis of gastrointestinal motility disorders," *Opt. Express, OE*, vol. 17, no. 6, pp. 4500–4508, Mar. 2009, doi: 10.1364/OE.17.004500.
- [95] J. W. Arkwright *et al.*, "Design of a high-sensor count fibre optic manometry catheter for in-vivo colonic diagnostics," *Opt. Express, OE*, vol. 17, no. 25, pp. 22423–22431, Dec. 2009, doi: 10.1364/OE.17.022423.
- [96] A Ruiz-Vargas, M. Costa, Lukasz Wiklendt, P. G. Dinning, and J. W. Arkwright, "The Use of Fibre Optic Sensing Technology with Intraluminal Impedance Catheter for Functional Gastrointestinal Motility Disorders," 2015, doi: 10.13140/RG.2.1.3125.9124.
- [97] E. J. Beckers, N. J. Rehrer, F. Brouns, F. Ten Hoor, and W. H. Saris, "Determination of total gastric volume, gastric secretion and residual meal using the double sampling technique of George.," *Gut*, vol. 29, no. 12, pp. 1725–1729, Dec. 1988, doi: 10.1136/gut.29.12.1725.
- [98] C. Dimoulas, G. Kalliris, G. Papanikolaou, V. Petridis, and A. Kalampakas, "Bowel-sound pattern analysis using wavelets and neural networks with application to long-term, unsupervised, gastrointestinal motility monitoring," *Expert Systems with Applications*, vol. 34, no. 1, pp. 26–41, Jan. 2008, doi: 10.1016/j.eswa.2006.08.014.
- [99] F. C. Paixão, L. A. Corá, M. F. Américo, R. B. de Oliveira, O. Baffa, and J. R. A. Miranda, "Development of an AMR-ACB Array for Gastrointestinal Motility Studies," *IEEE Trans. Biomed. Eng.*, vol. 59, no. 10, pp. 2737–2743, Oct. 2012, doi: 10.1109/TBME.2012.2208748.
- [100] G. O'Grady, "Gastrointestinal extracellular electrical recordings: fact or artifact?," *Neurogastroenterol Motil*, vol. 24, no. 1, pp. 1–6, Jan. 2012, doi: 10.1111/j.1365-2982.2011.01815.x.
- [101] J. K. Stevens and N. Worrall, "External recording of gastric activity: The electrogastragram," *Psychobiology*, vol. 2, no. 2, pp. 175–180, Jun. 1974, doi: 10.3758/BF03333020.
- [102] F. W. Woodley *et al.*, "Gastroesophageal reflux in cystic fibrosis across the age spectrum," *Transl. Gastroenterol. Hepatol*, vol. 4, pp. 69–69, Sep. 2019, doi: 10.21037/tgh.2019.08.11.
- [103] C. Shi *et al.*, "Application of a sub-0.1-mm³ implantable mote for in vivo real-time wireless temperature sensing," *Sci Adv*, vol. 7, no. 19, p. eabf6312, May 2021, doi: 10.1126/sciadv.abf6312.
- [104] "Satiety - an overview | ScienceDirect Topics." <https://www.sciencedirect.com/topics/agricultural-and-biological-sciences/satiety> (accessed Aug. 11, 2022).
- [105] G. J. Schwartz, "The role of gastrointestinal vagal afferents in the control of food intake: current prospects," *Nutrition*, vol. 16, no. 10, pp. 866–873, Oct. 2000, doi: 10.1016/S0899-9007(00)00464-0.

- [106] R. S. Ahima and D. A. Antwi, "Brain regulation of appetite and satiety," *Endocrinol Metab Clin North Am*, vol. 37, no. 4, pp. 811–823, Dec. 2008, doi: 10.1016/j.ecl.2008.08.005.
- [107] S. Breit, A. Kupferberg, G. Rogler, and G. Hasler, "Vagus Nerve as Modulator of the Brain–Gut Axis in Psychiatric and Inflammatory Disorders," *Frontiers in Psychiatry*, vol. 9, 2018, Accessed: Jun. 24, 2022. [Online]. Available: <https://www.frontiersin.org/article/10.3389/fpsy.2018.00044>
- [108] S. Luquet, F. A. Perez, T. S. Hnasko, and R. D. Palmiter, "NPY/AgRP Neurons Are Essential for Feeding in Adult Mice but Can Be Ablated in Neonates," *Science*, vol. 310, no. 5748, pp. 683–685, Oct. 2005, doi: 10.1126/science.1115524.
- [109] "Appetite regulation and weight control: the role of gut hormones | Nutrition & Diabetes." <https://www.nature.com/articles/nutd201121> (accessed Aug. 25, 2022).
- [110] O. B. Chaudhri, V. Salem, K. G. Murphy, and S. R. Bloom, "Gastrointestinal satiety signals," *Annu Rev Physiol*, vol. 70, pp. 239–255, 2008, doi: 10.1146/annurev.physiol.70.113006.100506.
- [111] K. Timper and J. C. Brüning, "Hypothalamic circuits regulating appetite and energy homeostasis: pathways to obesity," *Disease Models & Mechanisms*, vol. 10, no. 6, pp. 679–689, Jun. 2017, doi: 10.1242/dmm.026609.
- [112] M. W. Schwartz *et al.*, "Obesity Pathogenesis: An Endocrine Society Scientific Statement," *Endocrine Reviews*, vol. 38, no. 4, pp. 267–296, Aug. 2017, doi: 10.1210/er.2017-00111.
- [113] M. D. Turton *et al.*, "A role for glucagon-like peptide-1 in the central regulation of feeding," *Nature*, vol. 379, no. 6560, pp. 69–72, Jan. 1996, doi: 10.1038/379069a0.
- [114] "Distribution and release of human pancreatic polypeptide. | Gut." <https://gut.bmj.com/content/17/12/940.long> (accessed Aug. 28, 2022).
- [115] Y. Wang, X. Guo, X. Lu, S. Mattar, and G. Kassab, "Mechanisms of Weight Loss After Sleeve Gastrectomy and Adjustable Gastric Banding: Far More Than Just Restriction," *Obesity*, vol. 27, no. 11, pp. 1776–1783, 2019, doi: 10.1002/oby.22623.
- [116] L. Fischer *et al.*, "Excessive Weight Loss after Sleeve Gastrectomy: A Systematic Review," *OBES SURG*, vol. 22, no. 5, pp. 721–731, May 2012, doi: 10.1007/s11695-012-0616-1.
- [117] R. S. Gill, D. W. Birch, X. Shi, A. M. Sharma, and S. Karmali, "Sleeve gastrectomy and type 2 diabetes mellitus: a systematic review," *Surgery for Obesity and Related Diseases*, vol. 6, no. 6, pp. 707–713, Nov. 2010, doi: 10.1016/j.soard.2010.07.011.
- [118] D. Singh, A. S. Laya, W. K. Clarkston, and M. J. Allen, "Jejunioileal bypass: A surgery of the past and a review of its complications," *World J Gastroenterol*, vol. 15, no. 18, pp. 2277–2279, May 2009, doi: 10.3748/wjg.15.2277.
- [119] D. E. Cummings, J. Overduin, K. E. Foster-Schubert, and M. J. Carlson, "Role of the bypassed proximal intestine in the anti-diabetic effects of bariatric surgery," *Surgery for Obesity and Related Diseases*, vol. 3, no. 2, pp. 109–115, Mar. 2007, doi: 10.1016/j.soard.2007.02.003.
- [120] "Vertical Banded Gastroplasty." <https://www.ypo.education/bariatrics/vertical-banded-gastroplasty-t203/video/> (accessed Mar. 01, 2023).
- [121] M. R. van Wezenbeek, J. F. Smulders, J. P. J. G. M. de Zoete, M. D. Luyer, G. van Montfort, and S. W. Nienhuijs, "Long-Term Results of Primary Vertical Banded

- Gastroplasty," *OBES SURG*, vol. 25, no. 8, pp. 1425–1430, Aug. 2015, doi: 10.1007/s11695-014-1543-0.
- [122] "Laparoscopic Adjustable Gastric Banding," Aug. 08, 2021.
<https://www.hopkinsmedicine.org/health/treatment-tests-and-therapies/laparoscopic-adjustable-gastric-banding> (accessed Mar. 01, 2023).
- [123] J. H. Ahroni, K. F. Montgomery, and B. M. Watkins, "Laparoscopic Adjustable Gastric Banding: Weight Loss, Co-morbidities, Medication Usage and Quality of Life at One Year," *OBES SURG*, vol. 15, no. 5, pp. 641–647, May 2005, doi: 10.1381/0960892053923716.
- [124] "Roux-en-Y Gastric Bypass Weight-Loss Surgery," Aug. 08, 2021.
<https://www.hopkinsmedicine.org/health/treatment-tests-and-therapies/rouxeny-gastric-bypass-weightloss-surgery> (accessed Mar. 01, 2023).
- [125] P. R. Schauer *et al.*, "Bariatric Surgery versus Intensive Medical Therapy in Obese Patients with Diabetes," *N Engl J Med*, vol. 366, no. 17, pp. 1567–1576, Apr. 2012, doi: 10.1056/NEJMoa1200225.
- [126] J. Glass, A. Chaudhry, M. S. Zeeshan, and Z. Ramzan, "New Era: Endoscopic treatment options in obesity—a paradigm shift," *World Journal of Gastroenterology*, vol. 25, no. 32, pp. 4567–4579, Aug. 2019, doi: 10.3748/wjg.v25.i32.4567.
- [127] D. Štimac, S. Klobučar Majanović, and A. Belančić, "Endoscopic Treatment of Obesity: From Past to Future," *DDI*, vol. 38, no. 2, pp. 150–162, 2020, doi: 10.1159/000505394.
- [128] F. Bazerbachi *et al.*, "Intragastric Balloon Placement Induces Significant Metabolic and Histologic Improvement in Patients With Nonalcoholic Steatohepatitis," *Clinical Gastroenterology and Hepatology*, vol. 19, no. 1, pp. 146-154.e4, Jan. 2021, doi: 10.1016/j.cgh.2020.04.068.
- [129] R. Z. Sharaiha *et al.*, "Endoscopic Sleeve Gastroplasty Significantly Reduces Body Mass Index and Metabolic Complications in Obese Patients," *Clinical Gastroenterology and Hepatology*, vol. 15, no. 4, pp. 504–510, Apr. 2017, doi: 10.1016/j.cgh.2016.12.012.
- [130] G. Lopez-Nava, M. P. Galvão, I. Bautista-Castaño, A. Jimenez-Baños, and J. P. Fernandez-Corbelle, "Endoscopic Sleeve Gastroplasty: How I Do It?," *OBES SURG*, vol. 25, no. 8, pp. 1534–1538, Aug. 2015, doi: 10.1007/s11695-015-1714-7.
- [131] J. M. Kolb and H. Hammad, "The Use of the Overstitch to Close Endoscopic Resection Defects," *Gastrointestinal Endoscopy Clinics*, vol. 30, no. 1, pp. 163–171, Jan. 2020, doi: 10.1016/j.giec.2019.08.006.
- [132] "Aspire Bariatrics Company Update," *Aspire Bariatrics Company Update*.
<https://www.aspirebariatrics.com> (accessed Mar. 01, 2023).
- [133] M. Nyström *et al.*, "Aspiration Therapy As a Tool to Treat Obesity: 1- to 4-Year Results in a 201-Patient Multi-Center Post-Market European Registry Study," *OBES SURG*, vol. 28, no. 7, pp. 1860–1868, Jul. 2018, doi: 10.1007/s11695-017-3096-5.
- [134] "Drug Approval Package: Xenical (Orlistat) NDA# 20-766."
https://www.accessdata.fda.gov/drugsatfda_docs/nda/99/020766a.cfm (accessed Sep. 01, 2022).
- [135] "Drug Approval Package: Qsymia (phentermine and topiramate extended-release) NDA #22580Orig1s000."
https://www.accessdata.fda.gov/drugsatfda_docs/nda/2012/022580orig1s000_qsymia_toc.cfm (accessed Sep. 02, 2022).

- [136] “Drug Approval Package: Brand Name (Generic Name) NDA #.”
https://www.accessdata.fda.gov/drugsatfda_docs/nda/2014/200063Orig1s000TOC.cfm
 (accessed Aug. 22, 2022).
- [137] M. M. Sherman, S. Ungureanu, and J. A. Rey, “Naltrexone/Bupropion ER (Contrave),” *P T*, vol. 41, no. 3, pp. 164–172, Mar. 2016.
- [138] “How Saxenda® Works | Saxenda® (liraglutide) injection 3mg.”
<https://www.saxenda.com/about-saxenda/how-it-works.html> (accessed Mar. 01, 2023).
- [139] M. J. Franz, “Weight Management: Obesity to Diabetes,” *Diabetes Spectrum*, vol. 30, no. 3, pp. 149–153, Aug. 2017, doi: 10.2337/ds17-0011.
- [140] “Weight-Loss Prescription Medication | Wegovy® (semaglutide) Injection 2.4 mg.”
<https://www.wegovy.com/> (accessed Mar. 01, 2023).
- [141] O. of the Commissioner, “FDA Approves New Drug Treatment for Chronic Weight Management, First Since 2014,” *FDA*, Jun. 21, 2021. <https://www.fda.gov/news-events/press-announcements/fda-approves-new-drug-treatment-chronic-weight-management-first-2014> (accessed Mar. 01, 2023).
- [142] “IMCIVREE® (setmelanotide) injection,” *IMCIVREE® (setmelanotide) injection*.
<https://www.imcivree.com/> (accessed Mar. 01, 2023).
- [143] D. H. Ryan, “Next Generation Antiobesity Medications: Setmelanotide, Semaglutide, Tirzepatide and Bimagrumb: What do They Mean for Clinical Practice?,” *J Obes Metab Syndr*, vol. 30, no. 3, pp. 196–208, Sep. 2021, doi: 10.7570/jomes21033.
- [144] M. J. Ferrua and R. P. Singh, “Understanding the fluid dynamics of gastric digestion using computational modeling,” *Procedia Food Science*, vol. 1, pp. 1465–1472, 2011, doi: 10.1016/j.profoo.2011.09.217.
- [145] S. Brandstaeter, S. L. Fuchs, R. C. Aydin, and C. J. Cyron, “Mechanics of the stomach: A review of an emerging field of biomechanics,” *GAMM-Mitteilungen*, vol. 42, no. 3, Sep. 2019, doi: 10.1002/gamm.201900001.
- [146] M. Boland, “Human digestion – a processing perspective,” *Journal of the Science of Food and Agriculture*, vol. 96, no. 7, pp. 2275–2283, 2016, doi: 10.1002/jsfa.7601.
- [147] J. Tack, I. Demedts, A. Meulemans, J. Schuurkes, and J. Janssens, “Role of nitric oxide in the gastric accommodation reflex and in meal induced satiety in humans,” *Gut*, vol. 51, no. 2, pp. 219–224, Aug. 2002, doi: 10.1136/gut.51.2.219.
- [148] S. Banerjee, A. Pal, and M. Fox, “Volume and position change of the stomach during gastric accommodation and emptying: A detailed three-dimensional morphological analysis based on MRI,” *Neurogastroenterology & Motility*, vol. 32, no. 8, p. e13865, 2020, doi: 10.1111/nmo.13865.
- [149] L. A. Houghton *et al.*, “Motor activity of the gastric antrum, pylorus, and duodenum under fasted conditions and after a liquid meal,” *Gastroenterology*, vol. 94, no. 6, pp. 1276–1284, Jun. 1988, doi: 10.1016/0016-5085(88)90664-6.
- [150] E. Deloose, P. Janssen, I. Depoortere, and J. Tack, “The migrating motor complex: control mechanisms and its role in health and disease,” *Nat Rev Gastroenterol Hepatol*, vol. 9, no. 5, pp. 271–285, Mar. 2012, doi: 10.1038/nrgastro.2012.57.
- [151] L. Marciiani *et al.*, “Assessment of antral grinding of a model solid meal with echo-planar imaging,” *American Journal of Physiology-Gastrointestinal and Liver Physiology*, vol. 280, no. 5, pp. G844–G849, May 2001, doi: 10.1152/ajpgi.2001.280.5.G844.

- [152] C. Antunes, A. Aleem, and S. A. Curtis, "Gastroesophageal Reflux Disease," in *StatPearls*, Treasure Island (FL): StatPearls Publishing, 2021. Accessed: Dec. 08, 2021. [Online]. Available: <http://www.ncbi.nlm.nih.gov/books/NBK441938/>
- [153] A. E. Bharucha and B. E. Lacy, "Mechanisms, Evaluation, and Management of Chronic Constipation," *Gastroenterology*, vol. 158, no. 5, pp. 1232-1249.e3, Apr. 2020, doi: 10.1053/j.gastro.2019.12.034.
- [154] J. E. Pandolfino and P. J. Kahrilas, "American Gastroenterological Association medical position statement: Clinical use of esophageal manometry," *Gastroenterology*, vol. 128, no. 1, pp. 207–208, Jan. 2005, doi: 10.1053/j.gastro.2004.11.007.
- [155] K. H. Kim, C. S. Yu, Y. S. Yoon, S. N. Yoon, S.-B. Lim, and J. C. Kim, "Effectiveness of Biofeedback Therapy in the Treatment of Anterior Resection Syndrome After Rectal Cancer Surgery," *Diseases of the Colon & Rectum*, vol. 54, no. 9, pp. 1107–1113, Sep. 2011, doi: 10.1097/DCR.0b013e318221a934.
- [156] S. Wiwanitkit and V. Wiwanitkit, "Anorectal manometry and Hirschsprung's disease," *African Journal of Paediatric Surgery*, vol. 10, no. 3, pp. 293–293, Jul. 2013.
- [157] J. Lenglinger, "Impedance Planimetry," in *Dysphagia: Diagnosis and Treatment*, O. Ekberg, Ed., in Medical Radiology. Berlin, Heidelberg: Springer, 2012, pp. 329–337. doi: 10.1007/174_2012_640.
- [158] A. H. Maurer and H. P. Parkman, "Update on Gastrointestinal Scintigraphy," *Seminars in Nuclear Medicine*, vol. 36, no. 2, pp. 110–118, Apr. 2006, doi: 10.1053/j.semnuclmed.2005.12.003.
- [159] D. Carter and E. Bardan, "The Wireless Motility Capsule," in *Gastrointestinal Motility Disorders : A Point of Care Clinical Guide*, E. Bardan and R. Shaker, Eds., Cham: Springer International Publishing, 2018, pp. 373–378. doi: 10.1007/978-3-319-59352-4_34.
- [160] K. Tran, R. Brun, and B. Kuo, "Evaluation of regional and whole gut motility using the wireless motility capsule: relevance in clinical practice," *Therap Adv Gastroenterol*, vol. 5, no. 4, pp. 249–260, Jul. 2012, doi: 10.1177/1756283X12437874.
- [161] P. Enck *et al.*, "Functional dyspepsia," *Nat Rev Dis Primers*, vol. 3, p. 17081, Nov. 2017, doi: 10.1038/nrdp.2017.81.
- [162] P. Du *et al.*, "High-resolution Mapping of In Vivo Gastrointestinal Slow Wave Activity Using Flexible Printed Circuit Board Electrodes: Methodology and Validation," *Ann Biomed Eng*, vol. 37, no. 4, pp. 839–846, Apr. 2009, doi: 10.1007/s10439-009-9654-9.
- [163] T. R. Angeli *et al.*, "Experimental and Automated Analysis Techniques for High-resolution Electrical Mapping of Small Intestine Slow Wave Activity," *J Neurogastroenterol Motil*, vol. 19, no. 2, pp. 179–191, Apr. 2013, doi: 10.5056/jnm.2013.19.2.179.
- [164] L. K. Cheng, P. Du, and G. O'Grady, "Mapping and Modeling Gastrointestinal Bioelectricity: From Engineering Bench to Bedside," *Physiology*, vol. 28, no. 5, pp. 310–317, Sep. 2013, doi: 10.1152/physiol.00022.2013.
- [165] W. J. E. P. Lammers, L. V. Donck, J. A. J. Schuurkes, and B. Stephen, "Peripheral pacemakers and patterns of slow wave propagation in the canine small intestine in vivo," *Can. J. Physiol. Pharmacol.*, vol. 83, no. 11, pp. 1031–1043, Nov. 2005, doi: 10.1139/y05-084.
- [166] G. O'Grady *et al.*, "Rapid high-amplitude circumferential slow wave propagation during normal gastric pacemaking and dysrhythmias: Circumferential gastric slow wave

- propagation,” *Neurogastroenterology & Motility*, vol. 24, no. 7, pp. e299–e312, Jul. 2012, doi: 10.1111/j.1365-2982.2012.01932.x.
- [167] F. W. Woodley *et al.*, “Gastroesophageal reflux in cystic fibrosis across the age spectrum,” *Transl Gastroenterol Hepatol*, vol. 4, p. 69, Sep. 2019, doi: 10.21037/tgh.2019.08.11.
- [168] I. Tachecí *et al.*, “Electrogastrography in experimental pigs: the influence of gastrointestinal injury induced by dextran sodium sulphate on porcine gastric erythromycin-stimulated myoelectric activity,” p. 6, 2011.
- [169] J. W. Arkwright *et al.*, “In-vivo demonstration of a high resolution optical fiber manometry catheter for diagnosis of gastrointestinal motility disorders,” *Opt. Express, OE*, vol. 17, no. 6, pp. 4500–4508, Mar. 2009, doi: 10.1364/OE.17.004500.
- [170] A Ruiz-Vargas, M. Costa, Lukasz Wiklendt, P. G. Dinning, and J. W. Arkwright, “The Use of Fibre Optic Sensing Technology with Intraluminal Impedance Catheter for Functional Gastrointestinal Motility Disorders,” 2015, doi: 10.13140/RG.2.1.3125.9124.
- [171] J. W. Arkwright *et al.*, “The use of wavelength division multiplexed fiber Bragg grating sensors for distributed sensing of pressure in the gastrointestinal tract,” in *2008 IEEE PhotonicsGlobal@Singapore*, Dec. 2008, pp. 1–4. doi: 10.1109/IPGC.2008.4781397.
- [172] J. Tomek, P. Mlejnek, V. Janásek, P. Ripka, P. Kašpar, and J. Chen, “Gastric Motility and Volume Sensing by Implanted Magnetic Sensors,” *Sensor Letters*, vol. 5, no. 1, pp. 276–278, Mar. 2007, doi: 10.1166/sl.2007.002.
- [173] C. Dimoulas, G. Kalliris, G. Papanikolaou, V. Petridis, and A. Kalampakas, “Bowel-sound pattern analysis using wavelets and neural networks with application to long-term, unsupervised, gastrointestinal motility monitoring,” *Expert Systems with Applications*, vol. 34, no. 1, pp. 26–41, Jan. 2008, doi: 10.1016/j.eswa.2006.08.014.
- [174] L. R. Silva, P. J. Sousa, L. M. Goncalves, and G. Minas, “Flexible gastrointestinal motility pressure sensors based on aluminum thin-film strain-gauge arrays,” *J. Micromech. Microeng.*, vol. 25, no. 7, p. 074007, Jun. 2015, doi: 10.1088/0960-1317/25/7/074007.
- [175] F. C. Paixão, L. A. Corá, M. F. Américo, R. B. de Oliveira, O. Baffa, and J. R. A. Miranda, “Development of an AMR-ACB Array for Gastrointestinal Motility Studies,” *IEEE Transactions on Biomedical Engineering*, vol. 59, no. 10, pp. 2737–2743, Oct. 2012, doi: 10.1109/TBME.2012.2208748.
- [176] C. Dagdeviren *et al.*, “Flexible piezoelectric devices for gastrointestinal motility sensing,” *Nature Biomedical Engineering*, vol. 1, no. 10, Art. no. 10, Oct. 2017, doi: 10.1038/s41551-017-0140-7.
- [177] “ManoScan™ ESO High Resolution Manometry System | Medtronic.” <https://www.medtronic.com/covidien/en-us/products/motility-testing/manoscan-eso-high-resolution-manometry-system.html> (accessed Feb. 16, 2022).
- [178] T. R. Kuphaldt and J. Haughery, “ELECTRICAL SAFETY,” Jun. 2020, Accessed: Nov. 01, 2022. [Online]. Available: <https://iastate.pressbooks.pub/electriccircuits/chapter/chapter-1/>
- [179] “Flat Springs: Calculation Formulas,” *Tokai Spring industries, Inc.* <https://www.tokaibane.com/en/spring-design/flat-springs-formulas> (accessed Dec. 13, 2021).

- [180] “Polyamide 6.6 | Designerdata.” <https://designerdata.nl/materials/plastics/thermo-plastics/polyamide-6.6> (accessed Feb. 18, 2022).
- [181] “Poisson’s Ratio of Polymers.” https://amesweb.info/Materials/Poissons_Ratio_of_Polymers.aspx (accessed Feb. 18, 2022).
- [182] J. L. Puckett, V. Bhalla, J. Liu, G. Kassab, and R. K. Mittal, “Oesophageal wall stress and muscle hypertrophy in high amplitude oesophageal contractions,” *Neurogastroenterology & Motility*, vol. 17, no. 6, pp. 791–799, 2005, doi: 10.1111/j.1365-2982.2005.00693.x.
- [183] H. P. Swieskowski, “Design of Helical Compression Springs,” ARMY ARMAMENT RESEARCH AND DEVELOPMENT CENTER DOVER NJ FIRE CONTROL AND SMALL CALIBER WEAPON SYSTEMS LAB, Aug. 1979. Accessed: Apr. 20, 2021. [Online]. Available: <https://apps.dtic.mil/sti/citations/ADA077113>
- [184] S. of A. Engineers, *Spring design manual*. Warrendale, PA: Society of Automotive Engineers, 1990.
- [185] “Swine Health Recommendations: Exhibitors of All Pigs Going to Exhibits or Sales,” *MSU Extension*. https://www.canr.msu.edu/resources/swine_health_recommendations_exhibitors_of_all_pigs_going_to_exhibits_or_sa (accessed Oct. 29, 2022).
- [186] J.-S. Kim, D.-Y. Kwon, and B.-D. Choi, “High-Accuracy, Compact Scanning Method and Circuit for Resistive Sensor Arrays,” *Sensors*, vol. 16, no. 2, Art. no. 2, Feb. 2016, doi: 10.3390/s16020155.
- [187] G. Cheeney, M. Nguyen, J. Valestin, and S. S. C. Rao, “Topographic and manometric characterization of the recto-anal inhibitory reflex,” *Neurogastroenterology & Motility*, vol. 24, no. 3, pp. e147–e154, 2012, doi: 10.1111/j.1365-2982.2011.01857.x.
- [188] Y. Yang, H. Kuwano, Y. Okudaira, A. M. Kholoussy, and T. Matsumoto, “Use of intragastric balloons for weight reduction: An experimental study,” *The American Journal of Surgery*, vol. 153, no. 3, pp. 265–269, Mar. 1987, doi: 10.1016/0002-9610(87)90599-X.
- [189] M. A. Martinez-Brocca *et al.*, “Intragastric Balloon-Induced Satiety is Not Mediated by Modification in Fasting or Postprandial Plasma Ghrelin Levels in Morbid Obesity,” *OBES SURG*, vol. 17, no. 5, pp. 649–657, May 2007, doi: 10.1007/s11695-007-9109-z.
- [190] O. B. Chaudhri, V. Salem, K. G. Murphy, and S. R. Bloom, “Gastrointestinal Satiety Signals,” *Annual Review of Physiology*, vol. 70, no. 1, pp. 239–255, 2008, doi: 10.1146/annurev.physiol.70.113006.100506.
- [191] “Euler’s Column Formula.” https://www.engineeringtoolbox.com/euler-column-formula-d_1813.html (accessed Jan. 23, 2023).
- [192] “What is 304 Stainless Steel?,” *Masteel*. <https://masteel.co.uk/news/what-304-stainless-steel/> (accessed Jan. 23, 2023).
- [193] “All About 6061 Aluminum (Properties, Strength and Uses).” <https://www.thomasnet.com/articles/metals-metal-products/6061-aluminum/> (accessed Jan. 23, 2023).
- [194] A. G. Piersol, *Harris’ Shock and Vibration Handbook (6th Edition)*. McGraw-Hill Professional Publishing, 2000.

- [195] “Lead Screw Torque and Force Calculator.”
<https://www.daycounter.com/Calculators/Lead-Screw-Force-Torque-Calculator.phtml>
(accessed Jan. 26, 2023).
- [196] “N20 DC motor with metal gearbox (6V/100RPM/1:100).”
<https://nettigo.eu/products/n20-dc-motor-with-metal-gearbox-6v-100rpm-1-100> (accessed
Jan. 26, 2023).
- [197] P. K. Kundu, I. M. Cohen, and D. R. Dowling, *Fluid Mechanics*. Academic Press, 2015.